

INVESTIGATION OF IN-SITU COMBUSTION KINETICS
USING THE ISOCONVERSIONAL PRINCIPLE

A DISSERTATION
SUBMITTED TO THE DEPARTMENT OF ENERGY
RESOURCES ENGINEERING
AND THE COMMITTEE ON GRADUATE STUDIES
OF STANFORD UNIVERSITY
IN PARTIAL FULFILLMENT OF THE REQUIREMENTS
FOR THE DEGREE OF
DOCTOR OF PHILOSOPHY

Bo Chen
November 2012

© 2012 by Bo Chen. All Rights Reserved.

Re-distributed by Stanford University under license with the author.



This work is licensed under a Creative Commons Attribution-Noncommercial 3.0 United States License.

<http://creativecommons.org/licenses/by-nc/3.0/us/>

This dissertation is online at: <http://purl.stanford.edu/mf038wz2108>

I certify that I have read this dissertation and that, in my opinion, it is fully adequate in scope and quality as a dissertation for the degree of Doctor of Philosophy.

Anthony Kavscek, Primary Adviser

I certify that I have read this dissertation and that, in my opinion, it is fully adequate in scope and quality as a dissertation for the degree of Doctor of Philosophy.

Louis Castanier

I certify that I have read this dissertation and that, in my opinion, it is fully adequate in scope and quality as a dissertation for the degree of Doctor of Philosophy.

Margot Gerritsen

Approved for the Stanford University Committee on Graduate Studies.

Patricia J. Gumpert, Vice Provost Graduate Education

This signature page was generated electronically upon submission of this dissertation in electronic format. An original signed hard copy of the signature page is on file in University Archives.

Abstract

In-situ combustion (ISC) is the most energy efficient thermal enhanced oil recovery (EOR) method implemented in crude-oil reservoirs. The worldwide implementation of ISC in commercial field projects reached a maximum of 19 during the period of 1970's to 1990's, but it has declined to 4 active operations nowadays. Many failed projects are due to incorrect operations. Understanding the complicated combustion kinetics during the ISC process is essential and significantly important to optimize field operation.

The combination of the experimental tool, ramped temperature oxidation (RTO), and the measured data interpretation method, isoconversional principle, provides a workflow to unlock the complicated characteristics of ISC kinetics. Conducting reliable or repeatable RTO experiments for isoconversional interpretation is the baseline for the workflow. Simulations coupled with a synthetic reaction model in an in-house virtual kinetic cell (VKC) simulator show that reducing temperature deviation caused by exothermic reactions is critical to carry out consistent RTO experiments. The argument is supported by a series of RTO experiments of the same crude-oil mixture, but different working conditions with respect to the kinetic cell design, the volumetric flow rate of air injection and the size of the sample mixture. Furthermore, the consistent RTO experimental results prove the model-free nature of the isoconversional principle and its applicability in the investigation of ISC kinetics. An attempt to combine the isoconversional principle and the conventional interpretation method is proposed to interpret kinetic parameters including apparent activation energy, pre-exponential factor and reaction orders for both fuel and oxygen partial pressure. Simulations in the VKC were carried out to test the proposed method for

a unit and a non-unit reaction order case. The result showed good matches in the kinetic parameters between the interpretation and the simulations. A three-reaction scheme is proposed for two crude-oil mixtures, Alaska crude-oil and Karamay crude-oil, based on the observation and analysis of the activation energy fingerprints and the effluent data. The stoichiometry and the kinetic parameters for the reaction model are interpreted by the proposed method. The combustion models are verified in the commercial reservoir simulator CMG-STARs regarding the temperature histories, the effluent data from RTO experiments, and the isoconversional fingerprints. Further application of the isoconversional principle to analyze the crude-oil combustion includes investigating the sand and clay surface effect on the reaction paths together with X-ray photoelectron spectroscopy (XPS) to study the coke formation characteristics and their reaction kinetics. Screening the ISC candidates with respect to different crude-oil/sand-matrix pairs is also discussed. Lastly, the development of a microwave heating system is discussed to replace the conventional electric furnace system to carry out RTO experiments. Three generations of the microwave heating system are developed and discussed.

Acknowledgements

As my wife and friends always say I am a lucky person, this is really the truth when I gained the opportunity to be a PhD student in Professor Anthony Kovsky's group. I will never ever forget every moment I entered Professor Kovsky's office with discouraging results from my research, I always received encouraging words and warm smiles from him even if he was busy with his work. I sincerely appreciate all of the knowledge and skills I have learned during my PhD course under Professor Kovsky's supervision. Meanwhile, I feel guilty I should have contributed more to this exciting group, SUPRI-A.

Sincere thanks are given to Dr. Louis Castanier for his great help to my research. I can remember every time I knocked at the door of his office, saying 'good morning Louis', there is always a happy response from inside 'just a sec...' Sincere thanks are also due to Professor Margot Gerritsen, Professor Roland Horne and Professor Jonathan F. Stebbins for serving on the committee. Special thanks are given to ERE staff, Yolanda D. Williams and Joanna Sun.

My PhD research can not be finished without great help and supports from group mates and friends. It is my great happiness and gratitude to work with and to be friend with: Murat Cinar, Yangyang Liu, Mohammad Bazargan, Guenther Glatz, Berna Hascakir, Alexandre Lapene, Bolivia Vega, Zhouyuan Zhu, Qing Chen, Yang Liu, Saman Aryana, Egill Juliusson, David Cameron.

I would like to record my gratefulness here to my beloved wife, Xi Wang. She is the love and happiness to my life, giving me unconditional support to my career. Also thankfulness is due to my parents and family for their always being there in every aspect of my life.

Contents

Abstract	iv
Acknowledgements	vi
1 Introduction	1
1.1 Petroleum overview	1
1.2 In-situ combustion	2
1.3 Combustion kinetics	5
1.4 Statement of the problem	7
1.5 Thesis overview	8
2 Consistent RTO experiments and interpretation	12
2.1 Isoconversional principle	13
2.2 RTO experimental platform and simulator	15
2.3 Consistency	18
2.3.1 RTO simulations	18
2.3.2 RTO experiments	20
2.4 Repeatable RTO measurements	24
2.5 Conclusion	30
3 Isoconversional modeling and simulation	32
3.1 Defining kinetic parameters	34
3.1.1 Defining activation energy	37
3.1.2 Defining reaction orders	38

3.1.3	Defining pre-exponential factor	39
3.2	Kinetic interpretation for synthetic cases	39
3.2.1	Synthetic case of unit reaction orders	40
3.2.2	Synthetic case of non-unit reaction orders	41
3.2.3	Discussion	49
3.3	Kinetic interpretation and simulation	49
3.3.1	Gridding strategy	49
3.3.2	Kinetic reaction scheme	50
3.3.3	Alaskan oil sample	54
3.3.4	Karamay oil sample	62
3.4	Discussion	69
4	Isoconversional application	74
4.1	Reservoir matrix effect	74
4.1.1	Alaskan crude-oil cases	75
4.1.2	Karamay crude-oil cases	81
4.2	Coke formation investigation	87
4.2.1	Coke formed under air	88
4.2.2	Coke formed under nitrogen	94
4.2.3	XPS analysis	95
4.3	ISC candidate screening	98
5	RTO kinetics using electromagnetic radiation	107
5.1	Literature review	111
5.1.1	Microwave heating effect	111
5.1.2	Temperature measurement	113
5.1.3	Microwave heating system	115
5.2	Development of microwave heating systems	117
5.2.1	1st generation reactor and embodiments	117
5.2.2	2nd generation reactor and embodiments	121
5.2.3	3rd generation reactor and embodiments	126
5.2.4	Parallel electromagnetic heating system	133

5.3 Discussion	135
6 Summary and discussion	139
A Updates for the kinetic cell and combustion tube systems	143
B Background correction of effluent data	146
C Kinetic cell experiment preparation	150
D Codes for virtual kinetic cell simulation and isoconversional interpretation	152
E Input file of kinetic cell simulation for CMG-STARS	169
Bibliography	187

List of Tables

2.1	Kinetic cell designs	16
2.2	Arrhenius parameters for the synthetic model	18
2.3	Heat of reaction values for different simulation cases	20
3.1	Arrhenius parameters used in the synthetic case of unit reaction orders	41
3.2	Error analysis for the synthetic case of unit reaction orders	45
3.3	Arrhenius parameters used in the synthetic case of non-unit reaction orders	45
3.4	Error analysis for the non-unit reaction order case	45
3.5	Comparison between initial and adjusted values of pre-exponential fac- tor for the Alaska crude-oil combustion modeling.	62
3.6	Kinetic parameters for the proposed model of the Alaska crude-oil com- bustion.	62
3.7	Kinetic parameters for proposed model of the Karamay crude-oil com- bustion	64
4.1	Crude-oil/rock matrix pairs for RTO experiments	75
4.2	Oxygen consumption comparison of LTO and HTO for Alaskan crude oil cases	76
4.3	Oxygen consumption comparison of LTO and HTO for Karamay crude oil cases	82
4.4	Oxygen carbon ratios on the surface of different coke under air and nitrogen.	98

5.1	Comparison between microwave heating and furnace heating	110
5.2	Experimental conditions	121
A.1	Mass flow controller calibration table for air	144
A.2	Thermocouple enumeration for the kinetic cell system	144
A.3	Thermocouple enumeration for the combustion tube	145

List of Figures

1.1	In-situ combustion mechanism: (a), Schematic cartoon of a in-situ combustion process: heat is used to thin the oil and permit it to flow more easily toward production wells; in a fireflood, the formation is ignited, and by continued injection of air, a fire front is advanced through the reservoir; the mobility of oil is increased by reduced viscosity caused by heat and solution of combustion gases. (b), Illustration of temperature and saturation profiles in a typical in-situ combustion process: ① Injected Air and water zone (burned out); ② Air and vaporized water zone; ③ Burning front and combustion zone (600 - 1200 °F; ④ Coking zone; ⑤ Steam or vaporizing zone (Approx. 400 °F; ⑥ Condensing or hot water zone (50 - 200 °F above initial temperature); ⑦ Oil bank (near initial temperature); ⑧ Cold combustion gases.	11
2.1	Schematic diagram of RTO platform [17]: ① gas tank, ② mass flow controller, ③ electric furnace, ④ kinetic cell, ⑤ thermocouple, ⑥ back pressure controller, ⑦ gas analyzer, ⑧ computer.	16
2.2	Temperature profiles for the small temperature deviation (STD) case. For each temperature profile, the first hump represents the low temperature oxidation stage and the second hump represents the high temperature oxidation stage.	21

2.3	O_2 consumption profiles for the small temperature deviation (STD) case. For each O_2 curve, the first hump represents the low temperature oxidation stage and the second hump represents the high temperature oxidation stage. The valley between the two stages is the transition zone.	21
2.4	Temperature versus conversion for the small temperature deviation (STD) case. The curve of large heat rate is over the one of low heat rate. There is no intersection between different curves.	22
2.5	A plot of $\ln(d[X]/dt)$ versus $-1/(RT)$ for consistency check. The black solid lines connect dots of the same conversion X of different heat rates. Trends of each line are linear indication consistency. The slope represents the apparent activation energy at that conversion X	22
2.6	Activation energy fingerprints interpreted from the linear temperature (LT) case, the small temperature deviation (STD) case and the large temperature deviation (LTD) case using the integral isoconversional method.	23
2.7	Temperature histories for the RTO of Alaskan sample mixture: 13.3 °API, 45 grams of the sample mixture are used for each RTO experiment.	24
2.8	O_2 consumption histories for the RTO of Alaskan sample mixture: 13.3 °API, 45 grams of the sample mixture are used for each RTO experiment.	25
2.9	Temperature versus conversion for the RTO of Alaskan sample mixture: 13.3 °API, 45 grams of the sample mixture are used for each RTO experiment.	25
2.10	A plot of $\ln(d[X]/dt)$ versus $-1/(RT)$ for consistency check. The black solid lines connect dots of the same conversion X of different heat rates. Trends of each line are not linear for this measurement indicating inconsistent data. Alaskan sample mixture: 13.3 °API, 45 grams of the sample mixture are used for each RTO experiment.	26

2.11	Apparent activation energy fingerprint obtained from inconsistent data for the RTO of Alaskan sample mixture: 13.3 °API, 45 <i>grams</i> of the sample mixture are used for each RTO experiment.	26
2.12	Temperature histories for the RTO of Alaskan sample mixture: 13.3 °API, 25 <i>grams</i> of the sample mixture are used for each RTO experiment.	27
2.13	O ₂ consumption histories for the RTO of Alaskan sample mixture: 13.3 °API, 25 <i>grams</i> of the sample mixture are used for each RTO experiment.	27
2.14	Temperature versus conversion for the RTO of Alaskan sample mixture: 13.3 °API, 25 <i>grams</i> of the sample mixture are used for each RTO experiment.	28
2.15	A plot of $\ln(d[X]/dt)$ versus $-1/(RT)$ for consistency check. The black solid lines connect dots of the same conversion X of different heat rates. Trends of each line are linear for this measurement. Alaskan sample mixture: 13.3 °API, 25 <i>grams</i> of the sample mixture are used for each RTO experiment.	28
2.16	Apparent activation energy fingerprint obtained from consistent data for the RTO of Alaskan sample mixture: 13.3 °API, 25 <i>grams</i> of the sample mixture are used for each RTO experiment.	29
2.17	Activation energy fingerprints for three cases with different sample mass of identical composition. Case 1: KC1 is used, 18 <i>grams</i> of the mixture is used and air injection rate is 1 <i>L/min</i> ; Case 2: KC2 is used, 25 <i>grams</i> of the mixture is used and air injection rate is 1.5 <i>L/min</i> ; Case 3: KC3 is used, 10 <i>grams</i> , of the mixture is used and air injection rate is 1 <i>L/min</i>	30
3.1	Ramped temperature oxidation measurement data	35
3.2	Continuous flow reaction process during RTO	37
3.3	Simulation results for the synthetic case of unit reaction orders: 80% oxygen in the injection gas stream.	42

3.4	Simulation results for the synthetic case of unit reaction orders: 100% oxygen in the injection gas stream.	43
3.5	Activation energy fingerprints for unit reaction order cases of different oxygen compositions in the injection stream: both cases reveal similar fingerprints because of the identical reaction scheme.	44
3.6	Simulation results for the synthetic case of non-unit reaction orders: 80% oxygen in the injection gas stream.	46
3.7	Simulation results for the synthetic case of non-unit reaction orders: 100% oxygen in the injection gas stream.	47
3.8	Activation energy fingerprints for non-unit reaction order cases of different oxygen compositions in the injection stream: both cases reveal similar fingerprints because of the identical reaction scheme.	48
3.9	Radial gridding strategy ($4 \times 1 \times 7$ for $r \times \theta \times h$) to mimic the kinetic cell system in CMG-STARTS (the kinetic cell/furnace schematic diagram is adapted from a figure in Cinar's thesis [17].	51
3.10	RTO measured effluent data to identify reaction stages, CO_2/CO and O_2/CO	57
3.11	Isoconversional fingerprints for the four set of RTO experiments using different oxygen compositions in injection gas stream. The 35% oxygen case does not show consistent behavior as the other three cases. It is not used for the oxygen reaction order interpretation.	58
3.12	VKC simulation results based on the initial interpretation for values of activation energy, reaction orders, and pre-exponential factors A	59
3.13	VKC simulation results based on the adjusted pre-exponential factors A . Interpreted values of activation energies, reaction orders, and stoichiometry are kept the same as those in the initial interpretation simulation case. The heat rate is 1.85 K/min	60
3.14	Temperature history comparison between the VKC simulation result RTO measurement. The heat rate is 1.85 K/min	61
3.15	Isoconversional fingerprint comparison between the VKC simulation result and RTO measurement.	61

3.16	RTO measured effluent data to identify reaction stages, CO_2/CO and O_2/CO	65
3.17	Isoconversional fingerprints for the three set of RTO experiments using different oxygen compositions in the injection gas stream. The 35% oxygen case does not show consistent behavior as the other three cases. It is not used for the oxygen reaction order interpretation.	66
3.18	VKC simulation results based on the adjusted pre-exponential factors A. Interpreted values of activation energies, reaction orders, and stoichiometry are kept the same as those in the initial interpretations: The heat rate is 1.85 K/min	67
3.19	Temperature history comparison between the VKC simulation result RTO measurement: the heat rate is 1.85 K/min	68
3.20	Isoconversional fingerprint comparison between the VKC simulation result RTO measurement.	68
3.21	Alaskan crude oil RTO experiments: 35% oxygen composition.	71
3.22	Karamay crude oil RTO experiments: 35% oxygen composition.	72
3.23	Consistency check for the 35% oxygen composition RTO experiments of Alaskan crude oil.	73
3.24	Consistency check for the 35% oxygen composition RTO experiments of Karamay crude oil.	73
4.1	Alaskan crude oil case 1: 60 mesh fired sand and clay; 25g mixture of 2.04 wt% crude oil, 8.16 wt% water, 81.63 wt% fired sand and 8.16 wt% clay; Air injection rate is 1.5 L/min	77
4.2	Alaskan crude oil case 2: 60 mesh fired sand; 25g mixture of 2.04 wt% crude oil, 8.16 wt% water, 89.90 wt% fired sand; Air injection rate is 1.5 L/min	78
4.3	Alaskan crude oil case 3: 12 mesh fired sand; 25g mixture of 2.04 wt% crude oil, 8.16 wt% water, 89.90 wt% fired sand; Air injection rate is 1.5 L/min	79
4.4	Activation energy fingerprints comparison for Alaskan crude oil cases.	81

4.5	Karamay crude oil case 1: reservoir sand; 15g mixture of 2.04 <i>wt%</i> crude oil, 8.16 <i>wt%</i> water, 89.90 <i>wt%</i> fired sand; Air injection rate is 1.5 <i>L/min</i>	83
4.6	Karamay crude oil case 2: 60 mesh fired sand and clay; 25g mixture of 2.04 <i>wt%</i> crude oil, 8.16 <i>wt%</i> water, 81.63 <i>wt%</i> fired sand and 8.16 <i>wt%</i> clay; Air injection rate is 1.5 <i>L/min</i>	84
4.7	Karamay crude oil case 3: 60 mesh fired sand; 25g mixture of 2.04 <i>wt%</i> crude oil, 8.16 <i>wt%</i> water, 89.90 <i>wt%</i> fired sand; Air injection rate is 1.5 <i>L/min</i>	85
4.8	Activation energy fingerprints comparison for Karamay crude oil cases.	86
4.9	The kinetic cell for coke formation study in the isothermal condition.	89
4.10	Defining the termination temperature for the isothermal experiment of air coke formation: 300 °C is selected.	90
4.11	Coke is formed in the isothermal experiments.	91
4.12	RTO experiments for the Karamay air coke.	92
4.13	Comparison between the activation energy fingerprints for Karamay air coke and crude oil combustion: the activation energy values on fingerprint of air coke are very close to the values of HTO region on the fingerprint of crude oil.	93
4.14	Defining the termination temperature for the isothermal experiment of N ₂ coke formation: 420 °C is selected.	95
4.15	RTO experiments for the Karamay N ₂ coke	96
4.16	Activation energy fingerprint for Karamay N ₂ coke	97
4.17	XPS survey spectra of coke formation under air flow condition. Four spots are scanned.	99
4.18	XPS survey spectra of coke formation under nitrogen flow condition. Four spots are scanned.	100
4.19	High resolution XPS C 1s spectra of coke samples precipitated under air and nitrogen flow conditions	101
4.20	Unsuccessful combustion front propagation: (left) Combustion tube temperature profile and (right) isoconversional fingerprint [17].	102

4.21	Alaska crude oil combustion tube test with 60 mesh sand and clay. . .	104
4.22	Alaska crude oil combustion tube test with 60 mesh sand.	105
4.23	Karamay crude oil combustion tube test with reservoir sand.	106
5.1	Schematic diagram of microwave heating mechanisms: dipolar polarization and ionic conduction [26].	109
5.2	Temperature distribution difference between conventional and microwave heating [57].	110
5.3	Temperature (T), pressure (p), and power (P) profile for a 3 mL sample of methanol heated under sealed vessel single-mode microwave irradiation conditions to 165°C (external infrared temperature monitoring) [57].	116
5.4	Prototype of the 1st generation microwave heating system. The quartz tube reactor is hung inside the microwave oven cavity.	118
5.5	Metallic cap on the top of the microwave oven. A thermocouple is inserted through the cap. There are two connectors for injection and production gas respectively. The cap needs to be well grounded. . . .	118
5.6	Insulation material and its embodiment around the quartz tube reactor: during an experiment, crude oil sample is put at the bottom of the quartz cell. The body of the tube is wrapped by insulation material that is transparent to microwave, reducing heat loss to the oven cavity.	119
5.7	Shielded thermocouple and sintered SiC cylinders: sintered SiC cylinders are mixed with crude oil sample, acting as energy absorber to assist fast heating.	119
5.8	Schematic diagram of grounded circuit of a shield thermocouple. . . .	120
5.9	Experiment 1: effluent gas histories, 1st generation system.	122
5.10	Experiment 1: temperature profile, 1st generation system.	122
5.11	Experiment 2: temperature profile, 1st generation system.	123
5.12	Schematic design of the 2nd generation reactor.	125
5.13	The reactor embodiment based on a microwave oven.	126
5.14	The prototype of the 2nd generation microwave reactor.	127

5.15	The embodiment in a household microwave oven.	127
5.16	Shielded thermocouple and product filter connector.	128
5.17	2nd generation microwave heating system.	128
5.18	Schematic design of the 3rd generation reactor.	130
5.19	The prototype of the 3rd generation microwave reactor.	131
5.20	The embodiment in a household microwave oven, sintered SiC tube. .	132
5.21	The embodiment in a household microwave oven, sealing cap and quartz tube.	132
5.22	thermocouple and product filter connector.	133
5.23	Temperature profile of microwave heating of test 1, 3rd generation system.	134
5.24	Temperature profile of microwave heating of test 2, 3rd generation system.	134
5.25	Reactors based on microwave waveguides in a parallel manipulation. .	135
5.26	Schematic of reactor heated by RF radiation.	136
5.27	Induction heating with separate attenuator to achieve parallel heating.	137
5.28	Induction heating with different masses of RF absorber to achieve par- allel heating.	137
B.1	Temperature histories for RTO experiments.	148
B.2	149

Chapter 1

Introduction

1.1 Petroleum overview

Petroleum resources are categorized into conventional and unconventional resources. Conventional crude-oil is easier to recover and the reserves are estimated at around 3,012 billion barrels [126], over 50 percent of which resides in the Middle East. Roughly, 20-40% of the original oil in place (OOIP) of the conventional crude-oil is recoverable by primary and secondary processes. When using enhanced oil recovery (EOR) methods, 30-60% or more of the original oil in reservoir is produced. Technologies for conventional oil recovery have been well developed for many decades. Their field implementations are mature and economical. There have been some pessimists arguing that the depletion of petroleum resources would go to an end in the next 50 years. Their argument mostly regards conventional petroleum resources. More than 30 percent of the conventional resources has already been recovered to date[126].

Heavy oil and natural bitumen resources together contribute a total of 8,501 billion barrels to the world's unconventional crude-oil resources. It is further estimated that Canada and Venezuela alone possess heavy-oil resources that far exceed the world's conventional reserves [41]. Heavy oil has an API gravity between 10 and 20. It normally has little or no mobility under reservoir conditions due to its high viscosity. EOR technologies are needed for recovery of the original oil in the reservoir. Cyclic steam stimulation (CSS) and steam assisted gravity drainage (SAGD) are the two

major thermal EOR methods applied in heavy-oil reservoirs, however, a great amount of unconventional oil resource is still left behind waiting for further recovery. With the development of mature EOR technologies and the cost reduction of recovery processes, more concerns are needed for unconventional oil resources.

1.2 In-situ combustion

Heavy oil consists of a large portion of compounds of high molecular weight, such as resins and asphaltenes. This kind of crude oil flows with difficulty under initial reservoir temperature conditions because of its high viscosity. To recover commercially unconventional resources at economical production rates, it is critical to reduce the oil viscosity so that the crude oil can be moved towards the production well by external forces of pressure and gravity. One of the practical ways to decrease crude-oil viscosity is heating up the reservoir by the injection of hot water or steam from the ground surface. The techniques of CSS and SAGD have been applied worldwide [92], however, their shortcomings are apparent when these two thermal EOR methods are applied to reservoirs that are deep or lying under permafrost. Wellbore heat loss is significant for deep reservoirs and it greatly reduces the efficiency of an operation. Another practical way to introduce a heat source is to burn a certain amount of crude-oil in situ within the reservoir and let the combustion zone sweep the resource. This EOR method is called in-situ combustion (ISC) or fire-flooding.

In-situ combustion is considered as the most energy efficient and least atmospheric impact thermal EOR method [71]. During an ISC process, a small fraction of crude-oil is burned in situ, releasing heat from exothermic reactions. Meanwhile, pressure is elevated because of the intensive energy released from a very thin reaction zone, and the elevated pressure acts as one of the drainage mechanisms to push the crude oil towards a production well. Last but not least is the upgrading of the crude oil in-situ. Light or condensate crude oil composition is vaporized from the reaction zone and transported forward. Because the crude-oil burned is mainly the heavy fraction, light components are vaporized or separated from the mixture by the high temperature and these components then travel forwards downstream ahead of the oxygen front.

Although ISC is regarded as an EOR method with great potential, it is much more complicated than other thermal EOR methods. The physics of ISC include complex reaction kinetics, multiple displacement mechanisms and intensively changing phase dynamics. The ISC process is schematically described in Figure 1.1. A certain amount of crude oil is ignited by a heater within the injection well, and the continuously feeding air sustains the propagation of a high temperature combustion front moving from the injection well towards the production well. In the direction of the combustion front, several zones are observed [41]. The burned zone is the volume swept by the combustion front. In most of the cases the burned zone is very 'clean' or leaving behind very few burned residues. The combustion zone is a very thin zone with high temperature where oxygen reacts with crude-oil residues and the reactions are intensively exothermic, generating carbon oxides and water. Adjacent to the combustion zone is the coke zone. Effluent gas composed of nitrogen and carbon oxides penetrates the high-temperature front. Meanwhile, heat conduction from the combustion zone cracks the crude oil residues under this inert gas environment, forming so-called pyrolysis coke deposited on the rock surface. The coke is the main fuel source for the combustion. In front of the coke zone is the liquid vaporized zone, where temperature is still high enough to keep the condensable gas in the gas phase, such as steam and very light hydrocarbons, forming a steam plateau. Moving ahead of the vaporized zone is the steam condensate zone. The temperature here drops below the steam saturation temperature and a hot water bank is formed. Further ahead is the oil bank, where part of the oil is upgraded by mixing with light condensate hydrocarbons [84][10][41]. The driving mechanism in the ISC process is a combination of reduction in oil viscosity because of the elevated temperature, gas drive from reaction effluent gas, steam drive from the condensate water in the steam zone downstream of the combustion zone, upgraded oil by the mixing of condensate light oil component with the original crude oil, etc [17].

The ISC process was first patented in 1920 in the USA [102]. Since then, much research on this thermal EOR process has been conducted in both laboratory and pilot scale. Commercial ISC projects around the world reached a maximum of 19 during the period of 1970's to 1990's. The daily oil production from ISC was about

32,000 barrels of oil per day (BOPD) in 1992 [102]. Only 4 commercial ISC projects, however, are active currently. The daily oil production is around 3,770 BOPD [102]. The high cost of production is the major reason to shutdown many ISC projects, while other project failures were caused by incorrect operations on air injection, ignition, etc. [72]. The successful commercial ISC projects and their advantages, such as high efficiency in oil recovery, encourage us keep to working on this thermal EOR method. Meanwhile, the technical reasons for the decreasing frequency of commercial projects gives lessons that more research on reliable numerical and experimental tools for accurate and efficient prediction of field performance are needed so that sophisticated operations on a ISC project can be carried out [41].

Extensive research on the ISC process has been done regarding a wide range of topics. Many fundamental studies have been conducted experimentally in kinetic research systems, lab-scale combustion tube tests and pilot investigations, or by simulations of the kinetic study to field production to unlock the characteristics of this EOR process.

Experimental observation to identify global reaction stages is fundamental, using temperature or flue gas concentration recording techniques, such as thermogravimetric analysis and differential scanning calorimetry (TGA/DSC) or effluent gas analysis [60][7][8]. At least two oxidation stages, LTO and HTO were claimed. Other studies confirmed a transition reaction stage in between the LTO and HTO referred to as medium temperature oxidation or fuel formation stage [8][41]. Rather than diving into detailed elementary reaction schemes, reaction kinetic modeling is conducted based on the identification of reaction stages. The reaction modeling procedure has two phases, proposing a reaction mechanism scheme and defining kinetic parameters for a rate law model [6][32]. Lumping crude oil components as reactants in the reaction scheme is common. The crude oil can be treated as a bulk species [17][23], or divided into reaction functional groups such as maltenes and Asphaltenes [48][6][2] or a SARA (Saturates, Aromatics, Resins, and Asphaltenes) model [34], or partitioned by light or heavy fractions [20]. When the reaction scheme is ready, post-processing the measured data to interpret kinetic parameters is needed to define activation energy,

pre-exponential factor and reaction orders. Besides the kinetics investigation, laboratory combustion tube tests are another perspective to investigate reaction behaviors. Normally a combustion tube of stainless steel is a meter in length and roughly 10 *cm* in diameter. Insulation materials are needed to reduce heat loss from the tube to the ambient environment [17]. The combustion tube is very useful to monitor temperature propagation performance under different reservoir conditions [46] or at different operation modes, such as wet combustion and solvent injection [41].

Simulation study of the crude-oil combustion performance has three perspectives. validating the model in simulations of the kinetic measurement system, like a kinetic cell system [17], investigating ISC performance in 1-D combustion tube simulations [40] and field-scale simulations [124]. A reaction kinetic model is coupled with a reservoir simulator to mimic the combustion behavior under certain conditions. The simulation is very necessary to understand the ISC progress and analyze some important factors that can not be measured or detected in an experiment. Also, sensitivity studies are useful to optimize the operation [75].

1.3 Combustion kinetics

There is no doubt that research of the kinetics of crude-oil oxidation is fundamental and critical because the reaction zone during an ISC process is well governed kinetically by the inherent reaction mechanism.

A typical heavy crude oil consists of hundreds of components and its reactions with oxygen are numerous. Experimental capability is very limited to derive the reaction paths in detail. An empirical approach is more practical and generally applied. Based on effluent gas analysis, three reaction stages are observed: low temperature oxidation (LTO) with temperatures of 150 - 300°C, medium temperature reaction, with temperatures of 300 - 450°C, and high temperature oxidation (HTO) with temperatures above 400°C [41][10]. In the LTO regime where reactions are considered as heterogeneous gas/liquid reactions, oxygen diffuses from the gas stream, adsorbs on the surface and reacts with hydrocarbon components producing partially oxygenated compounds (e.g. alcohols, ketones, aldehydes) and few carbon oxides. The medium

temperature regime undergoes a series of cracking or pyrolysis reactions, generating coke that is the main source for the HTO reactions. After the medium temperature regime, coke is burned in the HTO stages, generating carbon oxides and water. The reactions in HTO are believed to be gas/solid heterogeneous reactions that result in bond breaking [31] [32].

It is widely accepted that the overall reaction is controlled by the reaction kinetics. Studying reaction kinetics consists of two phases: proposing a reaction mechanism (or reaction scheme) and building a reaction model for each reaction from measurement interpretation or mathematical treatment. An appropriate workflow combining well-designed experiments and a reliable data interpretation tool is essential for conducting reliable performance predictions of ISC by simulations. Based on all of the research on crude-oil combustion kinetics, we may classify them into conventional methods and isoconversional methods.

The conventional method needs a presumed reaction model to process data fitting on measured values. Boiusaid and Ramey were the first to carry out isothermal experiments in a combustion cell system [8]. Experiments at different constant temperatures were conducted, reaction order of oxygen partial pressure was assumed unit, and data fitting strategy was processed to estimate the activation energy and the Arrhenius constant. The method is straightforward, but the isothermal condition is not easy to achieve due to the exothermic reactions of crude-oil combustion, and the attempt does not simulate true frontal reaction behavior in the reservoir that is under high temperature and in a short period of time [31].

Therefore, non-isothermal experimental conditions attract more concern in later studies. Thermogravimetric analysis (TGA) and Differential Scanning Calorimetry (DSC) analysis are widely applied to define combustion parameters, such as heat value of crude-oil reaction, amount of fuel laid down, hydrogen/carbon (H/C) ratio and minimum front temperature [4][111][6]. Using TGA/DSC, a successful reaction model was developed by Vossoughi et al. [109] that can predict fuel deposition and combustion rate in combustion tube runs of crude oil of 19.8° API. Fassihi et al. [31][32] proposed a non-isothermal experimental procedure for crude-oil combustion study. The ramped temperature oxidation system consists mainly of a combustion

cell located in a furnace, three continuous gas analyzers, temperature, and flow rate recording components. Post-processing of measured data used conventional interpretation methods where the order of reaction with respect to fuel concentration needs to be assumed. A trial and error procedure is needed to estimate the reaction orders. The relation between oxygen consumption rate and carbon consumption is used to derive the change in oxygen concentration [31][32][17].

Cinar et al. [17] was the first to introduce the isoconversional principle to interpretation of RTO experiments. The isoconversional principle, with its model-free character, deconvolves the complicated multi-component, multi-step reaction kinetics during the ISC process. No reaction model is needed a priori, activation energies are described in the so-called isoconversional fingerprint as a function of conversion factor. Reaction stages, such as LTO and HTO are easily identified from the fingerprint. Furthermore, the negative temperature gradient region (NTGR) [70] where a local minimum in activation energy versus temperature is observed. The NTGR is also referred to as 'Death Valley', in which the reaction rate decreases as temperature increases, and its exist challenges the sustainability of ISC [22][17].

1.4 Statement of the problem

In-situ combustion (ISC) is a complicated thermal enhanced oil recovery (EOR) method because of the multi-component character of crude-oil, multi-phase behavior, and intense energy release in a very thin reaction zone. It is even more complicated when we take the heterogeneity of reactant and the rock matrix into consideration. Many fundamental studies have been conducted experimentally or by simulation to unlock the characteristics of this EOR process. Experimental research includes kinetic study to build a reaction model [1][14], combustion tube tests to monitor temperature front propagation at lab scale [46], and pilot test in a small field scale [103]. Simulation studies involve kinetics modeling [6], 1D, 2D and 3D tube simulations [40] and field-scale simulation [124].

Among all of this research, studying the reaction zone behavior is basic and critical, because the temperature which is the most critical index to judge the performance

of a ISC process is controlled by the reaction kinetics within the reaction zone. Understanding the reaction kinetics helps to optimize control of the ISC process. Building a sophisticated reaction model and coupling it with a reservoir simulator is the direction to investigate the reaction performance during the ISC process. Therefore, defining the parameter values from experimental measurement rather than from mathematical treatment is more physically meaningful.

The workflow of conducting RTO experiments and then processing data using isoconversional interpretation is considered as one of the promising ways to deconvolve the complicated reaction mechanism of ISC. RTO experiments work in a non-isothermal condition which has many advantages against isothermal experiments with respect to wider temperature range and ease of handling. The isoconversional principle is a model-free data interpretation method that naturally separates activation energy from the reaction model. Processing the workflow correctly should be the baseline for any proposed experimental strategy. Meanwhile, RTO experiments contain all of the reaction behavior under different heat rate measurements. A practical way is needed to extract as many kinetic parameters as possible to make the reaction model reliable and physically accurate.

1.5 Thesis overview

The dissertation consists of four major topics. The first topic is to investigate by simulation and experiment how to conduct consistent RTO experiments for isoconversional interpretation of the activation energy fingerprint. The second topic is combining the isoconversional principle together with conventional interpretation methods to extract kinetic parameters for building reaction models. The third topic is applying the isoconversional principle to investigate rock surface area affects on the ISC reaction kinetics, formation coke characters and kinetic behavior, and screening ISC candidates of different crude-oil/rock-matrix pair. The fourth topic is designing a microwave heating system to take place of the conventional furnace system for RTO experiments.

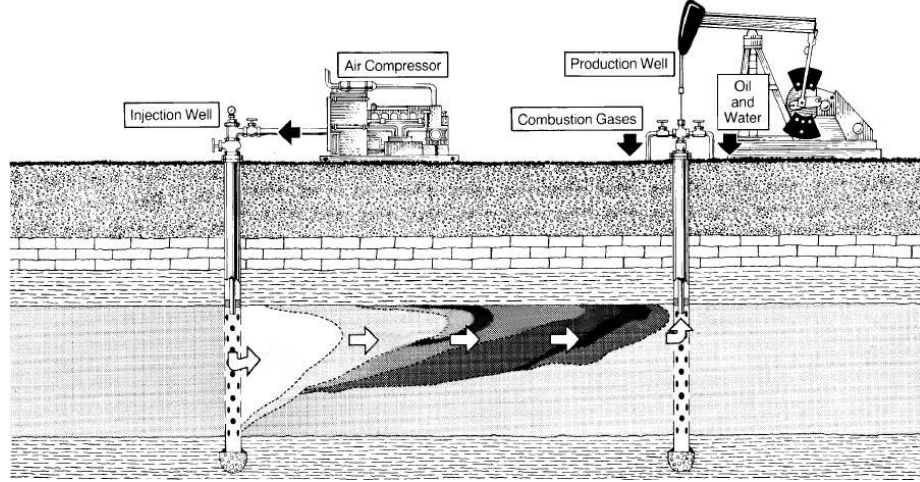
The consistency of RTO experiments and isoconversional interpretation is discussed in Chapter 2. Basic theory for the isoconversional principle is introduced. Governing equations describing both mass balance and energy balance are coded to develop a virtual kinetic cell (VKC) simulator, in which different reaction schemes are coupled and temperature as well as effluent gas profiles at various heat rates are calculated. The VKC is a useful tool to mimic crude-oil combustion occurring within a kinetic cell. Simulations studies showed that reducing temperature deviations caused by exothermic reactions is critical and have the RTO measurement consistent and thus a stable activation energy fingerprint. RTO experiments with the same crude oil mixture under different working conditions including kinetic cell design, air injection rate, and sample mixture size, support the argument from the VKC simulation analysis.

Building a reaction model requires definition of reaction parameters, including activation energy, pre-exponential factor, and reaction orders for reactants. Chapter 3 describes a way to combine the isoconversional principle with conventional interpretation to extract kinetic parameters from RTO measured data. Simulations in the VKC with two simple synthetic models demonstrate great capability of this method for interpretation. A three-reaction scheme is proposed based on the observation and analysis of the isoconversional fingerprint and effluent data. The kinetic parameter values are defined from a series of RTO experiments for combustions of two crude-oil sample mixtures. Good history match is achieved by simulations of VKC in the commercial reservoir simulator CMG-STARs.

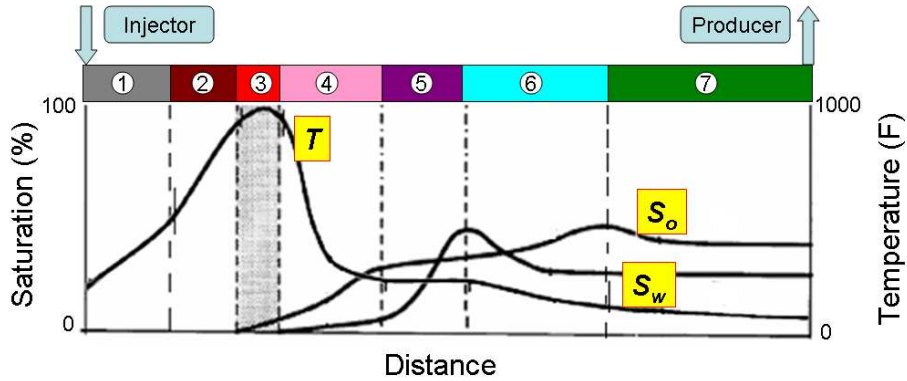
Chapter 4 expands the application of the isoconversional principle to investigate other aspects of crude-oil combustion. Further discussion on analyzing the activation energy fingerprint is included. Rock surface effect on kinetics of crude-oil combustion is observed by the fingerprint comparison between experiments of the same crude-oil but different rock matrix. The kinetic characters of coke formation under air flowing or inner gas flow condition is studied by RTO experiments and isoconversional analysis. X-ray photoelectron spectroscopy (XPS) is used to scan the coke surface to identify whether oxygen is involved with coke formation. Because the isoconversional fingerprint shows the apparent activation energy values, that responds to not only the

component reaction itself, but also to mechanisms like rock surface area and phase reactions. The fingerprint is treated as a diagnostic tool to select the potential ISC candidates of crude-oil/rock matrix pair. According to the screening criterion, a smooth activation energy fingerprint without an energy barrier in the early reaction period corresponds to a good ISC candidate. Combustion tube tests of three crude-oil/rock-matrix pairs support this argument.

Chapter 5 explores the use of electromagnetic heating methods within the laboratory. RTO experiments need to heat up the crude-oil mixture at different heating rates. The low efficiency of a conventional furnace kinetic cell system motivates us to find a new way to heat up the sample and to control the temperature. This chapter discusses development of a microwave heating system to process RTO experiments. Electromagnetic heating has many advantages compared to the conventional furnace heating, such as faster heat rate and shorter cooling cycle. Three generations of the microwave heating system are demonstrated. Preliminary tests on the system obtained a maximum temperature value around 500°C. The problems of building the system are discussed and future plans for improving the system are proposed.



(a) Schematic cartoon of a in-situ combustion process [125].



(b) Illustration of temperature and saturation profiles in a typical in-situ combustion process [41].

Figure 1.1: In-situ combustion mechanism: (a), Schematic cartoon of a in-situ combustion process: heat is used to thin the oil and permit it to flow more easily toward production wells; in a fireflood, the formation is ignited, and by continued injection of air, a fire front is advanced through the reservoir; the mobility of oil is increased by reduced viscosity caused by heat and solution of combustion gases. (b), Illustration of temperature and saturation profiles in a typical in-situ combustion process: ① Injected Air and water zone (burned out); ② Air and vaporized water zone; ③ Burning front and combustion zone (600 - 1200 °F; ④ Coking zone; ⑤ Steam or vaporizing zone (Approx. 400 °F; ⑥ Condensing or hot water zone (50 - 200 °F above initial temperature); ⑦ Oil bank (near initial temperature); ⑧ Cold combustion gases.

Chapter 2

Consistent RTO experiments and interpretation

The multi-component character of crude-oil contributes to the complexity of crude-oil combustion. It is almost impossible to identify every component in the crude mixture and elementary reactions of each component correlated with oxidation gas and high temperature. Therefore, lumping strategies for crude-oil components and for different stages of reactions are practical and persist [106] [107]. Interaction between components is a critical factor because the mixing rule is neglected. Taking the crude-oil mixture as a bulk material and phase behavior controlled by PVT data are considered as a more promising strategy. In this method, both series and parallel reactions at different phases are lumped respectively according to measured data, and the corresponding apparent activation energies are interrupted. Reaction models are built based on temperature profiles and effluent gas histories. It is commonly accepted that at least two reaction stages exist, fuel deposition and fuel burning. This goes to a point that we need mature measurements as well as robust tool to interpret parameter values.

One way to investigate the reaction kinetics of ISC is to apply ramped temperature oxidation (RTO) experiments within a kinetic cell system which is a continuous flow stirred tank reactor (CSTR), and use an interpretation tool to get the values for

kinetic parameters. Because of the complicated reaction mechanism, while conducting experiments, we need to reduce factors that have influence on the experimental result. Meanwhile, we need to make the measurement reliable. According to the model-free assumption of the isoconversional principle, a repeatable measurement is critical to convince us that this principle can be applied to interpret global activation energy from well-designed experiments. This goes to the heart of the consistency issue. In this chapter, the basic theory of the isoconversional principle is introduced, the RTO experimental platform is briefly described, and a simple kinetic cell simulator is developed to demonstrate how to operate the experiment correctly so that the isoconversional principle can be applied to post process the measurements. The consistency issue is studied by simulation and experiments. Also, the results supported the model-free character of isoconversional principle and it is promising to unlock the complicated reaction kinetic mechanism of ISC.

2.1 Isoconversional principle

One fundamental and critical study of ISC reaction kinetics is to evaluate kinetic parameters, such as activation energy. We can categorize this study into conventional interpretation [31][32] and isoconversional interpretation [15]. Generally, the ISC reaction rate is described as a product of a rate constant $k(T)$ and a global reaction model $f(C)$

$$-\frac{dC}{dt} = k(T)f(C) \quad (2.1)$$

where $k(T)$ is a function of temperature T and $f(C)$ is a function of species concentration C . In ISC modeling, commonly $k(T)$ is expressed using the Arrhenius rate law

$$k(T) = A \exp\left(-\frac{E}{RT}\right) \quad (2.2)$$

where A is the pre-exponential factor, E is the activation energy, and R is the universal gas constant. The reaction model is commonly considered as a function of fuel

concentration and oxygen partial pressure, and that is

$$f(C_f) = P_{O_2}^a C_f^b \quad (2.3)$$

where C_f is the fuel concentration, P_{O_2} is the partial pressure for oxygen, a and b are reaction orders for oxygen and fuel respectively. Substituting Eq. (2.2) and Eq. (2.3) into Eq. (2.1), we obtain a rate equation describing ISC reaction kinetics

$$-\frac{dC_f}{dt} = A \exp\left(-\frac{E}{RT}\right) P_{O_2}^a C_f^b \quad (2.4)$$

Because of the complicated character of the ISC reaction mechanism, well designed experiments and robust interpretation tools are needed to define the activation energy E , the pre-exponential factor A , and reaction orders, a and b . In this study, we only focus on defining the activation energy. Kinetic cell experiments are conducted and the isoconversional principle is applied to get the E values.

Conventional interpretation methods include isothermal and non-isothermal attempts. The isothermal method is based on Eq. (2.4) [8]: isothermal experiments are conducted at several constant temperatures and reaction rates are estimated. The reaction order for oxygen is assumed to be unit. This method is straightforward, but it needs isothermal conditions that are difficult to achieve and impossible to carry out experiments in a wide range of temperatures. The non-isothermal method was developed to overcome the difficult working condition of isothermal method [31][32]. Here, the order of reaction with respect to carbon concentration needs to be known a priori, so a trial and error procedure is needed to estimate the reaction orders. The isoconversional method is a more promising principle than the conventional method because it is a model-free technique and the interpretation is based on multiple ramped temperature measurements. This principle was first devised by Friedman [35]. Its critical statement is that at a given extent of conversion, the reaction rate is only a function of temperature. In terms of fraction of conversion X , Eq. (2.4) is rewritten as:

$$-\frac{dX}{dt} = A \exp\left(-\frac{E}{RT}\right) f(X) \quad (2.5)$$

Taking the logarithm of both sides of Eq. (2.5) gives

$$\ln \left(-\frac{dX}{dt} \right) = \ln(A) + \ln[f(X)] - \frac{E}{RT} \quad (2.6)$$

According to the isoconversional theory, at a constant extent of conversion X , $\ln(A)$ and $\ln[f(X)]$ are constants. By plotting $\ln \left(-\frac{dX}{dt} \right)$ versus $\frac{1}{RT}$, the slope of the straight line is the activation energy at that conversion X . This method is also called the differential isoconversional method [35]. Because of the noise sensitivity of the differential method for measurement data, Vyazovkin described an integral isoconversional method and its improvement to overcome the shortcomings of the differential method [112] [115]. The critical part of the integral method is to solve the minimum function of

$$\Phi(E_X) = \sum_i^n \sum_j^n \frac{J[E_X, T_i(t_X)]}{J[E_X, T_j(t_X)]} = \min, \quad i \neq j \quad (2.7)$$

in which J is

$$J[E_X, T(t_X)] = \int_{t_X - \Delta X}^{t_X} \exp\left(-\frac{E_X}{RT(t_X)}\right) dt \quad (2.8)$$

2.2 RTO experimental platform and simulator

To apply the isoconversional principle for the activation energy interpretation, RTO experiments are carried out. Figure 2.1 shows the experimental platform. The key components of the system include a kinetic cell (i.e., reactor), an electric furnace, a mass flow controller, a back-pressure controller, thermocouples, a gas analyzer, gas supplies, and a computer. The oil sample mixed with crushed rock matrix of sand is put inside the cell chamber. The preheated oxidation gas is injected through the bottom of the cell and contacts with the oil sample. Meanwhile, heat from the furnace ramps the cell temperature at a specified heat rate. The temperature histories as well as corresponding gas compositions are recorded. These data are used to interpret kinetic parameters.

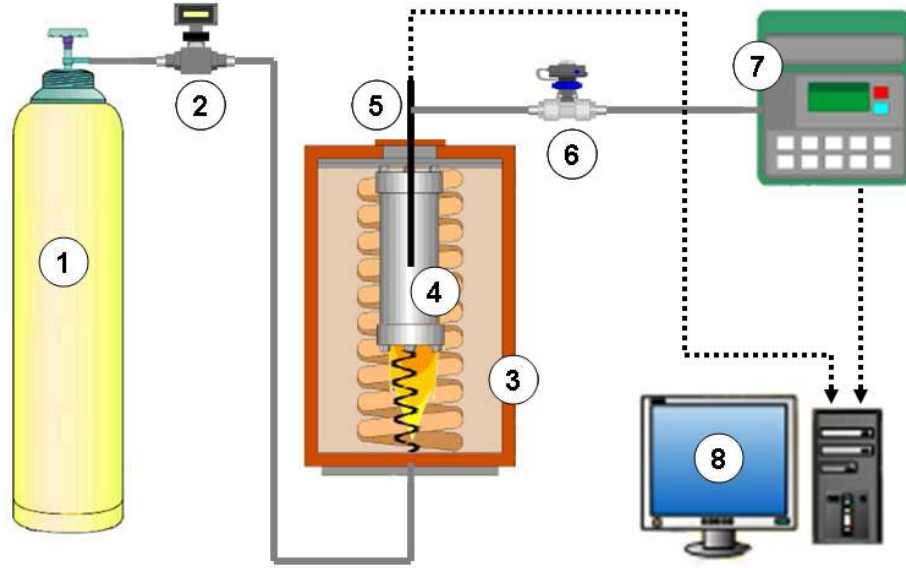


Figure 2.1: Schematic diagram of RTO platform [17]: ① gas tank, ② mass flow controller, ③ electric furnace, ④ kinetic cell, ⑤ thermocouple, ⑥ back pressure controller, ⑦ gas analyzer, ⑧ computer.

Table 2.1: Kinetic cell designs

Unit: cm	I.D	length	well thickness	material
Kinetic cell 1 (KC1)	3.1	12.0	1.8	stainless steel
Kinetic cell 2 (KC1)	3.1	12.0	0.5	stainless steel
Kinetic cell 3 (KC3)	1.4	15.2	0.3	carbon steel

Three different kinetic cells are used (KC1, KC2 and KC3). The chamber dimension and the well thickness of each cell are listed in Table 2.1. The KC1 and the KC2 are conventional cells, and KC3 is the induction cell [90]. KC2 has a thinner wall than KC1 so that the temperature difference between the furnace and the cell chamber is reduced. For each cell, a certain amount of fired sand is filled at the bottom part for gas dispersion, the oil/sand mixture is put in the center of the cell and the rest of the chamber volume is filled with fired sand. The sample mixture within the chamber is treated as zero-dimensional so that the kinetic cell is considered as a differential reactor.

During an RTO experiment, the oxidation gas is preheated to the same temperature as that within the kinetic cell before injection. The gas reacts with the oil sample for the period of residence time Δt , and then the effluent gas flows out of the cell chamber. This process is modeled as a CSTR process [43] [14]: 1. the fuel only exists inside the reactor cavity because of the liquid phase or solid phase; 2. steady state is considered for the gas reacting with fuel mixture so that the accumulation term for gas species is zero.

Here are the governing equations describing the mass balances of liquid/solid phase

$$-\frac{dC_{f,i}}{dt} = r_{f,i}, \quad i = 1, 2, \dots, n \quad (2.9)$$

and gas phase

$$0 = \frac{F_{g,j,in} - F_{g,j,out}}{V} + r_{g,j}, \quad j = 1, 2, \dots, m \quad (2.10)$$

and the temperature variation

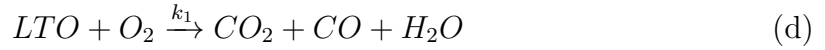
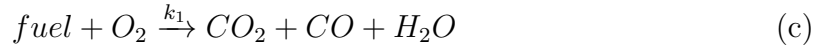
$$V \frac{dT}{dt} = \frac{\dot{Q} - \sum_{j=1}^m F_{j,out} C_{P_j} (T - T_{j,in})}{\sum_{i=1}^n C_i C_{P_i} + \sum_{j=1}^m C_j C_{P_j}} + \frac{\sum_{i=1}^n \Delta H_{R,i}(T) (r_i V)}{\sum_{i=1}^n C_i C_{P_i} + \sum_{j=1}^m C_j C_{P_j}} \quad (2.11)$$

where $r_{f,i}$ and $r_{g,j}$ are net reaction rates for a liquid/solid phase and a gas phase species respectively. $F_{g,j}$ is molar flow rate of species j , V is the void volume of the cell chamber, \dot{Q} is the heat flux from the furnace, C_P is the heat capacity, and ΔH_R is the reaction enthalpy. The CSTR simulator is coded in MATLAB.

A synthetic scheme of four reactions is used in the simulator. The reactant *fuel* is the original crude-oil and *fuel** is the intermediate component. Reaction (a), (b) and (d) are series reactions. Reaction (c) is the parallel reaction. For each reaction, reaction orders for oxygen and fuel are unit. Arrhenius parameters are listed in Table 2.2.

Table 2.2: Arrhenius parameters for the synthetic model

Reaction	(a)	(b)	(c)	(d)
Pre-exponential factor $L/(mole \cdot s)$	1	2.93×10^5	100	100
Activation energy $J/(mole \cdot k)$	63000	75000	125000	12000



Four-reaction synthetic reaction scheme.

Simulations of different heating rates are carried out. The O_2 consumption and the temperature histories are recorded. Both differential and integral isoconversional methods are applied to process the data.

2.3 Consistency

2.3.1 RTO simulations

When applying the isoconversional principle to interpret apparent activation energy from measurement data, the validation of this principle in a real kinetic experiment needs to be investigated. This goes to the experimental consistency issue. Cinar et al. [17] discussed some qualitative ideas to judge whether the measurements are consistent or not. More analysis is needed to show how to work on kinetic experiments correctly so that the measurements are consistent. This is significantly important to make the measurement repeatable even with a different kinetic cell device [90]. In

this subsection, simulations based on the synthetic model are discussed to show how we should handle our experiments.

According to Eq. (2.6), the differential method has the basic principle for isoconversional method: at a certain extent of fraction conversion X , $1/(RT)$ and $\ln(\frac{dX}{dt})$ form a straight line and the slope of which is the apparent activation energy. Friedman performed experiments of the thermal degradation of plastic at different linear heating rates. The isoconversional fingerprint interpreted from the TGA measurement matched the documented result [35]. For crude-oil RTO experiments, because of the intensive heat released from crude oil oxidation and the temperature control strategy in which the furnace temperature is linearly prescribed, temperature within the kinetic cell is very difficult to achieve a linear trend. Apparently, a rigorous test of the consistency of experimental data for use in the isoconversional method has never been discussed. The temperature deviation and its effect on the isoconversional application are studied here as well. In the simulator where the temperature profiles are calculated using the energy balance equation, the temperature deviation because of the heat released is controlled by the values of reaction enthalpy. Linear temperature histories are achieved by zero reaction enthalpies, and increasing the reaction enthalpies increases the temperature deviations on the temperature histories.

Three cases are considered which are a linear temperature case (LT), a small temperature deviation case (STD) and a large temperature deviation case (LTD). The reaction enthalpies for each case are listed in Table 2.3. The LT case is an ideal case without temperature deviation, and its activation energy fingerprint is well interpreted by the isoconversional principle. The LTD case is an extreme case in which a large amount of heat is released causing big temperature deviations of the temperature profiles. In this study, the STD case is analyzed and the activation energy result is compared with the LT and the LTD cases.

Figures 2.2 and 2.3 show the temperature and the oxygen consumption profiles at different heat rates respectively. Two reaction stages, that are the low-temperature oxidation and the high-temperature oxidation regions, are observed according to the O_2 consumption humps. Figure 2.4 shows temperature versus conversion X at each heat rate. The curves of large heat rates are above those of low heat rates and there is

Table 2.3: Heat of reaction values for different simulation cases

	Reaction (a)	Reaction (b)	Reaction (c)	Reaction (d)
LT	0	0	0	0
STD	-80000	40000	-100000	-100000
LTD	-100000	40000	-120000	-120000

no intersection between different curves. Figure 2.5 shows the consistency check plot, in which the black solid lines represent the apparent activation energies according to the isoconversional principle. The plot shows a linear trend of each line. Figure 2.6 shows the activation energy fingerprints obtained by the integral isoconversional method. The STD fingerprint matches the LT fingerprint which is the ideal case, and both of them represent the activation energy values listed in Table 2.2. For the LTD case, the fingerprint represents the low temperature oxidation stage well, but there is an oscillation at the high temperature oxidation stage. This oscillation is due to the big temperature deviation caused by the large amount of heat released.

Based on the simulation results, a consistent measurement should follow: 1. when plotting temperature versus conversion, larger heat rate curves should lie over lower heat rate curves and there is no intersection between curves; 2. when plotting $\ln(d[X]/dt)$ versus $-1/(RT)$, the connection for data points of different heat rates at the same conversion should follow a linear trend and this trend is the activation energy at that conversion X ; 3. because of the much more complicated reaction kinetics for a real case of the crude oil combustion, big temperature deviations should be avoided.

2.3.2 RTO experiments

Lab measurements of kinetic parameter are much more difficult because of the complicated compositional character of crude-oil samples and the combustion mechanism. Meanwhile, the noise introduced by temperature recording and from gas analyzer data drift make it hard to obtain consistent measurement. Much effort is needed to manage consistent measurements. According to the conclusion from simulations, a

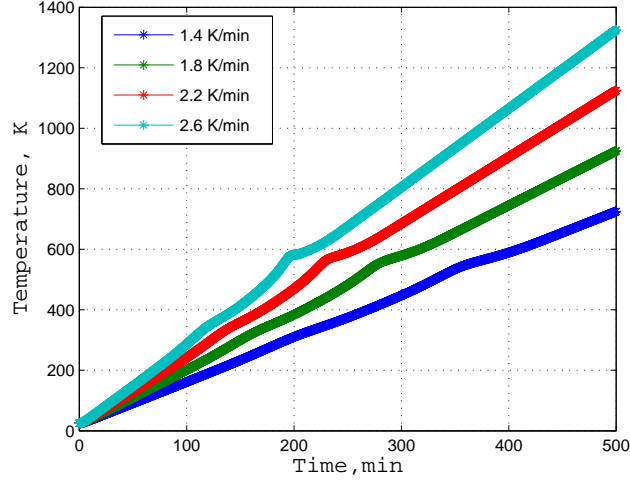


Figure 2.2: Temperature profiles for the small temperature deviation (STD) case. For each temperature profile, the first hump represents the low temperature oxidation stage and the second hump represents the high temperature oxidation stage.

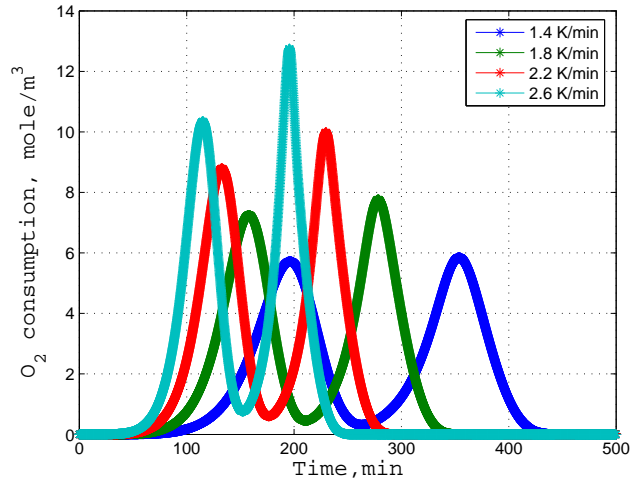


Figure 2.3: O_2 consumption profiles for the small temperature deviation (STD) case. For each O_2 curve, the first hump represents the low temperature oxidation stage and the second hump represents the high temperature oxidation stage. The valley between the two stages is the transition zone.

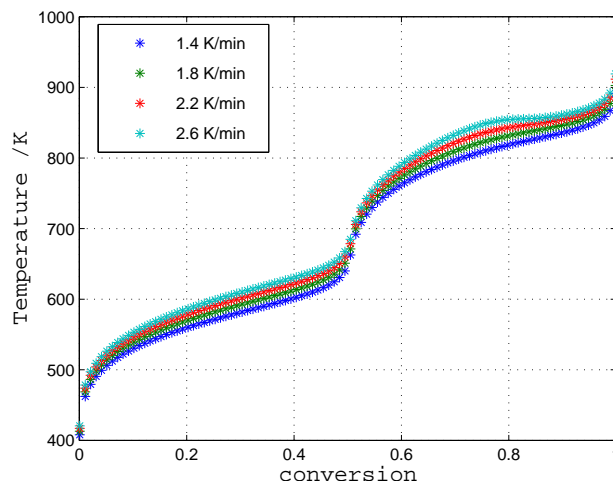


Figure 2.4: Temperature versus conversion for the small temperature deviation (STD) case. The curve of large heat rate is over the one of low heat rate. There is no intersection between different curves.

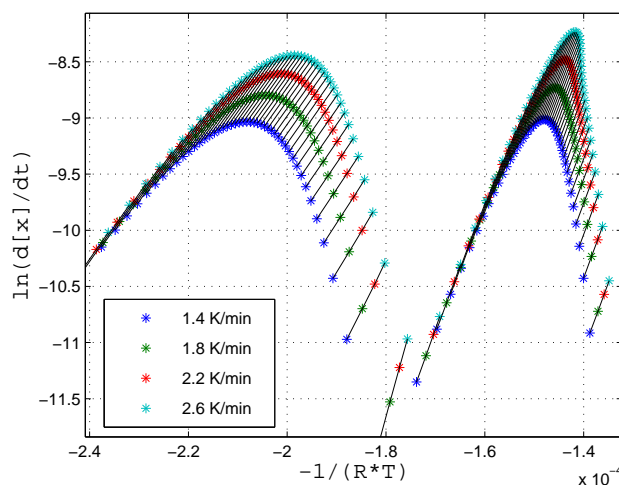


Figure 2.5: A plot of $\ln(d[X]/dt)$ versus $-1/(RT)$ for consistency check. The black solid lines connect dots of the same conversion X of different heat rates. Trends of each line are linear indication consistency. The slope represents the apparent activation energy at that conversion X .

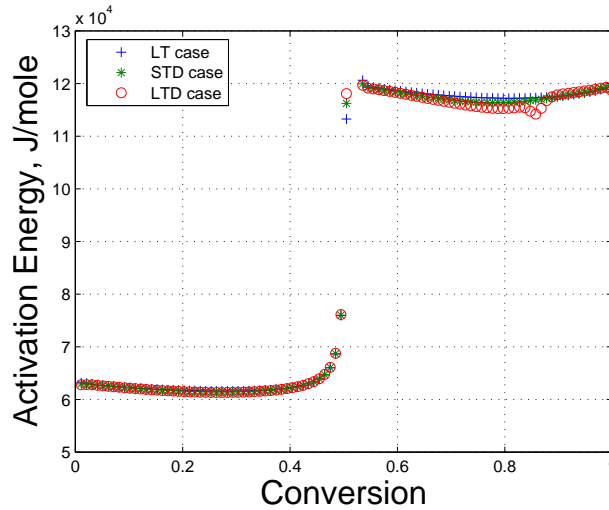


Figure 2.6: Activation energy fingerprints interpreted from the linear temperature (LT) case, the small temperature deviation (STD) case and the large temperature deviation (LTD) case using the integral isoconversional method.

comparison study between two experiments are considered: a bad measurement with large sample size and a good measurement with small sample size.

The crude oil sample used is an Alaskan crude oil with an API of 13.3. The sample mixture composition is: 4 *wt%* of crude-oil; 80 *wt%* of 60 mesh fired sand; 8 *wt%* of clay; 8 *wt%* of water. 100 *psi* back pressure is maintained within the kinetic cell.

The first measurement has 45 *g* of the sample mixture in KC1. The kinetic cell back pressure is 100 *psi*. The air injection rate is 2 *L/min*. Five RTO experiments are carried out. Temperatures within the cell chamber and the corresponding effluent gas compositions are recorded. Figures 2.7 and 2.8 show the measurement results for temperatures and O_2 consumptions respectively. Two reaction stages, the low temperature oxidation and the high temperature oxidation are observed. Figure 2.9 shows the temperature versus conversion curves. Some intersection parts are observed between curves of different heat rate. In Figure 2.10 The relationship of $1/(RT)$ and $\ln(\frac{dX}{dt})$ does not follow a linear trend in either the low temperature oxidation or the high temperature oxidation region. Based on the analysis, the activation energy fingerprint in Figure 2.11 is highly unstable and the values are not reliable. The plot

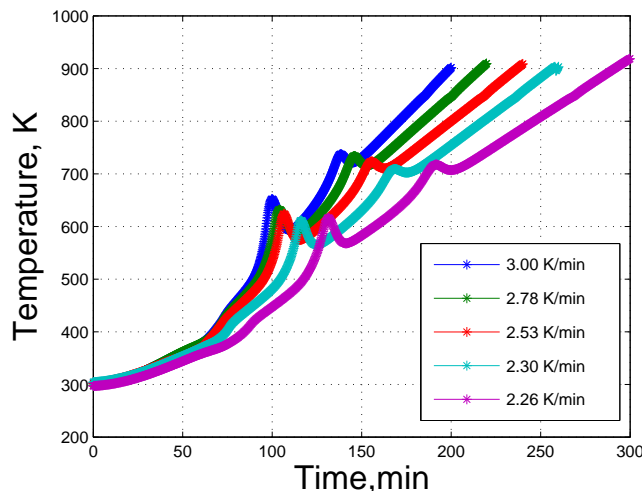


Figure 2.7: Temperature histories for the RTO of Alaskan sample mixture: 13.3 °API, 45 grams of the sample mixture are used for each RTO experiment.

does not show characteristic LTO and HTO regions.

The second measurement is conducted using a smaller size of sample mixture of 25g in the KC1. The kinetic cell back pressure is 100 *psi* and the air injection rate is 1.5 *L/min*. Temperatures within the cell chamber and the corresponding effluent gas compositions are plotted in Figure 2.12 and Figure 2.13, respectively. Figure 2.14 shows the temperature versus conversion curves. The curve of high heat rate is over those of lower heat rates and there is no intersection of the curves. In Figure 2.15, the relationship of $\ln(\frac{dX}{dt})$ and $1/(RT)$ follow a linear trend in both the low temperature oxidation and the high temperature oxidation stages. The consistency analysis reveals good measurement for this case. The activation energy fingerprint in Figure 2.16 exhibits two reaction stages and the activation energy values are reliable.

2.4 Repeatable RTO measurements

Three cases are conducted to test the repeatable character of RTO experiments for iso-conversional interpretation. Based on the model-free character of the isoconversional principle, the RTO measurements are conducted using the same sample mixture but

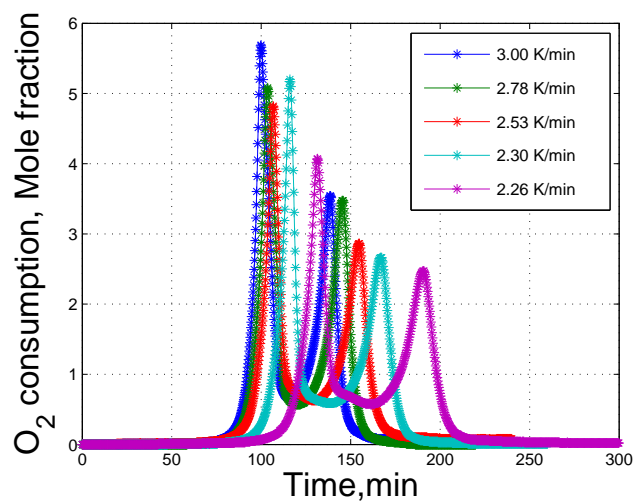


Figure 2.8: O_2 consumption histories for the RTO of Alaskan sample mixture: 13.3 °API, 45 grams of the sample mixture are used for each RTO experiment.

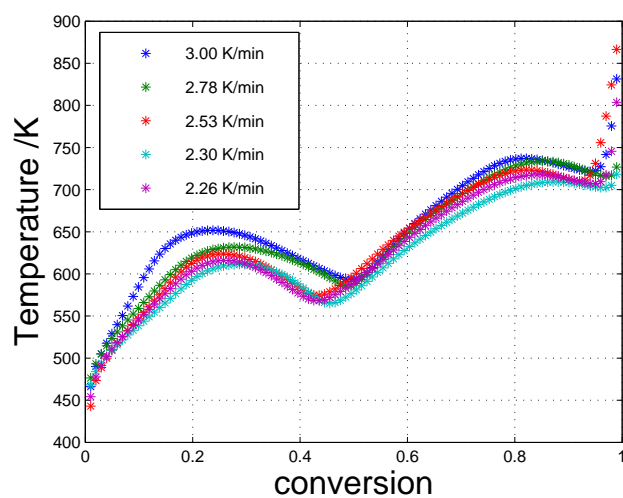


Figure 2.9: Temperature versus conversion for the RTO of Alaskan sample mixture: 13.3 °API, 45 grams of the sample mixture are used for each RTO experiment.

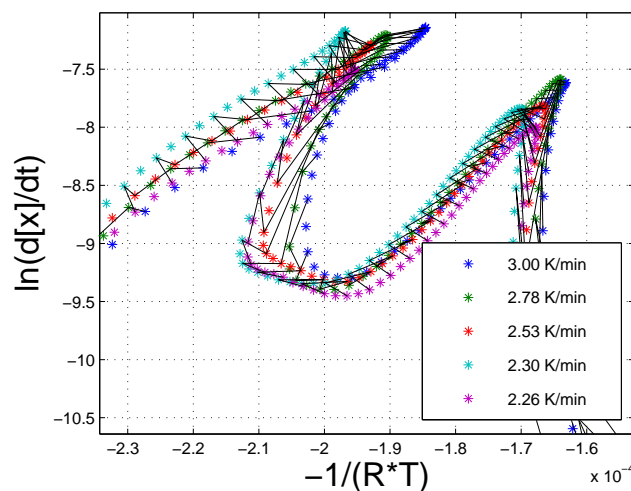


Figure 2.10: A plot of $\ln(d[X]/dt)$ versus $-1/(RT)$ for consistency check. The black solid lines connect dots of the same conversion X of different heat rates. Trends of each line are not linear for this measurement indicating inconsistent data. Alaskan sample mixture: 13.3 °API, 45 grams of the sample mixture are used for each RTO experiment.

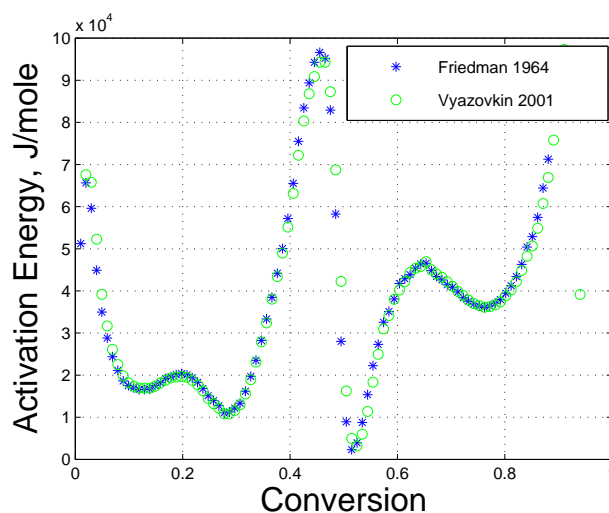


Figure 2.11: Apparent activation energy fingerprint obtained from inconsistent data for the RTO of Alaskan sample mixture: 13.3 °API, 45 grams of the sample mixture are used for each RTO experiment.

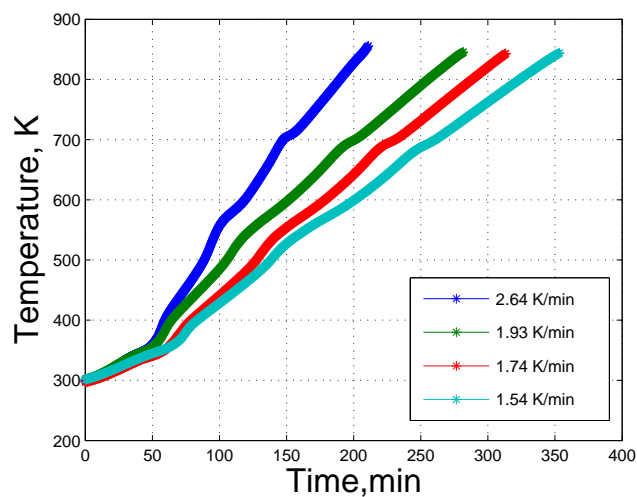


Figure 2.12: Temperature histories for the RTO of Alaskan sample mixture: 13.3 °API, 25 grams of the sample mixture are used for each RTO experiment.

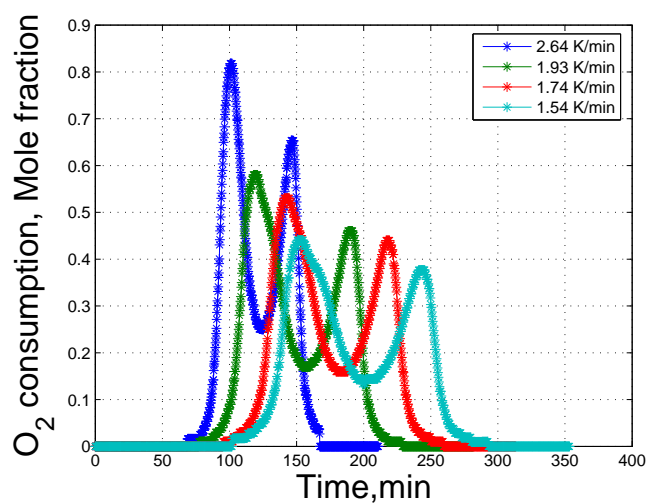


Figure 2.13: O_2 consumption histories for the RTO of Alaskan sample mixture: 13.3 °API, 25 grams of the sample mixture are used for each RTO experiment.

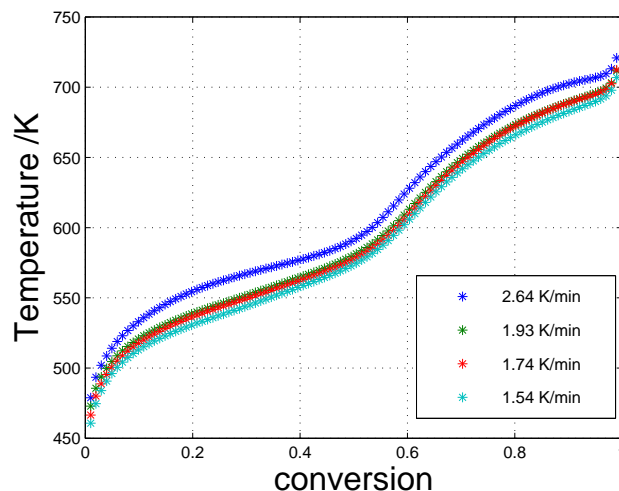


Figure 2.14: Temperature versus conversion for the RTO of Alaskan sample mixture: 13.3 °API, 25 *grams* of the sample mixture are used for each RTO experiment.

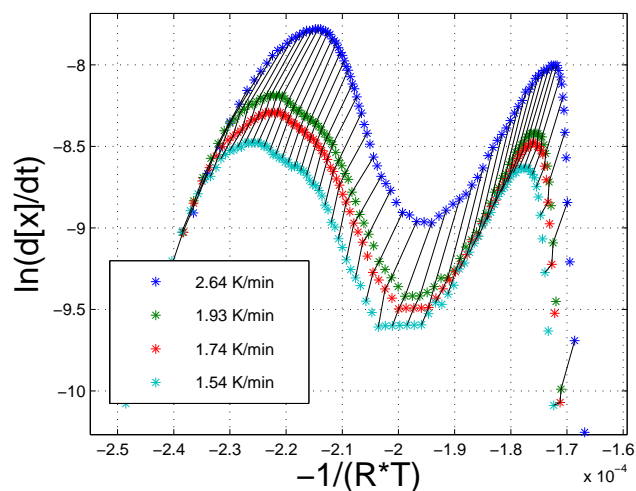


Figure 2.15: A plot of $\ln(d[X]/dt)$ versus $-1/(RT)$ for consistency check. The black solid lines connect dots of the same conversion X of different heat rates. Trends of each line are linear for this measurement. Alaskan sample mixture: 13.3 °API, 25 *grams* of the sample mixture are used for each RTO experiment.

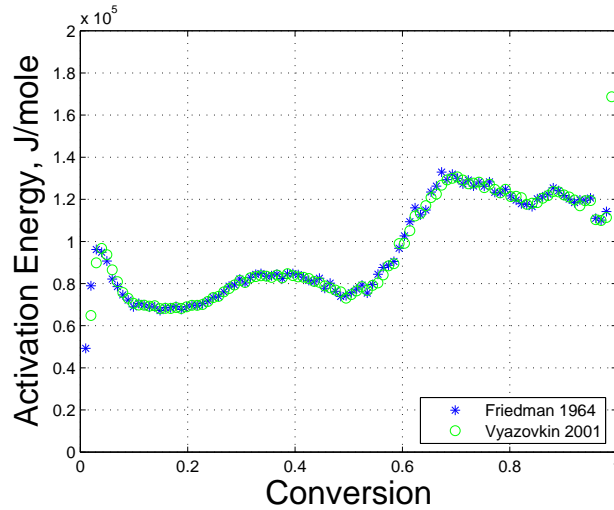


Figure 2.16: Apparent activation energy fingerprint obtained from consistent data for the RTO of Alaskan sample mixture: 13.3 °API, 25 grams of the sample mixture are used for each RTO experiment.

under different working conditions, including different kinetic cell designs, different sample mixture sizes and different air injection rates.

The sample mixture used is the Alaskan crude-oil - 2.2 wt%; 60 mesh fired sand - 88.9 wt%; clay - 0 wt% and water - 8.9 wt%. A 100 psi back-pressure is applied for all experiments. The first case uses KC1. 18 g of the sample mixture is put into the kinetic cell and 1 L/min gas injection rate is used. The second case uses KC2. 25 g of the sample mixture is used and 1.5 L/min gas injection rate is applied. The third case uses KC3. 10 g of the sample mixture is used and 1 L/min gas injection rate is applied. For each case, RTO experiments of different heat rates are conducted.

The activation energy fingerprints of the three cases are plotted in Figure 2.17. The integral isoconversional method is applied. These curves demonstrate very close values of activation energy as a function of conversion. They reveal the model-free character of the isoconversional principle and the repeatability of RTO experiments for crude-oil combustion kinetic studies.

It is well known that the clay within the matrix favors the ISC process by adding interfacial area and a catalytic affect from the heavy metal derivatives [25][111]. The

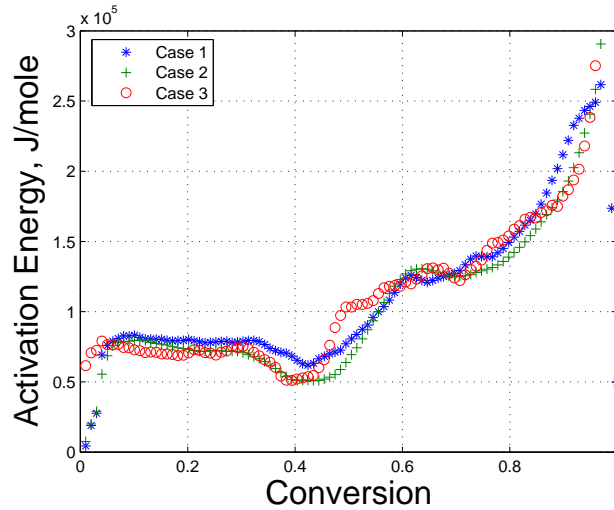


Figure 2.17: Activation energy fingerprints for three cases with different sample mass of identical composition. Case 1: KC1 is used, 18 *grams* of the mixture is used and air injection rate is 1 *L/min*; Case 2: KC2 is used, 25 *grams* of the mixture is used and air injection rate is 1.5 *L/min*; Case 3: KC3 is used, 10 *grams*, of the mixture is used and air injection rate is 1 *L/min*

clay within a sample mixture changes the reaction mechanism and reduces the apparent activation energies. This result is easily observed when we compare the activation energy fingerprints for the Alaskan crude-oil cases with and without clay in Figure 2.16 and Figure 2.17 respectively. More details on the rock surface effect and kinetic information in the activation energy fingerprint are discussed in Chapter 4.

2.5 Conclusion

The isoconversional principle is successfully applied to interpret apparent activation energy for crude-oil combustion within a continuous flow stirred tank reactor. Ramped temperature oxidation experiments are conducted in the kinetic cell platform in which temperatures as well as production gas data are recorded. A simulator is developed for describing the combustion process within the kinetic cell. The simulation with a synthetic reaction model and RTO experiments with Alaskan crude-oil mixture show how to manage successful RTO experiments: because of the exothermic reaction

mechanism of crude-oil, reducing the amount of heat generated by the reaction is necessary to keep measurements reliable and consistent. Three sets of RTO experiments of different reactor designs, different air injection rates and different sample mixture sizes support that the model-free character of the isoconversional principle and its promising feature to unlock the complicated kinetics of the ISC process.

Chapter 3

Isoconversional modeling and simulation

When performing in-situ combustion simulations, a reaction kinetic model is needed to couple with other physical models, such as fluid flow through porous media and thermodynamic behavior including phase changes. Kinetic studies of crude-oil combustion offer parameters for reaction rate modeling. According to Eq.2.4, these parameters include activation energy E , pre-exponential factor A , and reaction orders a and b for oxygen partial pressure and fuel concentration, respectively. A reliable kinetic model should capture as many critical characters of the ISC process as possible, whereas the reaction scheme should consist of as few components and reactions as necessary to reduce the cost of numerical computations.

Kinetics research of crude oil combustion in porous media is complicated by several factors. The first is the multi-component character of a crude-oil. Normally, the crude oil sample consists of hundreds of identified light and heavy hydrocarbon components that dissolve into each other. The simplest hydrocarbon component, CH_4 , needs about 37 species and 351 irreversible reactions as its comprehensive chemical mechanism to account for its oxidation performance [51]. When analysis goes to a heavy component, the detailed reaction kinetic model is impractically complex. Meanwhile analyzing the crude oil by separating components or fractions dismisses

the interaction between components. This is considered to be an important factor altering the reaction paths. Secondly, the crude oil is mixed with rock matrix. The rock mineralogy, such as carbonates, surface area, and metallic catalyst has non-negligible influence on the reaction paths, thus, the apparent behavior of the combustion. The third factor is the multiphase behavior of the crude oil. The reaction kinetic performance of a certain species may be different in different phases, such as gas phase and liquid phase [79]. When accounting for phase behavior across a wide temperature range from ambient to the peak combustion temperature such as 600 °C, the thermodynamic equilibrium changes intensively. Therefore the effect of phase behavior on the combustion is nontrivial. The last but not least is the wide range of temperatures associated with heat conduction as well as heat released from exothermic reactions. Very limited experimental tools can describe the kinetic behavior in such a complicated condition. Conventionally, isothermal experiments were carried out. This technique needs to keep temperature constant at several values that artificially narrows the temperature range. The measured data do not represent the entire combustion behavior of the crude oil in the ISC process [113]. As a result, ramped temperature oxidation (RTO) within a kinetic cell was developed [31][32]. In RTO, the experiments are conducted non-isothermally. Temperature within a kinetic cell is increased by an external heat source, from ambient to a very high termination temperature. Effluent gas data are recorded by a gas analyzer. Interpretation methods include those applied to the isothermal experiments and the isoconversional principle. It is believed that the isoconversional principle has more advantages than the conventional methods with respect to its model-free nature and robustness in conducting reliable measurement [16][17].

As discussed in Chapter 2, activation energy E of crude oil combustion within a kinetic cell is dynamically changed and the apparent values are presented against the conversion X in the isoconversional fingerprint. Other kinetic parameters, like the pre-exponential factor and reaction orders for oxygen partial pressure and fuel concentration, are still unknown. This chapter introduces an approach combining both the isoconversional principle and the conventional interpretation method to define reaction parameters for the combustion model. The approach is applied in two synthetic

cases with the same reaction scheme, but different reaction model. A three-reaction scheme is proposed for the combustion of two different crude-oil sample mixtures and the reaction parameters are interpreted by the proposed method.

3.1 Defining kinetic parameters

According to the literature review, the isoconversional principle is widely applied to interpret activation energies for solid decomposition processes [114]. Mass variation is measured as a function of time and the corresponding ramped temperatures are recorded. The conversion is defined as the accumulated mass change divided by the original mass. Theoretical analysis and experimental measurement show the isoconversional principle works well on solid component reactions [114].

When this principle is applied to study ISC reaction kinetics by a continuous flow reactor, the effluent gas rather than the mass of the fuel inside the reactor chamber is measured. Application of the principle to interpret kinetic parameters is an issue. Meanwhile, other kinetic parameters, such as pre-exponential factor and reaction orders, are still unknown. Cinar et al. described governing equations derived for the kinetic cell system and the definition of conversion in terms of oxygen consumption [14][15][16], but the connection between the conventional method and the isoconversional method is not clear. Understanding the connection between the conventional method and the isoconversional method, as well as different time scales in the process of the flow reactor system is necessary. Discussion on the connection also provides some prerequisites to run successful RTO experiments for isoconversional interpretation.

In order to find out the connection between the conventional method and the isoconversional method, two different time scales in the flow reactor system need to be introduced. One time scale is the entire reaction period. At this time scale, we record temperatures and production gas compositions at a certain frequency (usually per second). A typical RTO measurement is shown in Figure 3.1, including histories for temperatures, oxygen consumption and carbon oxides fractions in the effluent gas stream. We process these measurements by the isoconversional principle to get

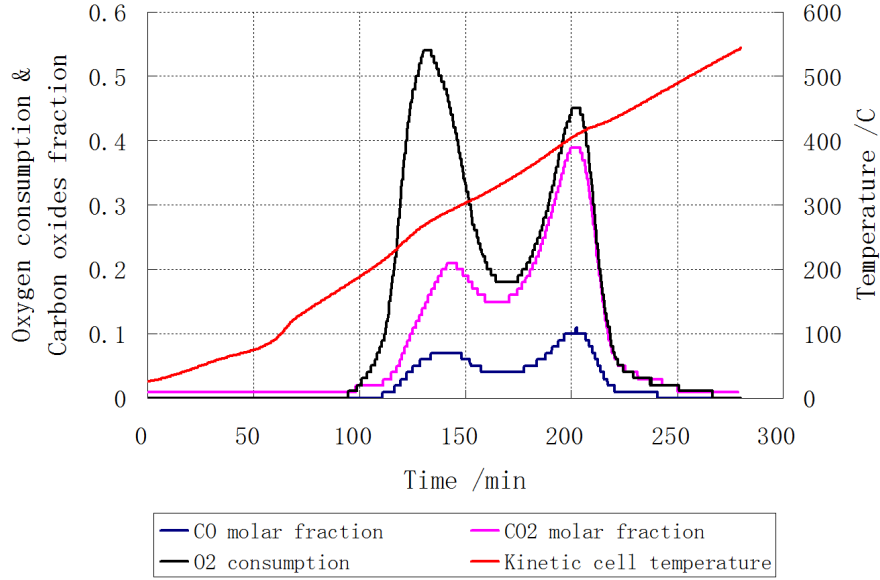


Figure 3.1: Ramped temperature oxidation measurement data

kinetic parameters.

The conversion factor in terms of oxygen consumption up to a time t is defined as

$$X = \frac{\int_0^t \Delta x_{O_2}(t) dt}{\int_0^\infty \Delta x_{O_2}(t) dt} \quad (3.1)$$

Where X is the oxygen conversion factor, and Δx_{O_2} is oxygen consumed as a function of time:

$$\Delta x_{O_2} = x_{O_2}^\circ - x'_{O_2} \quad (3.2)$$

where x'_{O_2} is the oxygen molar fraction in the outlet stream and $x_{O_2}^\circ$ is the oxygen molar fraction in the inlet stream.

The isoconversional method is a model-free process to interpret activation energy. Little manipulation of measurement data is needed for processing. So it is very convenient, and it has many advantages as compared to the conventional method of obtaining activation energy values. It is not that straightforward to obtain the formula of a reaction model in terms of oxygen conversion X . Some research describes

how to interpret the pre-exponential factor using the isoconversional principle. A reaction model of a certain reaction order is presumed. One example is polymer degradation modeling. The overall degradation rate is conventionally expressed by n th order model of sample mass [37]. In an RTO measurement where effluent gas compositions are recorded, however, the fuel mass within the kinetic cell is not measured. Furthermore, it is very difficult to describe the fuel concentration using the oxygen conversion X because of the multi-step reaction scheme and the unknown stoichiometry.

On the other hand, conventional expression of reaction rates describes a reaction model in terms of reactant concentrations as

$$-\frac{dC_f}{dt} = A^* \exp\left(-\frac{E}{RT}\right) C_{O_2}^a C_f^b \quad (3.3)$$

When a reactant is in the gas phase, such as oxygen, partial pressure of the gas is used in place of the concentration:

$$-\frac{dC_{O_2}}{dt} = A \exp\left(-\frac{E}{RT}\right) P_{O_2}^a C_f^b \quad (3.4)$$

In the RTO experiment, oxygen concentration is approximated as

$$C_{O_2} = \frac{\frac{x_{O_2} P_{total} V}{T_0}}{V} = \frac{x_{O_2} P_{total}}{T_0} \quad (3.5)$$

In terms of molar fraction of oxygen, x_{O_2} , Eq. 3.4 is written as

$$-\frac{dx_{O_2}}{dt} = (AT_0 P_{total}^{a-1}) \exp\left(-\frac{E}{RT}\right) x_{O_2}^a C_f^b \quad (3.6)$$

To apply Eq. 3.6 to interpret kinetic parameters from measured RTO data, the other time scale related to the gas volumetric flow rate is introduced. The process of the continuous flow reactor is simplified in Figure 3.2. The residence time Δt is defined in Eq. 3.7. If Δt is small enough, T is considered to be the same at the inlet and the outlet streams. This condition is achieved by a relatively high gas injection rate and increasing temperature slowly in a RTO experiment. The injection gas is

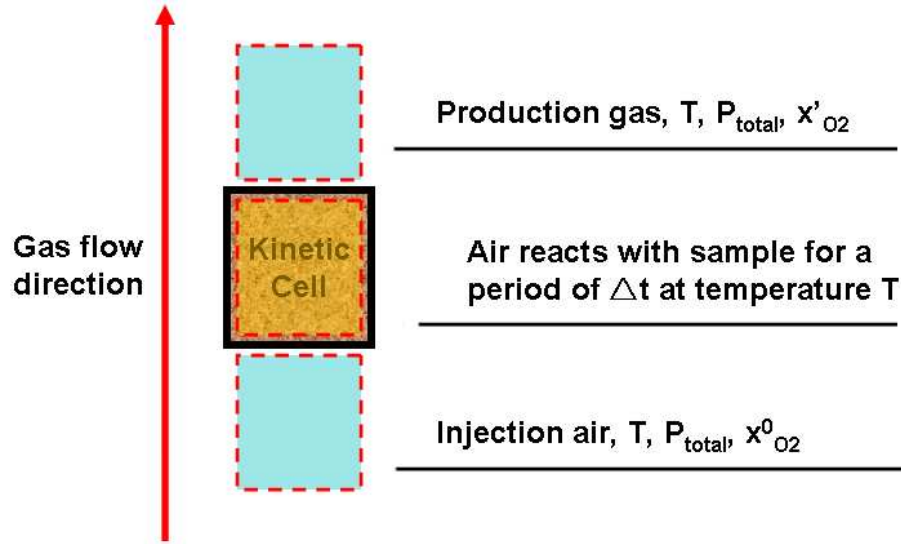


Figure 3.2: Continuous flow reaction process during RTO

preheated to the kinetic cell temperature in the inlet portion of the furnace. So Eq. 3.6 is written as

$$\Delta t = \frac{\text{Void volume inside the kinetic cell}}{\text{Volumetric flow rate}} \quad (3.7)$$

$$\frac{\Delta x_{O_2}}{\Delta t} = (AT_0 P_{total}^{a-1}) \exp\left(-\frac{E}{RT}\right) (x_{O_2}^o)^a C_f^b \quad (3.8)$$

For a normal RTO experiment, where the gas injection rate is 1.5 L/min or above and the temperature heat rate is 3 K/min or lower, the condition is fulfilled. Together with Eq. 2.5 and Eq. 3.8, we can estimate activation energy E , pre-exponential factor A , and reaction order a and b .

3.1.1 Defining activation energy

By applying the isoconversional principle that considers the reaction model to be only a function of conversion X and independent from temperature T , we obtain the activation energy E by post processing RTO measured data. Taking the logarithm on both sides of Eq. 2.5, we have

$$\ln\left(\frac{dX}{dt}\right) = \ln(Af(X)) - \frac{E}{RT} \quad (3.9)$$

By plotting $\ln(\frac{dX}{dt})$ vs. $-\frac{1}{RT}$ of RTO experiments, activation energy values as a function of the conversion factor X are interpreted. This is the differential form of the isoconversional principle. Other adjusted forms including the integral formulations are developed [112][115], but the differential form is fundamental and it provides us direct clues on handling RTO experiments correctly as discussed in Chapter 2.

3.1.2 Defining reaction orders

When the activation energy values are interpreted, the fuel reaction order is solved. Defining α as the oxygen conversion within a reaction stage, and according to the isoconversional principle, fuel conversion is proportional to oxygen conversion,

$$C_{f,X}^b = ((1 - X)C_f^\circ)^b \quad (3.10)$$

where C_f° is the initial fuel concentration. Considering Eq. 3.8 for one of the RTO measurements at two different conversions, X_1 and X_2 in a certain reaction stage

$$\frac{\Delta x_{O_2,X_1}}{\Delta t} = (AT_0 P_{total}^{a-1}) \exp\left(-\frac{E}{RT_{X_1}}\right) (x_{O_2}^\circ)^a C_{f,X_1}^b \quad (3.11)$$

$$\frac{\Delta x_{O_2,X_2}}{\Delta t} = (AT_0 P_{total}^{a-1}) \exp\left(-\frac{E}{RT_{X_2}}\right) (x_{O_2}^\circ)^a C_{f,X_2}^b \quad (3.12)$$

substituting $C_{f,\alpha 1}^b$ and $C_{f,\alpha 2}^b$ into Eq. 3.10 and combining Eq. 3.11 and Eq. 3.12 together, one can get

$$\frac{\Delta x_{O_2,X_1}}{\Delta x_{O_2,X_2}} = \exp\left(\frac{E}{RT_{X_2}} - \frac{E}{RT_{X_1}}\right) \left(\frac{1 - X_1}{1 - X_2}\right)^b \quad (3.13)$$

Solving Eq. 3.13 provides the value for fuel reaction order, b .

According to Eq. 2.5 and Eq. 3.8, if the reaction mechanism is well defined, it should be independent of partial pressure of oxygen. In the following section, RTO experiments of different injected oxygen fractions support this argument. Considering

two RTO measurements of different oxygen fraction streams, $\Delta x_{O_2,1}^\circ$ and $\Delta x_{O_2,2}^\circ$, where the superscript ' \circ ' indicates the inlet condition, Eq. 3.8 is manipulated for different RTO programs at the same oxygen conversion X :

$$\frac{\Delta x_{O_2,1}}{\Delta t} = (AT_0 P_{total}^{a-1}) \exp\left(-\frac{E}{RT_1}\right) (x_{O_2,1}^\circ)^a C_{f,1}^b \quad (3.14)$$

$$\frac{\Delta x_{O_2,2}}{\Delta t} = (AT_0 P_{total}^{a-1}) \exp\left(-\frac{E}{RT_2}\right) (x_{O_2,2}^\circ)^a C_{f,2}^b \quad (3.15)$$

At the same conversion X ,

$$C_{f,1}^b = C_{f,2}^b \quad (3.16)$$

Combining Eq. 3.14 and Eq. 3.15 together, we have

$$\frac{\Delta x_{O_2,1}}{\Delta x_{O_2,2}} = \exp\left(\frac{E}{RT_2} - \frac{E}{RT_1}\right) \left(\frac{x_{O_2,1}^\circ}{x_{O_2,2}^\circ}\right)^a \quad (3.17)$$

By solving Eq. 3.17, we find the numerical value of a .

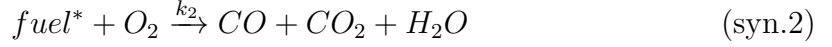
3.1.3 Defining pre-exponential factor

After activation energy and reaction orders are defined, we interpret the pre-exponential factor using Eq. 3.8. Because of the multi-step reaction scheme, the chosen conversion values should be small so that the impacts from other oxygen consumption reactions with greater activation energy are minimized.

$$A = \frac{\Delta x_{O_2,\alpha}}{T_0 P_{total}^{a-1} \exp\left(-\frac{E}{RT_\alpha}\right) ((1-\alpha) C_f^\circ)^b (x_{O_2}^\circ)^a \Delta t} \quad (3.18)$$

3.2 Kinetic interpretation for synthetic cases

Application of the proposed isoconversional interpretation method for kinetic parameters is demonstrated. Two synthetic cases of the same reaction scheme with different reaction models are used. The reaction scheme consists of two reactions:



In the reaction scheme, $fuel$ and $fuel^*$ are in the liquid phase and other species are in the gas phase. The virtual kinetic cell simulator uses reactant concentration to calculate the oxygen uptake rates (partial pressure expression and concentration expression for the rate equation are consistent). Eq. 3.18 is rewritten as

$$A = \frac{\Delta C_{O_2, \alpha}}{\exp(-\frac{E}{RT_\alpha})((1 - \alpha)C_{f, initial})^b (C_{O_2}^\circ)^a \Delta t} \quad (3.20)$$

Other input parameters used in VKC are listed below:

- Pressure: $P_{total} = 100 \text{ psi}$;
- Void volume within the kinetic cell chamber: $V = 40 \text{ cm}^3$;
- Volumetric flow rate: $\dot{V} = 2 \text{ L/min}$;
- Fuel initial concentration in the cell: $C_f^\circ = 20000 \text{ mole/m}^3$;
- Oxygen initial concentration in the gas stream: $C_{O_2}^\circ = 222.49 \text{ mole/m}^3$;
- Oxygen molar fraction in the inlet stream: 80% or 100%.

3.2.1 Synthetic case of unit reaction orders

The first synthetic case considers unit reaction orders for both fuel and oxygen. The kinetic parameters are listed in Table 3.1.

The simulation results of temperature and oxygen consumption as a function of conversion are shown in Figure 3.3 for the 80% oxygen case and Figure 3.4 for 100% oxygen case. Figure 3.5 shows the activation energy fingerprints for both cases. The 80% oxygen case and 100% oxygen case reveal similar behavior on the isoconversional fingerprint. Oxygen partial pressure does not alter the reaction paths.

Table 3.1: Arrhenius parameters used in the synthetic case of unit reaction orders

	$A, 1/(mole \cdot s)$	$E, J/mole$	Heat of reaction, $J/mole$	a	b
Reaction syn.1	1	63000	-40000	1	1
Reaction syn.2	100	120000	-60000	1	1

Calculation is done based on one of the RTO experiments in Figure 3.3 and Eq. 3.13 to define the fuel's reaction order b . From Figure 3.5(a), the activation energy for the reaction syn.1 and syn.2 are 63000 $J/mole$ and 120000 $J/mole$ respectively. From Figure 3.3(b) and 3.3(a), we pick up the conversion values of 0.1 and 0.2 for the reaction syn.1 and 0.6 and 0.7 for the reaction syn.2. The reaction syn.1 consumes about 50% of the total oxygen, and the reaction syn.2 consumes about the rest 50% of the total oxygen. So for the reaction syn.1, we can get $b = 1.0136$. We do the same calculation for the reaction syn.2, and we can get $b = 0.9976$.

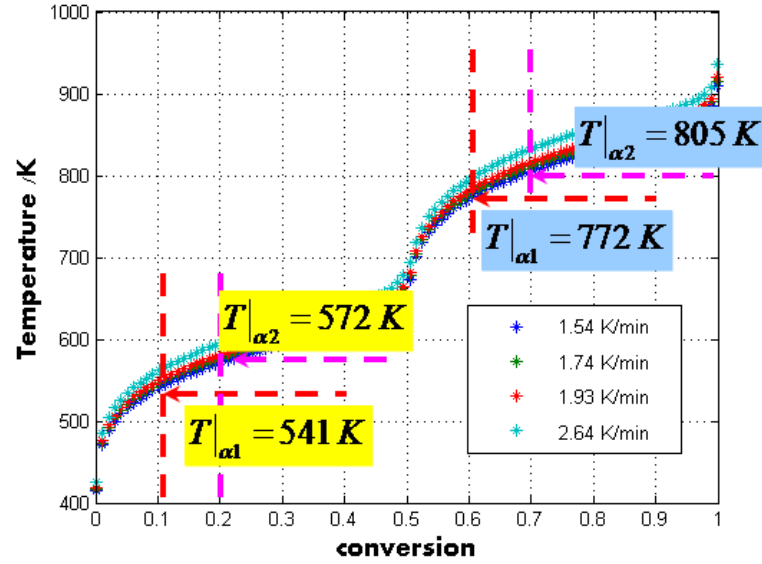
In order to get the reaction order a for oxygen, oxygen fraction within the inlet stream needs to be changed. The 100% oxygen case is considered and the calculation is based on Eq. 3.17. We pick up the conversion values of 0.2 for the reaction syn.1 and 0.7 for the reaction syn.2. So $\Delta x_{O_2,1} = 5.57$ and $\Delta x_{O_2,2} = 5.76$. The parameter a is calculated by Eq. 3.17 and is 0.9924 for the reaction syn.1. The same calculation is done for reaction syn.2, and $a = 0.9918$.

Once the reaction orders are interpreted, according to Eq. 3.20, the pre-exponential factor A is calculated. The 80% oxygen case is used to interpret A . For the reaction syn.1, The residence time is $\Delta t = 1.2 \text{ sec}$ based on Eq. 3.7. So $A = 0.9890 \text{ } 1/(mole \cdot s)$ for reaction syn.1 and $A = 101.7582 \text{ } 1/(mole \cdot s)$ for reaction syn.2.

The error analysis between the interpreted kinetic parameters and the values of pre-assumed model are compared in Table 3.2. The comparison shows acceptable matches.

3.2.2 Synthetic case of non-unit reaction orders

The second synthetic case uses non-unit reaction orders. The kinetic parameters are listed in Table 3.3. When the reaction orders are greater than one, they favor the



(a) Temperature vs. conversion

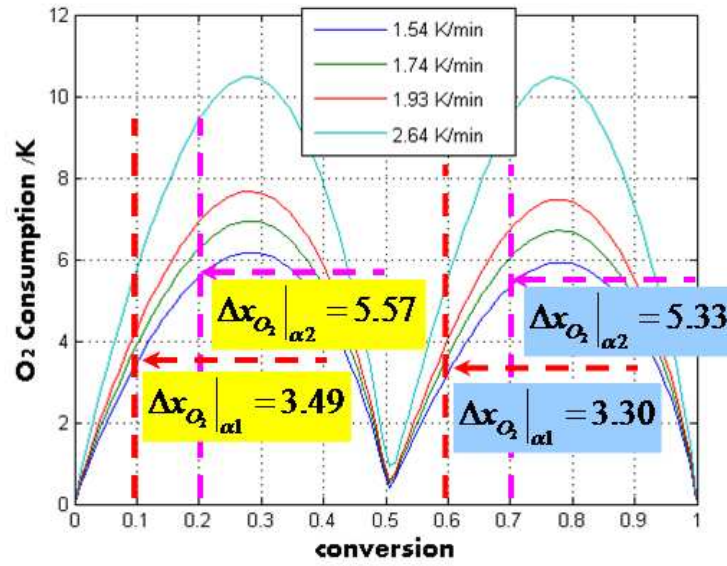
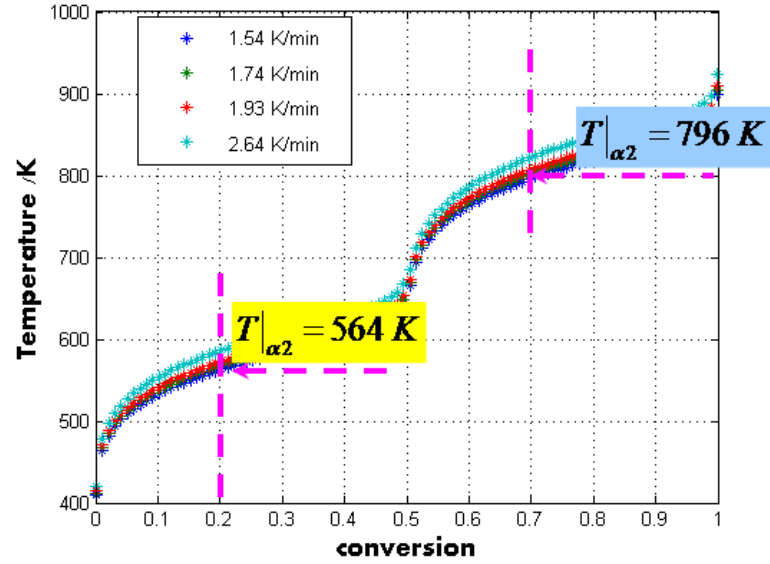
(b) O_2 consumption vs. conversion

Figure 3.3: Simulation results for the synthetic case of unit reaction orders: 80% oxygen in the injection gas stream.



(a) Temperature vs. conversion

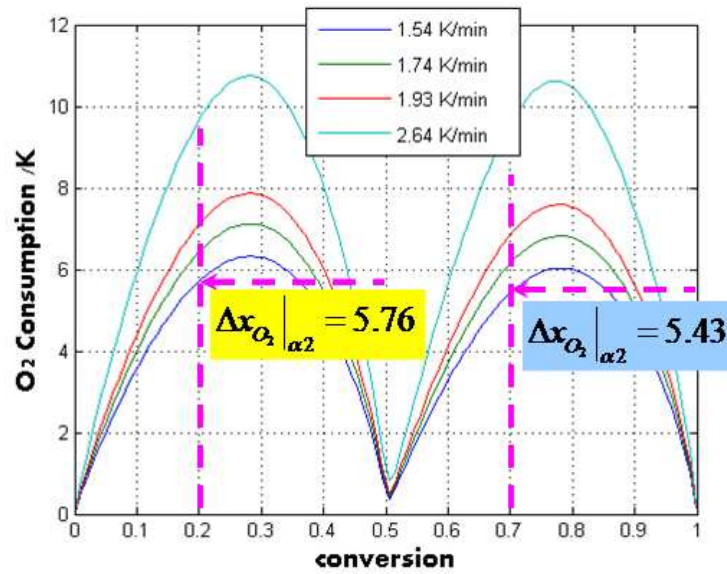
(b) O_2 consumption vs. conversion

Figure 3.4: Simulation results for the synthetic case of unit reaction orders: 100% oxygen in the injection gas stream.

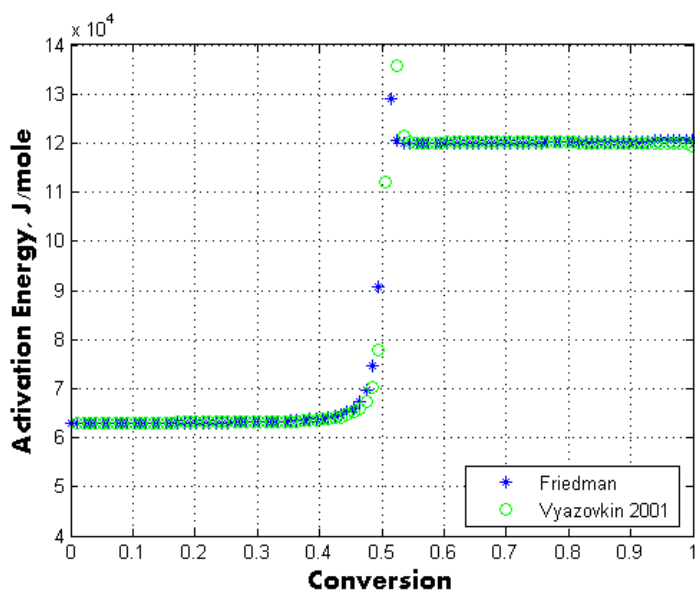
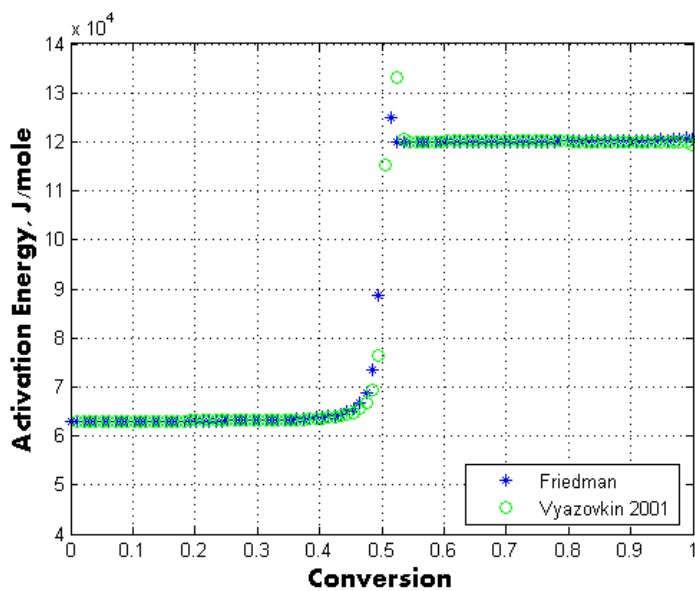
(a) Activation energy fingerprint for the $O_2 = 80\%$ case(b) Activation energy fingerprint for the $O_2 = 100\%$ case

Figure 3.5: Activation energy fingerprints for unit reaction order cases of different oxygen compositions in the injection stream: both cases reveal similar fingerprints because of the identical reaction scheme.

Table 3.2: Error analysis for the synthetic case of unit reaction orders

	A, 1/mole*s	E, J/mole	a	b
Reaction 4.2a	1	63000	1	1
Estimation value	0.9890	63000	0.9924	1.0136
Rel Error	0.011	0	0.0076	0.0136
Reaction 4.2b	100	120000	1	1
Estimation value	101.7582	120000	0.9918	0.9976
Rel Error	0.0176	0	0.0082	0.0024

Table 3.3: Arrhenius parameters used in the synthetic case of non-unit reaction orders

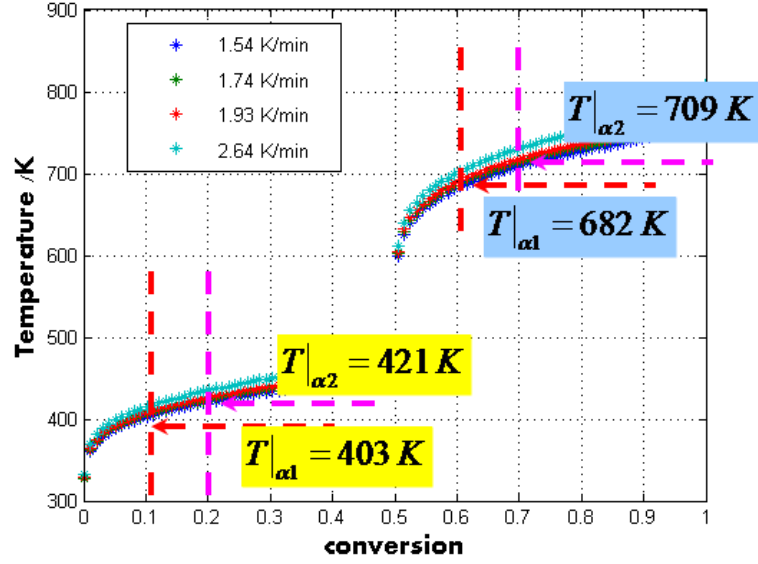
	A, 1/mole*s	E, J/mole	Heat of reaction, J/mole	a	b
Reaction 4.2a	1	63000	-20000	2	1
Reaction 4.2b	100	120000	-40000	1.5	1

reaction rates and thus the heat released, so the heat of reaction is reduced. Other parameters are the same as the synthetic case of unit reaction orders.

For the case of 80% oxygen, the simulation results are shown in Figure 3.6, and for the case of 100% oxygen, the simulation results are shown in Figure 3.7. The same calculation procedure as the synthetic case of unit reaction orders is used, and the interpreted results and error analysis are listed in Table 3.4.

Table 3.4: Error analysis for the non-unit reaction order case

	A, 1/(mole · s)	E, J/mole	a	b
Reaction 4.2a	1	63000	2	1
Estimation value	0.9839	63000	1.9864	0.9939
Rel Error	0.0161	0	0.0068	0.0061
Reaction 4.2b	100	120000	1.5	1
Estimation value	100.6609	120000	1.5148	1.0073
Rel Error	0.0066	0	0.0099	0.0073



(a) Temperature vs. conversion

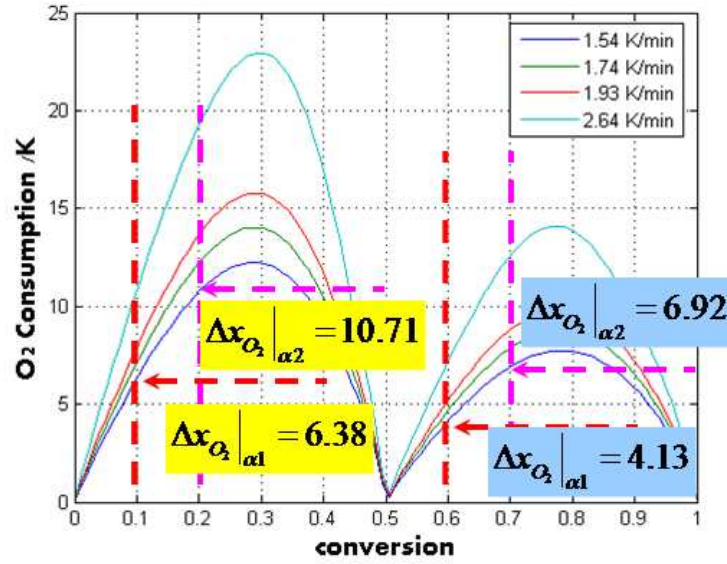
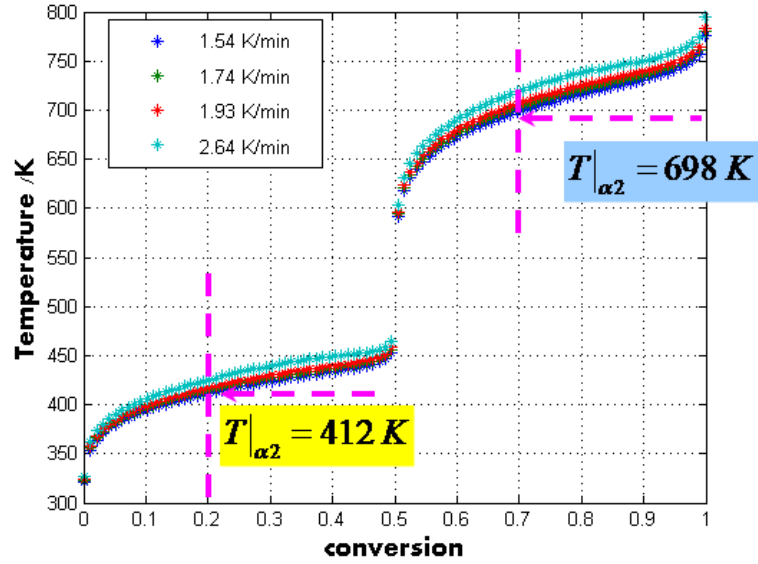
(b) O_2 consumption vs. conversion

Figure 3.6: Simulation results for the synthetic case of non-unit reaction orders: 80% oxygen in the injection gas stream.



(a) Temperature vs. conversion

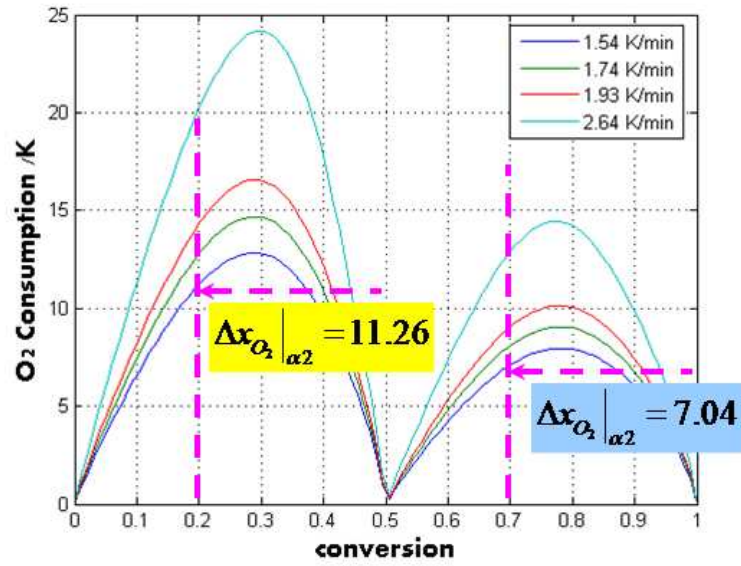
(b) O_2 consumption vs. conversion

Figure 3.7: Simulation results for the synthetic case of non-unit reaction orders: 100% oxygen in the injection gas stream.

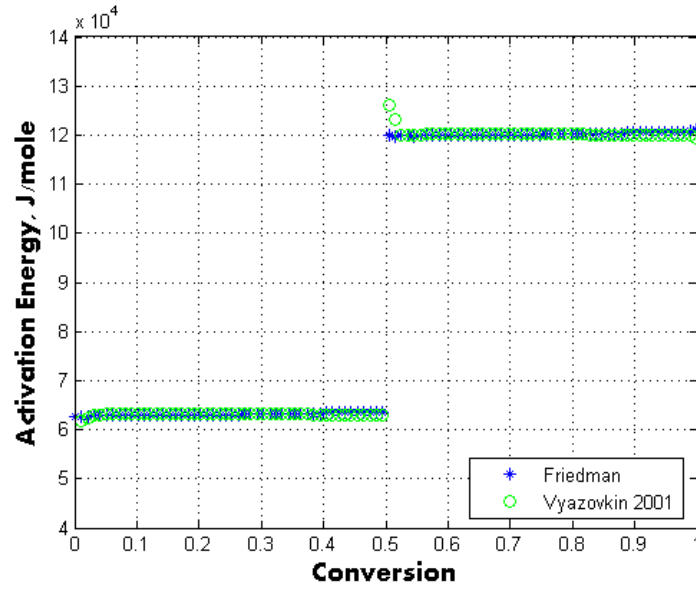
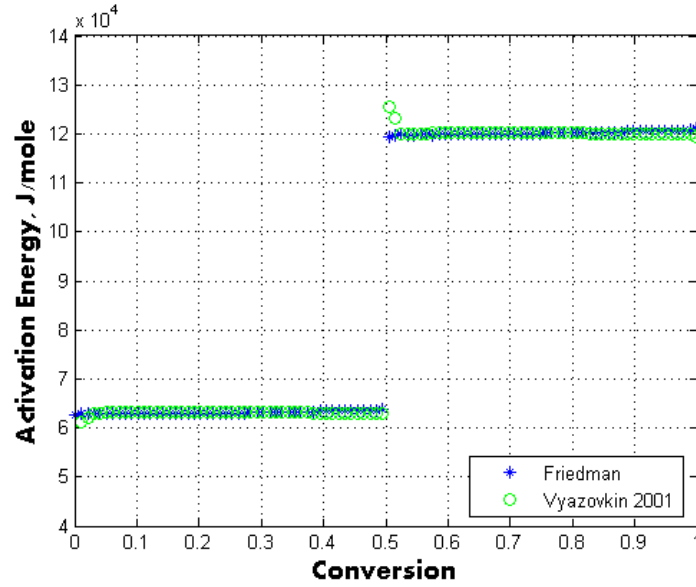
(a) Activation energy fingerprint for the $O_2 = 80\%$ case(b) Activation energy fingerprint for the $O_2 = 100\%$ case

Figure 3.8: Activation energy fingerprints for non-unit reaction order cases of different oxygen compositions in the injection stream: both cases reveal similar fingerprints because of the identical reaction scheme.

3.2.3 Discussion

The interpretation procedure applied in the synthetic cases shows acceptable results of the interpreted parameters. Reaction order for fuel is interpreted from a set of RTO experiments under the same oxygen composition injection condition, while reaction order for oxygen concentration or oxygen partial pressure is interpreted from a series of RTO experiments under different oxygen composition in the gas stream. The interpretation procedure is carried out for the real cases to build kinetic reaction models for crude-oil combustion.

3.3 Kinetic interpretation and simulation

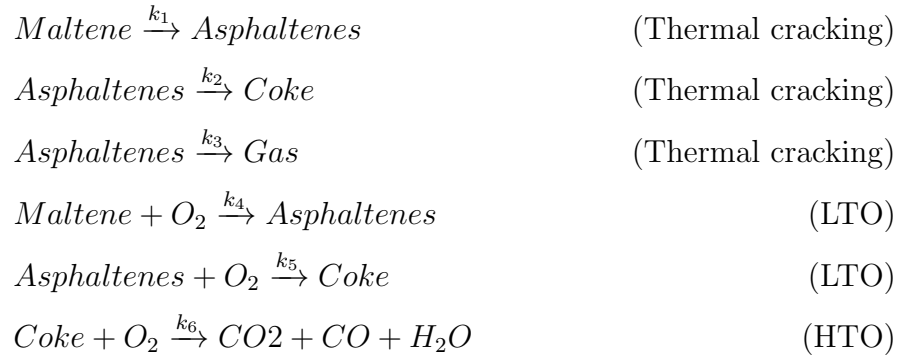
3.3.1 Gridding strategy

To verify the different reaction kinetic models proposed, simulations of the combustion process within the kinetic cell are carried out using CMG-STARs [19]. A radial gridding strategy of $4 \times 1 \times 7$ is applied to divide the RTO system into five functional zones: the crude-oil sample mixture is located in the center of the kinetic cell chamber; two sand dispersion zones are at the bottom and on the top part of the cell cavity; outside of the cell chamber is the stainless steel tube body of the kinetic cell, air zones are in between the cell body and the furnace, and the outermost zone is the electric furnace. The dimensions of each zone are the same as the real kinetic cell system in the lab. Figure 3.9 demonstrates the gridding strategy as described. The electric furnace is simulated by the outermost grid blocks with a large value of the heat capacity. Heat flux is added to the grid block and a linear temperature profile is imposed. The large value of the heat capacity reduces the influence of interior grid blocks. The injection well is located at the bottom cap of the kinetic cell, that is heated up during a RTO process so that the injected gas is preheated. Then, the gas stream travels through the sand at the inlet of the cell chamber. During this period, the gas temperature is increased even more. The preheating process in simulation is very close to the real preheating stage in an RTO experiment. While the gas keeps going upward, it contacts with the sample mixture at the center of the cell chamber

and then reactions take place with temperature increasing. The production well is located at the cap on top of the kinetic cell and the production gas is conducted through the production well to the gas analyzer.

3.3.2 Kinetic reaction scheme

There are a number of proposed reaction schemes that capture the combustion behavior during an ISC process under different conditions [6][30][17]. Based on the work of Hayashitani et al. [48] and Adegbesan et al. [2], Belgrave et al. [6] proposed a pseudo-mechanistic reaction scheme for modeling the ISC of Athabasca bitumen. The reaction scheme divides the crude oil composition into fractions of maltenes and asphaltenes. Three reactions are used for thermal cracking, two reactions for the low temperature oxidation stage and one reaction for the high temperature oxidation stage:



Reaction scheme proposed by Belgrave et al. [6].

By processing RTO experiments and observing identified reaction stages from effluent data, Dechelette et al. [23] proposed a three-reaction scheme to capture the two distinct combustion stages. They use two kinds of coke components to mimic the HTO performance:

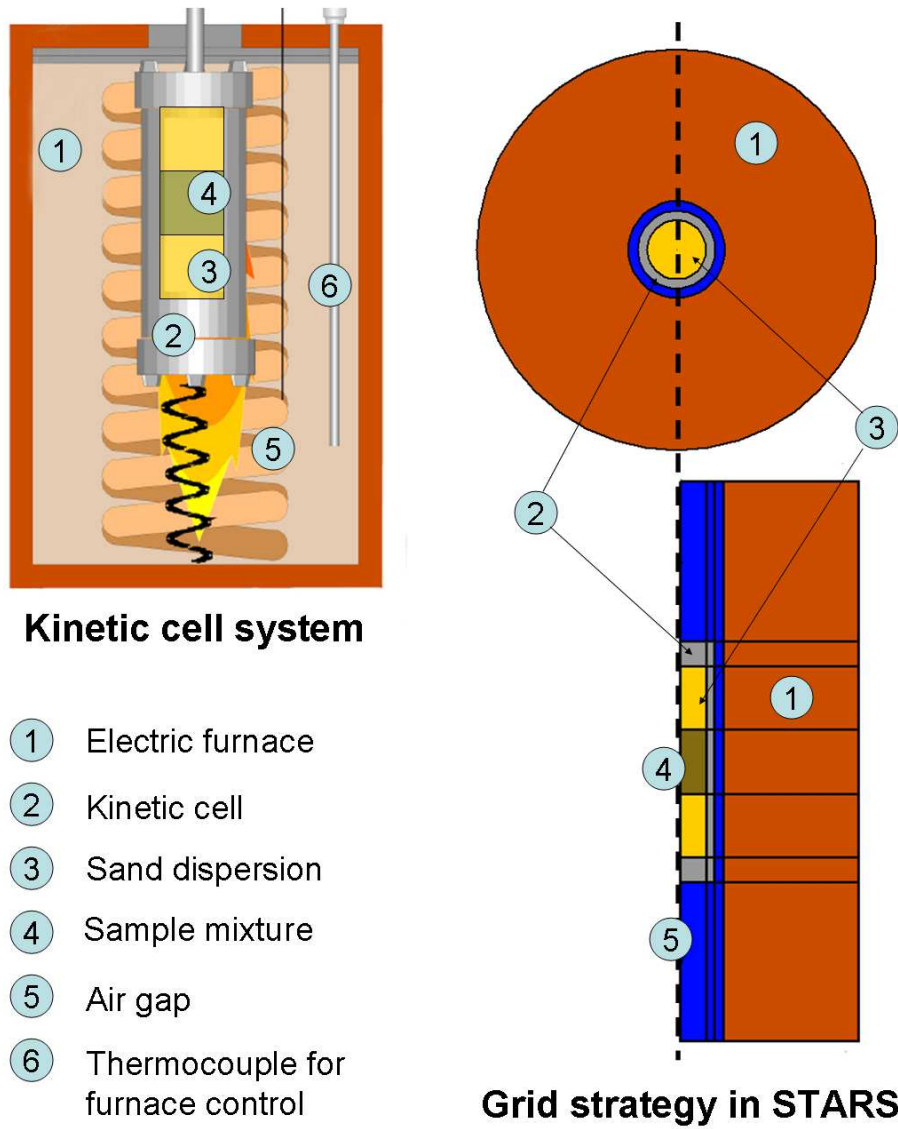
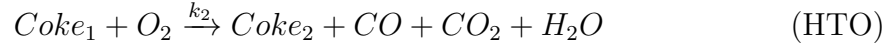
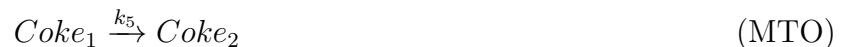
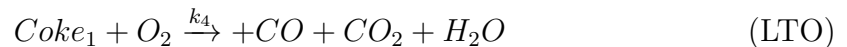


Figure 3.9: Radial gridding strategy ($4 \times 1 \times 7$ for $r \times \theta \times h$) to mimic the kinetic cell system in CMG-STARTS (the kinetic cell/furnace schematic diagram is adapted from a figure in Cinar's thesis [17]).



Reaction scheme proposed by Dechelette et al. [23].

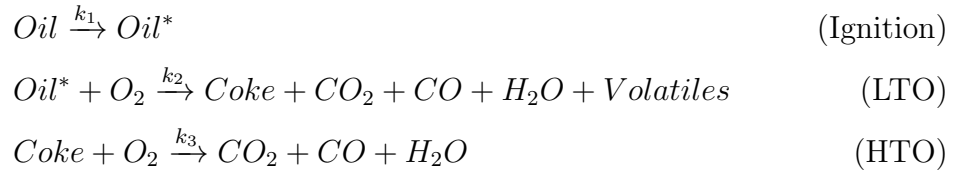
Cinar et al. [17] were the first to apply the isoconversional principle together with RTO experiments to build a reaction model for ISC. The result is based on the observation of the effluent gas data from RTO experiments and the isoconversional fingerprint of activation energies. At least two different coke formation reactions are necessary for conditions of under nitrogen and under air, and there should be two distinct coke species for LTO and HTO respectively. Stoichiometry of the proposed reaction scheme for a certain crude-oil/sand mixture is interpreted from effluent gas data. The isoconversional activation energy fingerprint is used to identify reaction stages and give initial activation energy values to each reaction. Reaction orders are all assumed to be unity, and activation energies, pre-exponential factors are tuned by an optimization strategy. After the optimization process, the kinetic cell simulations showed good matches on both temperature and effluent gas histories with RTO measurements, however, the activation energy values are different from those on the isoconversional fingerprint.



Reaction scheme proposed by Cinar et al.[17].

Based on the review of proposed reaction models in publication, a reaction model for ISC combustion, whether it is complicated or simple, needs to capture at least two identified reaction stages during the ISC process: low temperature oxidation and high temperature oxidation. A complicated reaction model captures more details, because there are more parameter variables which means more degrees of freedom. The complicated model however is expensive to couple into a reservoir simulator and has more parameters to define and most of which are difficult to interpret from experimental measurement. Therefore, tuning the parameter by an optimization routine or manually persists in ISC simulations. This tuning process at some level overshadows the physical meaning of the reaction model by a mathematical solution. On the other hand, reaction orders for reactants are normally presumed as unit. Thus, the compensation of degree of freedom comes from adding more reactions.

Therefore, proposing a simple reaction scheme and defining its parameters to the greatest extent possible from lab measurement is more preferred. Based on observation of effluent gas data together with isoconversional fingerprint, a three-reaction model is proposed for the combustion of two different crude-oil/sand mixtures, Alaskan crude oil mixed with fired sand of 60 mesh and clay and Karamay crude oil mixed with reservoir sand. The proposed reaction Scheme 3.24 describes the three major reaction stages: ignition, LTO and HTO. The ignition reaction does not change the oil property, it plays like a threshold to retard reactions happening at low temperature.



Reaction scheme 3.24

RTO experiments are carried out to define the stoichiometry of the reaction scheme and interpret kinetic parameters for the rate law model. As described previously, at least two RTO experiments at different heat rates are needed to interpret the

reaction order of fuel, and two RTO experiments of different oxygen composition in the injection stream are needed to interpret the reaction order of oxygen partial pressure. For each crude oil mixture of Alaska crude oil or Karamay crude oil, four sets of RTO experiments under four different oxygen composition injection are carried out. This is also used to check that the reaction paths are consistent under different oxygen composition.

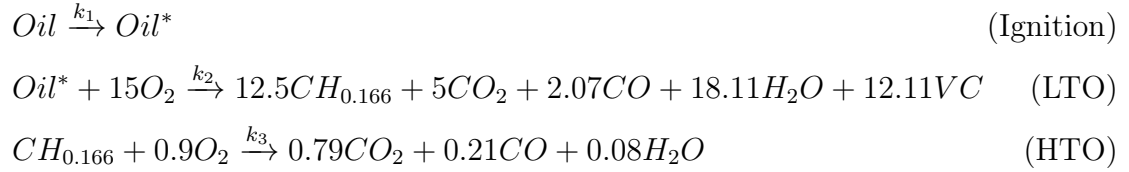
3.3.3 Alaskan oil sample

The Alaskan crude-oil (13.3 °API) sample mixture of 25 grams is used in each of the RTO experiments. The mixture composition is 2.04 wt% crude-oil, 8.16 wt% water, 81.63 wt% fired sand of 60 mesh and 8.16 wt% clay. Based on the crude-oil fraction of the mixture, 0.51 grams of crude-oil are initially inside the kinetic cell. The air injection rate is 1.5 L/min at the standard condition (25 °C and 1.01325×10^5 Pa). The RTO experiment with the heat rate of 1.85 K/min is selected for stoichiometry calculation (Figure 3.10).

The first step is defining the stoichiometry for the HTO reaction in Scheme 3.24. From Figure 3.10, CO_2/CO is 3.8, O_2/CO_2 is 1.18. Using mass balance, H_2O/CO_2 is 0.105 and H/C is 0.166. With this information, the chemical formula for coke is $CH_{0.166}$, and the stoichiometry for the HTO reaction is calculated by the balance of elements.

The entire reaction period of the RTO experiment is 18600 seconds. Processing the integral of the production gas of both CO and CO_2 over the reaction period, an amount of 1.66×10^{-2} mole of carbon C is captured by the gas analyzer in the form of carbon oxides. Considering that oxygen consumption contributes to the production of carbon oxides and water, the apparent hydrogen content within the crude-oil is calculated by subtracting oxygen in carbon oxides, and it is 2.99×10^{-2} mole. Thus, a total mass of carbon and hydrogen from crude-oil that is involved in reactions recorded by gas analyzer is 0.23 gram. The mass difference between the initial crude-oil and total mass of carbon and hydrogen recorded by the gas analyzer is caused by volatile components of the crude oil or other produced hydrocarbon gas that can't

be recognized by the gas analyzer. Both of the volatile components are hydrocarbon gases are grouped into VC in the reaction scheme. Based on mass balance, 44.86% of the original crude oil reacts with oxygen and generates coke, carbon oxides and water, and the other 55.14% is grouped into VC . From Figure 3.10, in the LTO stage, the ratio of CO_2 and CO is 2.42, and O_2/CO_2 is around 3. The crude oil molecular weight is estimated by adjusting its value to match the peak oxygen consumption of either LTO or HTO, and it is 615 $g/mole$. The molar ratio of O_2 and the coke is estimated by the peak oxygen consumption ratio of LTO and HTO. H_2O can not be estimated from the measurement, so it is used to balance the mass of products for the LTO reaction. The proposed reaction scheme for Alaska crude-oil mixture is:



Reaction scheme 3.25

After defining the stoichiometry, kinetic parameters for each of the reactions are interpreted. Four sets of RTO experiments using different oxygen composition in the injection gas are carried out. The four activation energy fingerprints are plotted in Figure 3.11. The 35% oxygen case does not reveal a consistent fingerprint as those with oxygen compositions of 16% to 21%. So this case is not taken into consideration for parameter interpretation. The ignition reaction takes place at the very beginning. From Figure 3.11, the activation energy value for the ignition reaction is about 1.0×10^5 $J/mole$. The pre-exponential factor can be estimated from the starting point of oxygen consumption and A is 1.0×10^{10} $1/(mole \cdot min)$. For the LTO reaction, the activation energy is about 8.5×10^4 $J/mole$. Two conversion X values, 0.2 and 0.22, are chosen to process the calculation for the fuel reaction order. The RTO experiments used are the one with air injection. The LTO reaction begins at about $X = 0$ and ends at around $X = 0.6$. Based on Eq. 3.13, the LTO reaction order for fuel is $b = 1.83$. Calculating the oxygen partial pressure reaction order, the

conversion value of 0.2 is used for RTO experiments of different oxygen composition in the injection gas. Based on Eq. 3.17, the reaction order for oxygen is $a = 0.9$. The residence time is calculated under the 100 psi condition and it is 0.056 min. The initial fuel concentration is about $6.87 \times 10^{-5} \text{ mole/cm}^3$. Based on Eq. 3.18, A is about $3.69 \times 10^{15} \text{ 1/(mole} \cdot \text{min)}$. The same interpretation for HTO reaction parameters is conducted. The HTO activation energy is interpreted from Figure 3.11 and it is around $1.3 \times 10^5 \text{ J/mole}$. Two conversion X values, 0.7 and 0.75, are chosen to process the calculation for the fuel reaction order and $b = 1.45$. the conversion value of 0.7 is used to interpret the HTO oxygen reaction order and $a = 1.0$. According to the molar ratio of coke and fuel, the beginning of HTO has a fuel concentration about 12.5 times of original oil. With this information and using Eq. 3.18, A is interpreted with a value of $9.95 \times 10^{13} \text{ 1/(mole} \cdot \text{min)}$. STARS simulation uses the lab unit system, so does the kinetic parameter interpretation.

The simulation result based on the kinetic interpretation is shown in Figure 3.12. The LTO takes place earlier while the HTO happens a little later. Adjustment of parameter values is carried out for pre-exponential factors of LTO and HTO only. Figure 3.13 shows the simulation results after adjusting the pre-exponential factors manually. The simulation represents matches with the effluent gas data. The adjusted values as well as the initial values of A are listed in Table 3.5. By comparison, the initial guess of A by Eq. 3.18 gives pretty good initial values for the reaction model. The parameters of the reaction model for combustion of the Alaska crude-oil mixture are listed in Table 3.6. The simulation also shows very good match of the temperature history in Figure 3.14. When comparing the isoconversional fingerprints interpreted from RTO experiments and simulation in Figure 3.15, the simulated fingerprint has a similar behavior as that of the RTO experiments.

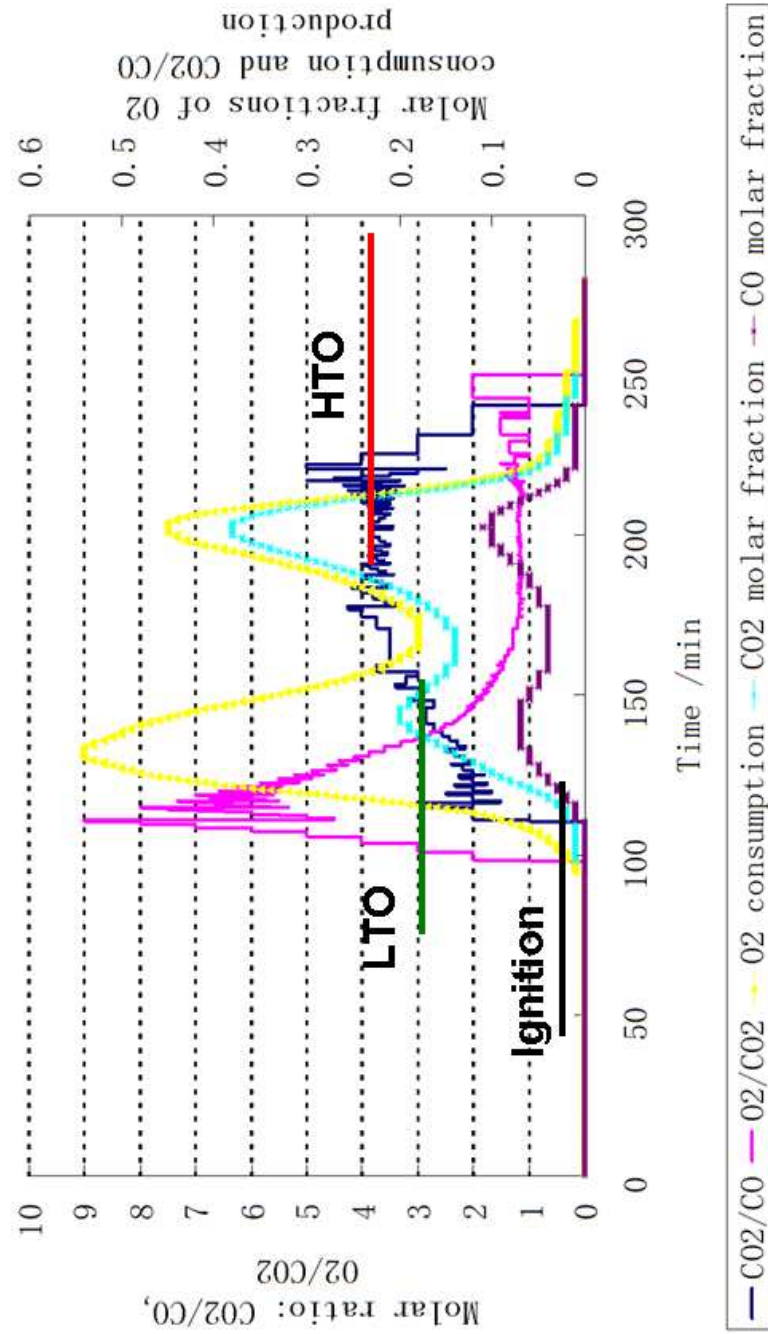


Figure 3.10: RTO measured effluent data to identify reaction stages, CO_2/CO and O_2/CO .

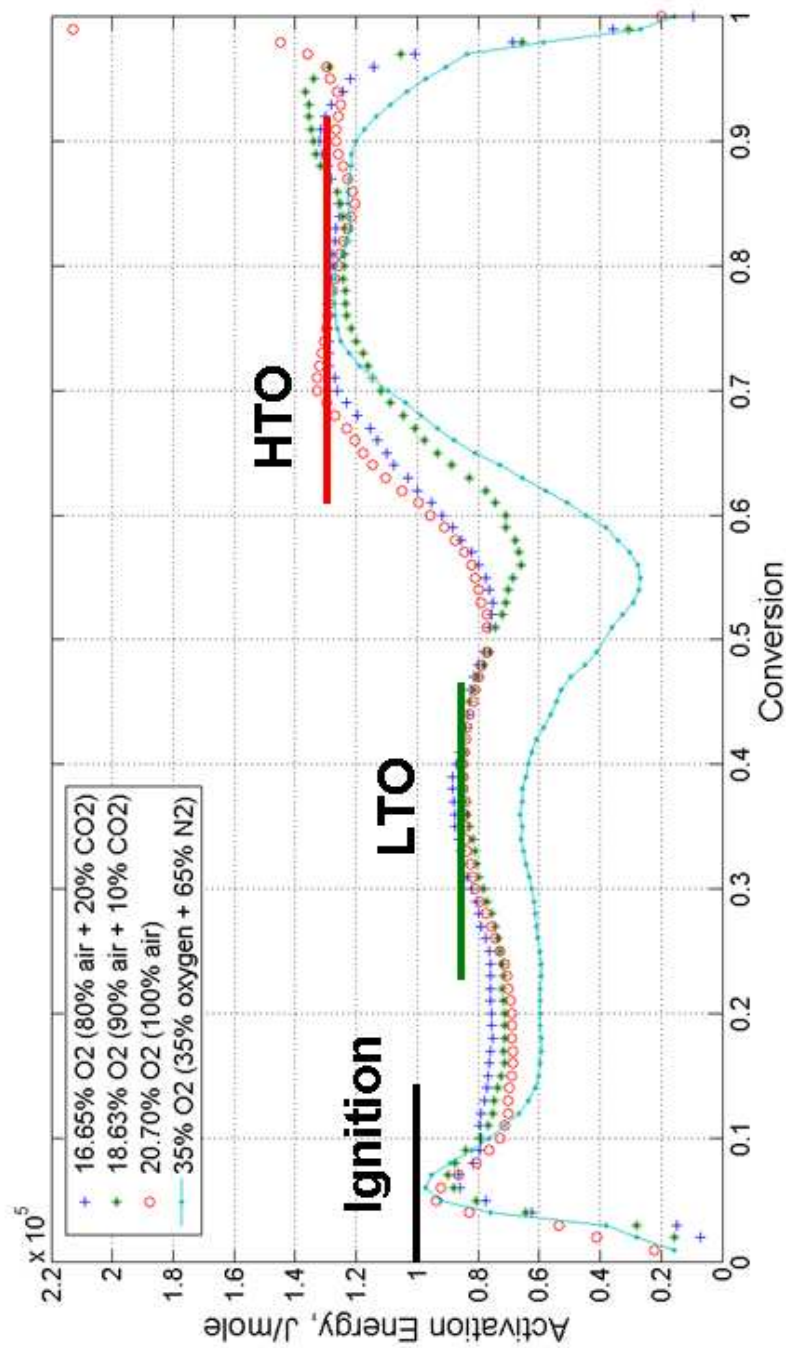


Figure 3.11: Isoconversional fingerprints for the four set of RTO experiments using different oxygen compositions in injection gas stream. The 35% oxygen case does not show consistent behavior as the other three cases. It is not used for the oxygen reaction order interpretation.

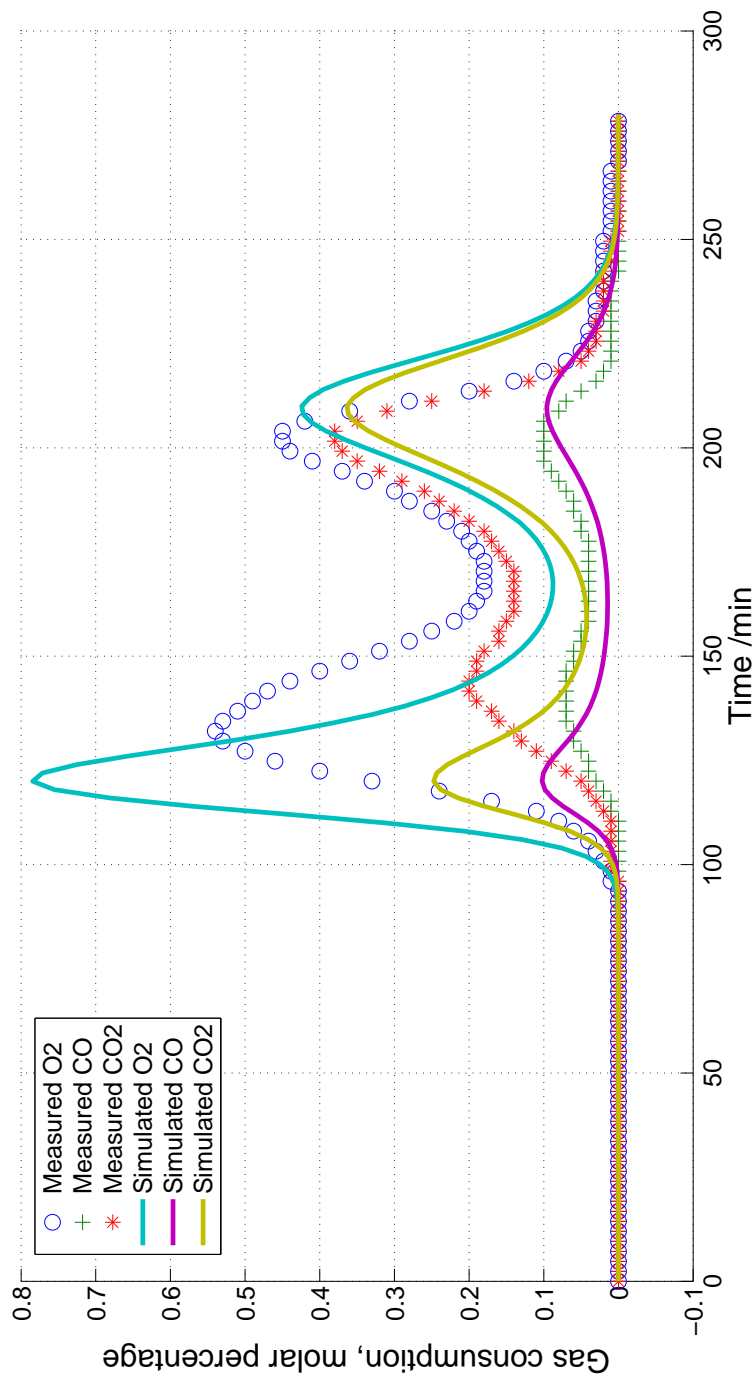


Figure 3.12: VKC simulation results based on the initial interpretation for values of activation energy, reaction orders, and pre-exponential factors A .

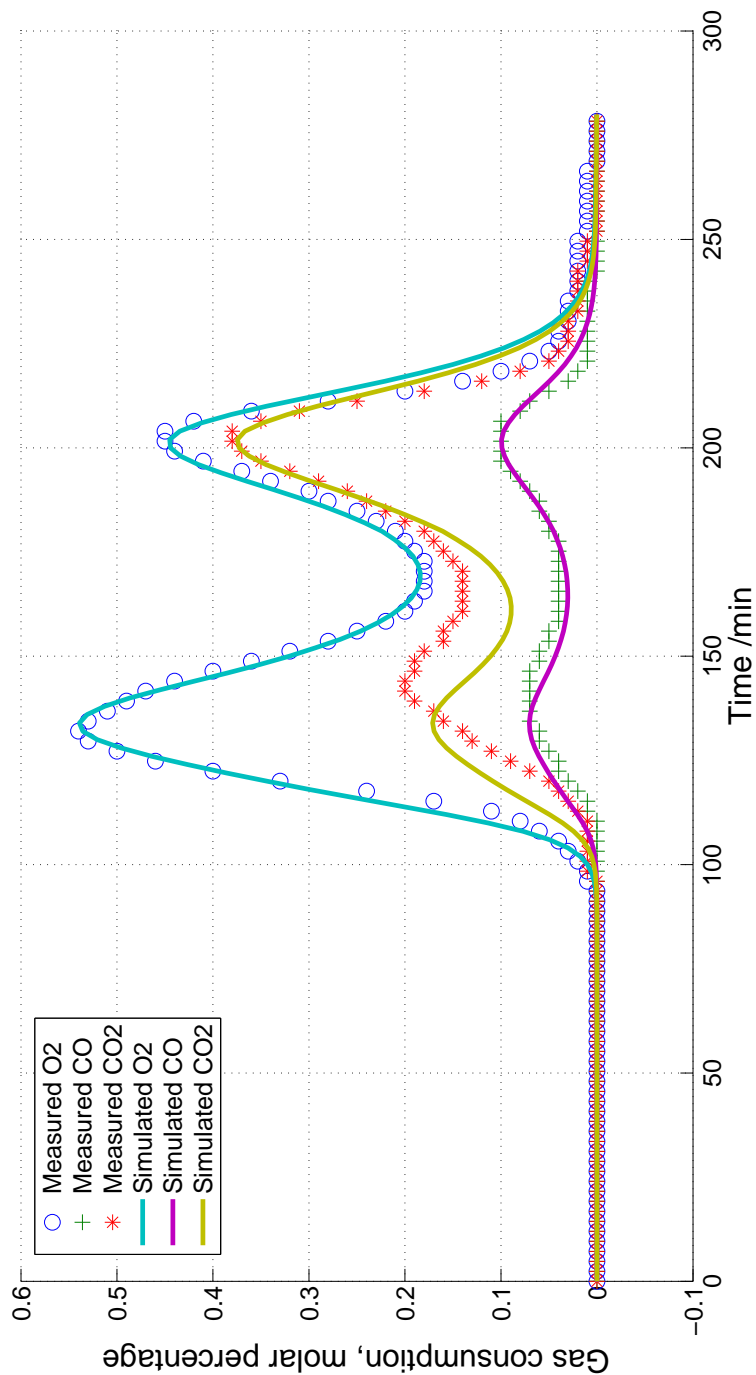


Figure 3.13: VKC simulation results based on the adjusted pre-exponential factors *A*. Interpreted values of activation energies, reaction orders, and stoichiometry are kept the same as those in the initial interpretation simulation case. The heat rate is 1.85 K/min .

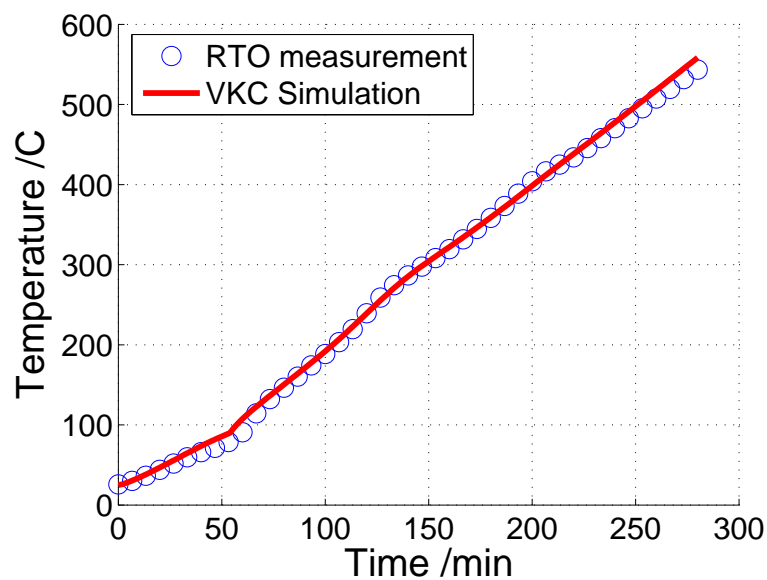


Figure 3.14: Temperature history comparison between the VKC simulation result and RTO measurement. The heat rate is 1.85 K/min

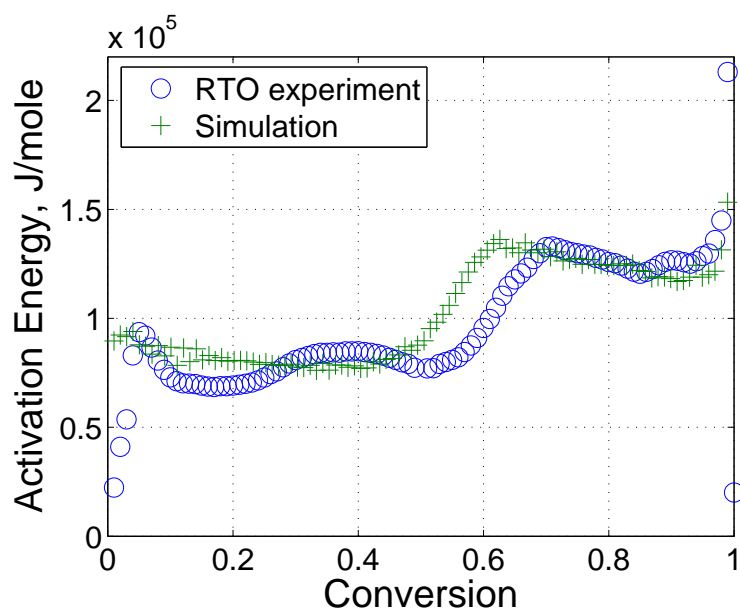


Figure 3.15: Isoconversional fingerprint comparison between the VKC simulation result and RTO measurement.

Table 3.5: Comparison between initial and adjusted values of pre-exponential factor for the Alaska crude-oil combustion modeling.

	Initially estimated, $1/(mole \cdot min)$	Adjusted, $1/(mole \cdot min)$
LTO	3.69×10^{15}	1.5×10^{15}
HTO	9.95×10^{13}	1.6×10^{14}

Table 3.6: Kinetic parameters for the proposed model of the Alaska crude-oil combustion.

Reaction	$A, 1/(mole \cdot min)$	$Ea, J/mole$	$\Delta H, J/mole$	a	b
Ignition	1.0×10^{10}	1.0×10^5	3.6×10^6	—	1
LTO	1.5×10^{15}	8.5×10^4	1.86×10^7	0.9	1.83
HTO	1.6×10^{14}	1.3×10^5	1.0×10^6	1.0	1.45

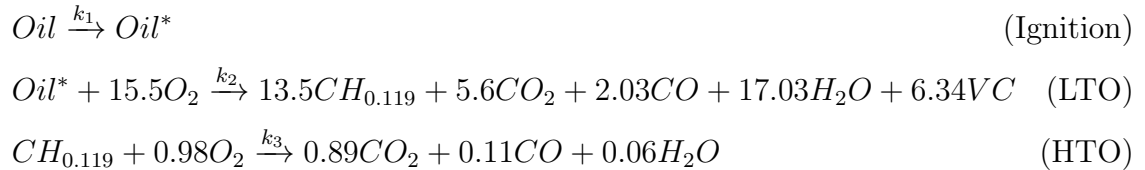
3.3.4 Karamay oil sample

The same modeling procedure is conducted for the Karamay crude-oil (11.8 °API) combustion. The crude-oil /reservoir-sand mixture of 15 gram is used for each of the RTO experiments. The composition is of 2.04 wt% crude oil, 8.16 wt% water, and 89.8 wt% sand matrix. 0.31 gram of crude oil is initially within the kinetic cell. The gas injection rate is set to be 1.5 L/min at the standard condition (25 °C and 1.01325×10^5 Pa). The RTO effluent data shown in Figure 3.16 with the heat rate of 1.85 K/min is used for the stoichiometry calculation.

The first step is defining the stoichiometry for the HTO reaction in Scheme 3.24. From Figure 3.16, CO_2/CO is 8.1, O_2/CO_2 is 1.1. Using mass balance, H_2O/CO_2 is 0.067 and H/C is 0.119. With these information, the chemical formula for coke is $CH_{0.119}$, and the stoichiometry for the HTO reaction is calculated by the balance of elements.

The entire reaction period of the RTO experiment is 18600 seconds. Processing the integral of the production gas of both CO and CO_2 over the reaction period, an amount of 1.32×10^{-2} mole of carbon C is captured by the gas analyzer in the form of carbon oxides. Considering the oxygen consumption contributes to the production

of carbon oxides and water, the apparent hydrogen content within the crude-oil is calculated by subtracting oxygen in carbon oxides, and it is 2.81×10^{-2} mole. Thus, a total mass of carbon and hydrogen from crude-oil that is involved in reactions recorded by the gas analyzer is 0.19 gram. The mass difference between the initial crude-oil and total mass of carbon and hydrogen recorded by the gas analyzer is caused by volatile components of the crude oil or other produced hydrocarbon gas that can not be recognized by the gas analyzer. Based on mass balance, 60.95% of the original crude oil reacts with oxygen and generates coke, carbon oxides and water, and the other 39.05% is grouped into *VC*. From Figure 3.10, in the LTO stage, the ratio of CO_2 and CO is 2.8, and O_2/CO_2 is around 3.4. The crude oil molecular weight is estimated by adjusting its value to match the peak oxygen consumption of either LTO or HTO, and it is 455 g/mole. The molar ratio of O_2 and the coke is estimated by the peak oxygen consumption ratio of LTO and HTO. H_2O can not be estimated from the measurement, so it is used to balance the mass of products for the LTO reaction. The proposed reaction scheme for Karamay crude-oil mixture is:



Reaction scheme 3.26

After defining the stoichiometry, kinetic parameters for each of the reactions are interpreted. Three sets of RTO experiments using different oxygen composition in the gas injection are carried out. The three activation energy fingerprints are plotted in Figure 3.17. The 35% oxygen case does not reveal consistent fingerprint as those with oxygen compositions of 16.6% and 20.7%. So the 35% oxygen case is not taken into consideration for parameter interpretation. The ignition reaction take places at the very beginning. From Figure 3.11, the activation value for the ignition reaction is about 1.13×10^5 J/mole. The pre-exponential factor can be estimated from the starting point of oxygen consumption and A is 3.7×10^{10} 1/(mole · min). For the

Table 3.7: Kinetic parameters for proposed model of the Karamay crude-oil combustion

Reaction	$A, 1/(mole \cdot min)$	$Ea, J/mole$	$\Delta H, J/mole$	a	b
Ignition	3.7×10^{10}	1.13×10^5	2.6×10^6	–	1
LTO	1.0×10^{15}	7.5×10^4	1.96×10^7	1.3	0.92
HTO	4.2×10^{12}	1.0×10^5	1.3×10^6	0.9	1.41

LTO reaction, the activation energy is about $7.5 \times 10^4 J/mole$. Two conversion X values, 0.2 and 0.25, are chosen to process the calculation for the fuel reaction order. The RTO experiments used are the ones with air injection. The LTO reaction begins at about $X = 0.1$ and ends at around $X = 0.6$. Based on Eq. 3.13, the LTO reaction order for fuel is $b = 0.92$. Calculating the oxygen partial pressure reaction order, the conversion value of 0.2 is used for RTO experiments of different oxygen composition in the injection gas. Based on Eq. 3.17, the reaction order for oxygen is $a = 1.3$. The same interpretation for HTO reaction parameters is conducted. The HTO activation energy is interpreted from Figure 3.11 and it is around $1.0 \times 10^5 J/mole$. Two conversion X values, 0.7 and 0.75, are chosen to process the calculation for the fuel reaction order and $b = 1.41$. the conversion value of 0.7 is used to interpret the HTO oxygen reaction order and $a = 0.9$. After adjusting pre-exponential factors based on the initial guess by Eq. 3.18, the kinetic parameters for the Karamay crude-oil combustion are listed in Table 3.7.

The simulation result based on the kinetic model listed in Table 3.7 is shown in Figure 3.18. The simulation represents very good matches with the effluent gas data. The simulations also show very good match of the temperature history in Figure 3.19. When comparing the isoconversional fingerprints interpreted from RTO experiments and simulation in Figure 3.20, the simulated fingerprint has a very similar behavior as the RTO experiments.

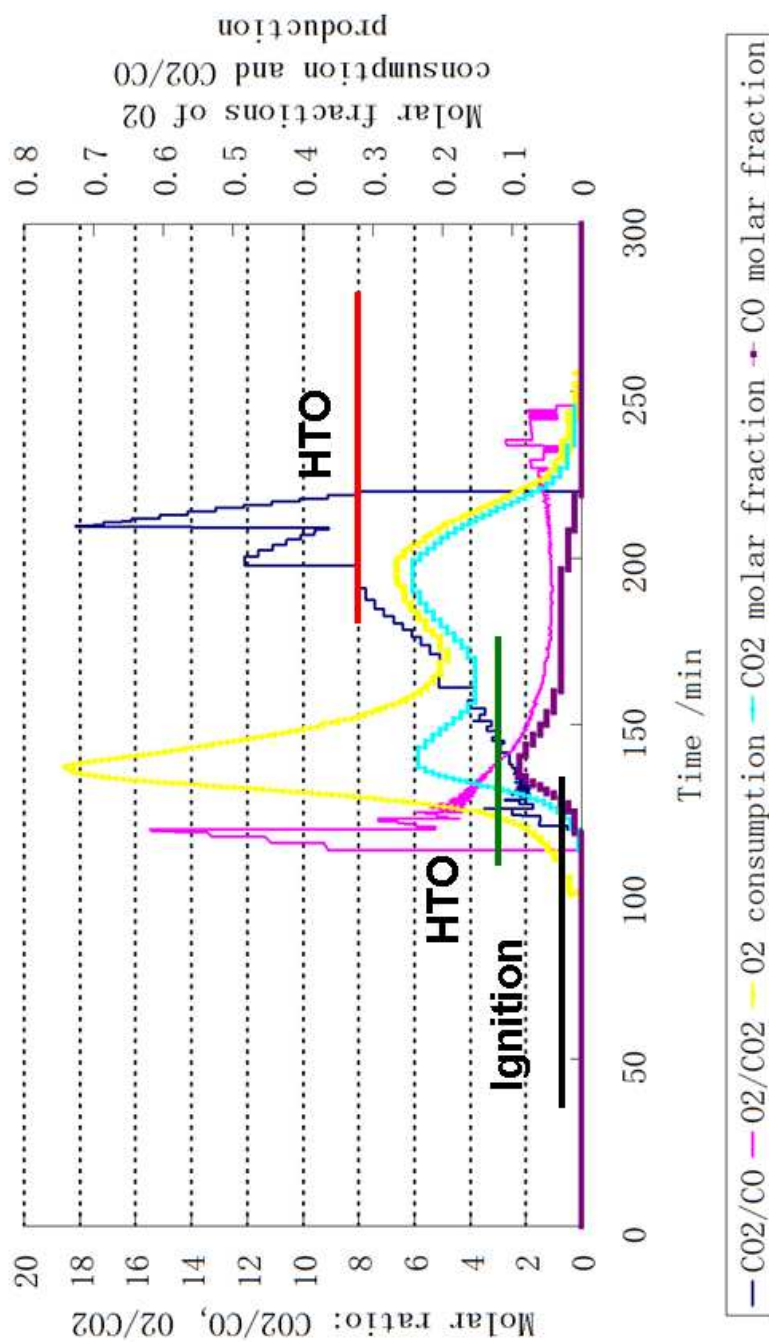


Figure 3.16: RTD measured effluent data to identify reaction stages, CO_2/CO and O_2/CO .

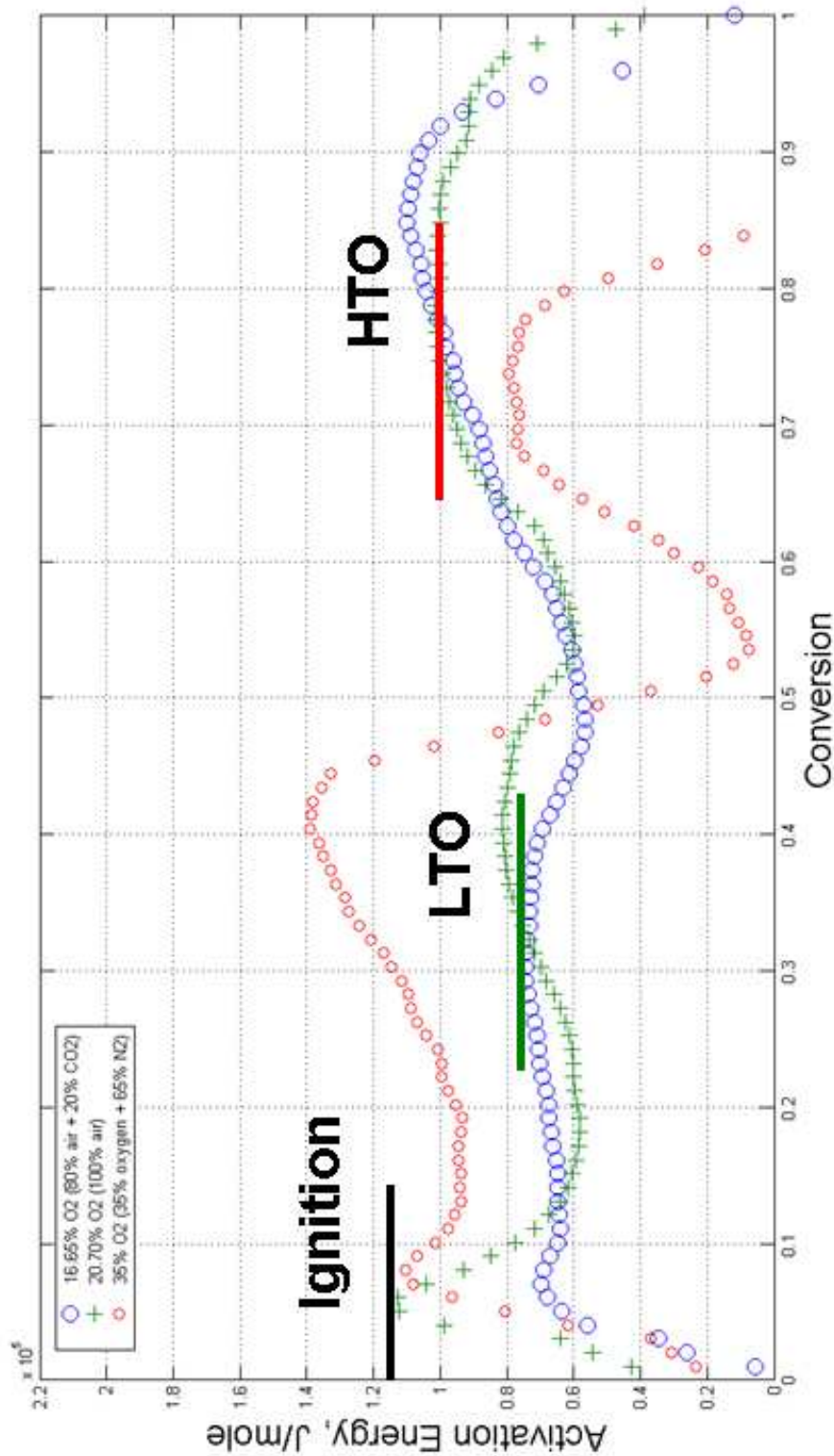


Figure 3.17: Isoconversional fingerprints for the three set of RTO experiments using different oxygen compositions in the injection gas stream. The 35% oxygen case does not show consistent behavior as the other three cases. It is not used for the oxygen reaction order interpretation.

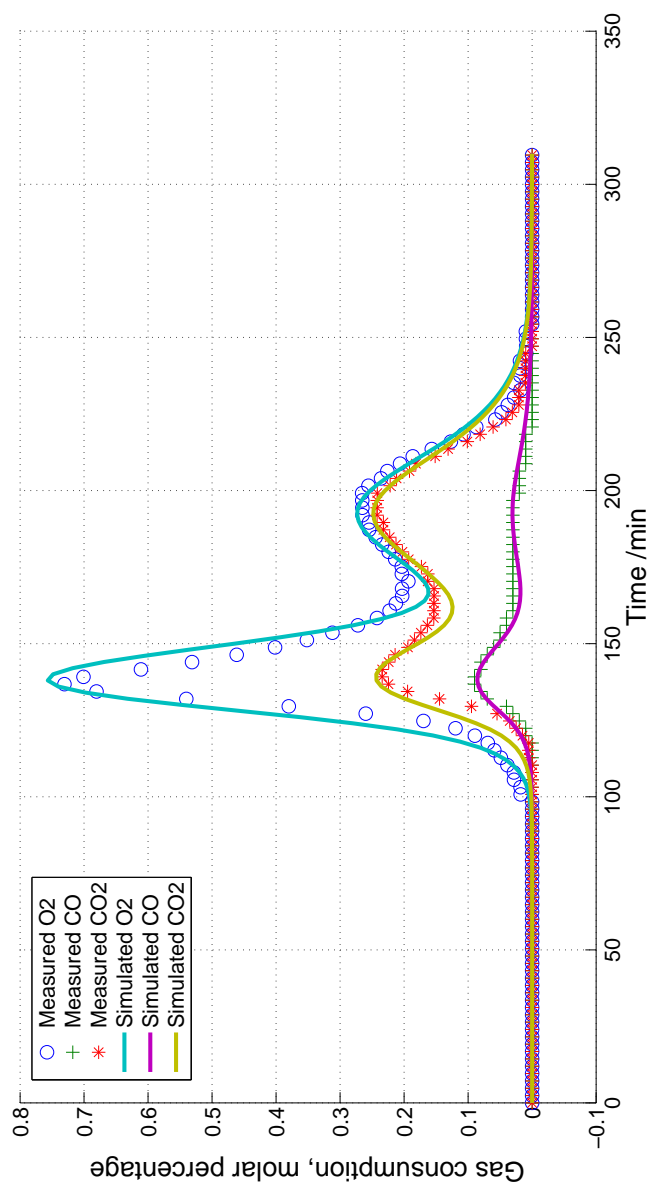


Figure 3.18: VKC simulation results based on the adjusted pre-exponential factors A . Interpreted values of activation energies, reaction orders, and stoichiometry are kept the same as those in the initial interpretations: The heat rate is 1.85 K/min .

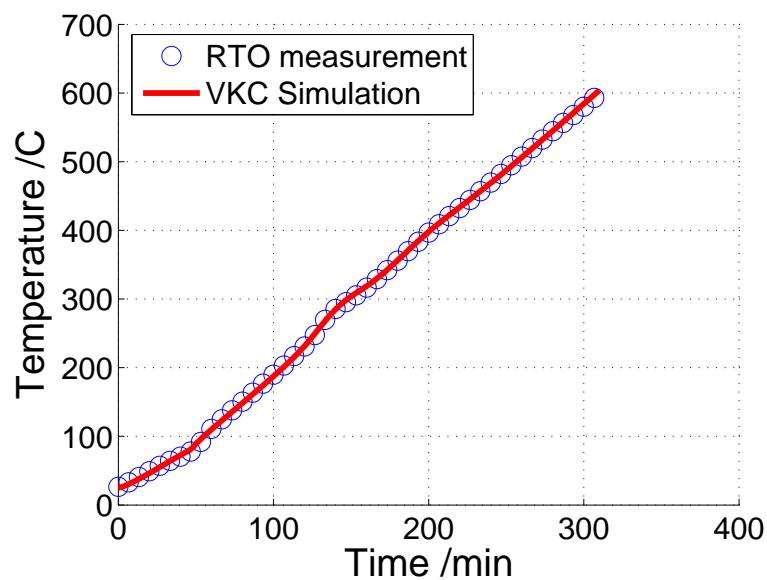


Figure 3.19: Temperature history comparison between the VKC simulation result RTO measurement: the heat rate is 1.85 K/min

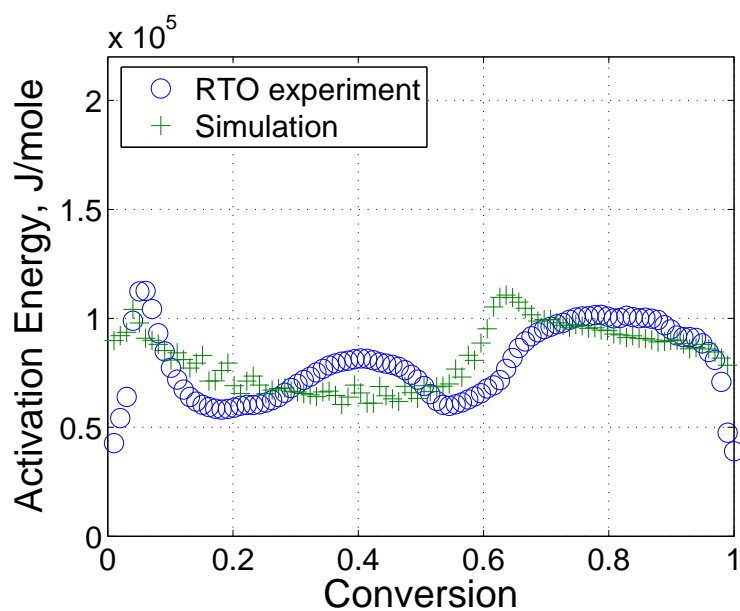


Figure 3.20: Isoconversional fingerprint comparison between the VKC simulation result RTO measurement.

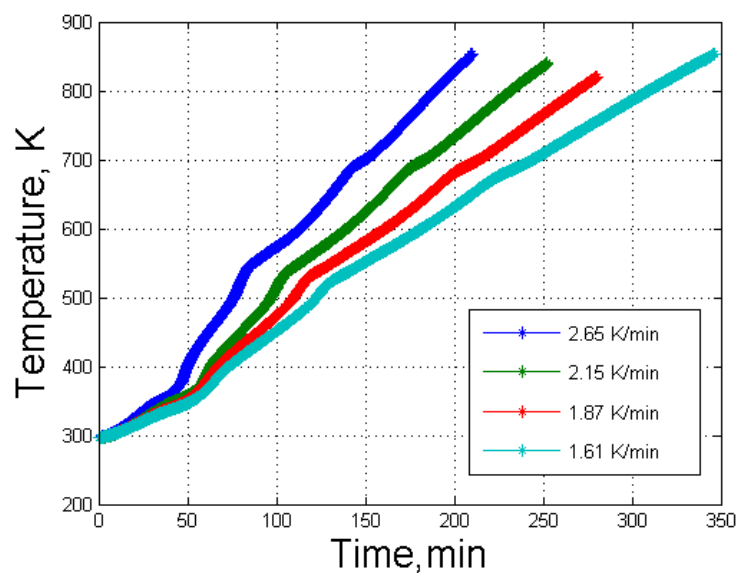
3.4 Discussion

The proposed method combines the isoconversional and conventional principles together to interpret kinetic parameters, activation energy, pre-exponential factor and reaction orders, for reaction model from RTO experiments. The synthetic cases of unit and non-unit reaction orders exhibit very good matches between the model values and the interpreted values of kinetic parameters. The method is applied to build reaction models for two different crude-oil/sand mixtures. A three-reaction scheme is proposed based on reaction stages identified from isoconversional fingerprint as well as RTO effluent data. Stoichiometry is defined from effluent data, activation energy is read from the isoconversional fingerprint, reaction orders are interpreted by processing several sets of RTO experiments using different oxygen compositions in the injection gas stream, and pre-exponential factor is given as an initial guess and then adjusted to match the measurement. The virtual kinetic cell simulation coupled with the proposed model well represents the combustion performance of the crude oil mixture within the kinetic cell, regarding the temperature histories, effluent gas histories, and the isoconversional fingerprint.

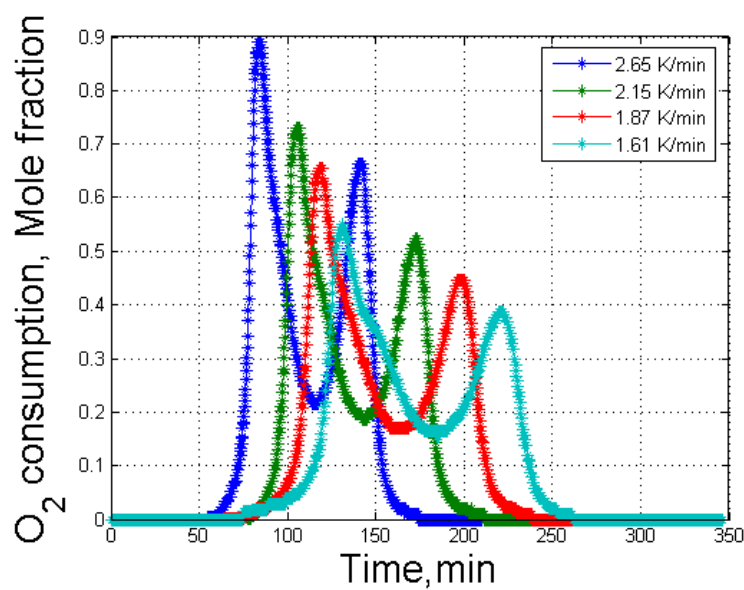
The proposed three-reaction scheme captures major characteristics of crude-oil combustion. Improvement of the proposed scheme is needed to make the simulations match the ignition stage with respect to carbon oxides, and transition stage between LTO and HTO in terms of oxygen profiles. Adding more reactions, such as four or five reactions, to the reaction scheme would make simulations more accurate. Also, adding an intermediate reactant, such as a coke component burned at the LTO stage [17] would improve the transition stage on the isoconversional fingerprint. The additions of reactions or reactants makes the interpretation more complicated, so more work is needed to improve the interpretation method combining the isoconversional principle and conventional methods.

For the 35% oxygen composition cases, eight experiments have been done, in total. Four each for Alaskan and Karamay crude oil cases. The measurement data are shown in Figure 3.21 and 3.22 for the Alaskan and the Karamay crude oil respectively. From the temperature and the effluent gas profiles, they represent very good trends and

a certain degree of consistency. The consistency check ($\ln(dx/dt)$ vs. $-1/RT$), as discussed in Chapter 2, gives poor results showing in Figure 3.23 and 3.24, especially for the Karamay crude oil case. The consistency check for the Alaskan case shows poor consistency in the transition zone between LTO and HTO stages, and for the Karamay case, the consistency check suggests that RTO measurements are not consistent at all.

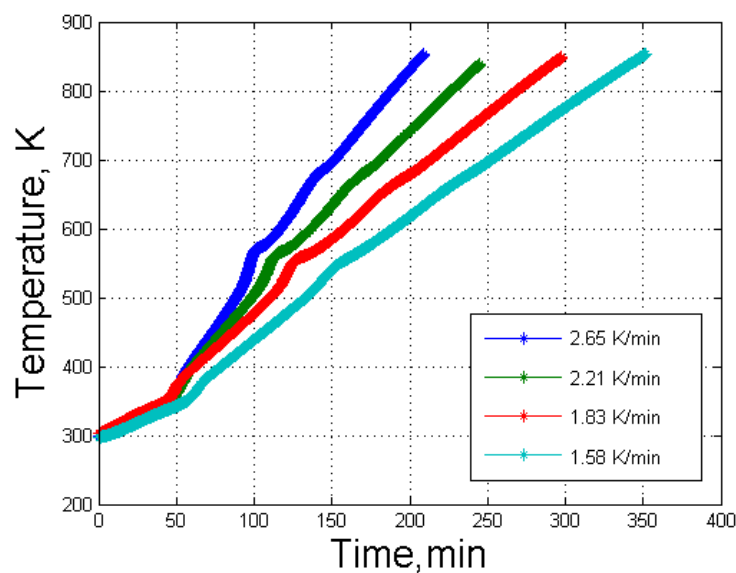


(a) Temperature histories

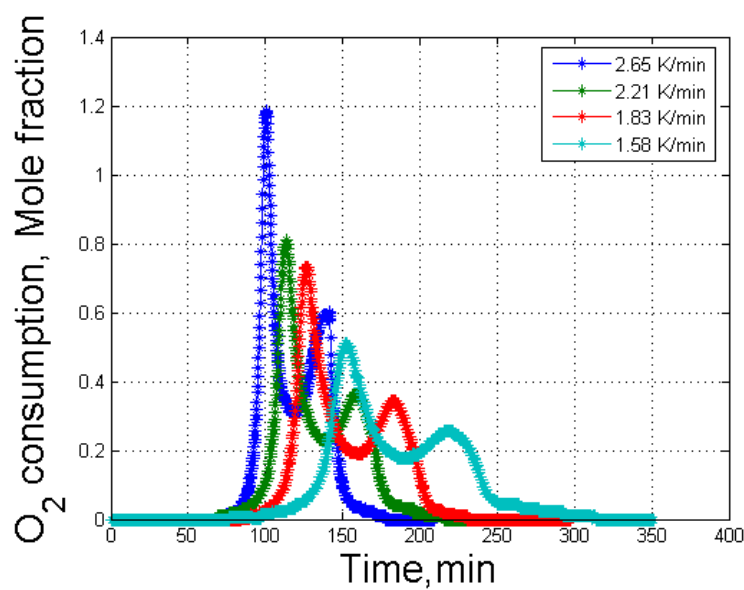


(b) Oxygen consumption histories

Figure 3.21: Alaskan crude oil RTO experiments: 35% oxygen composition.



(a) Temperature histories



(b) Oxygen consumption histories

Figure 3.22: Karamay crude oil RTO experiments: 35% oxygen composition.

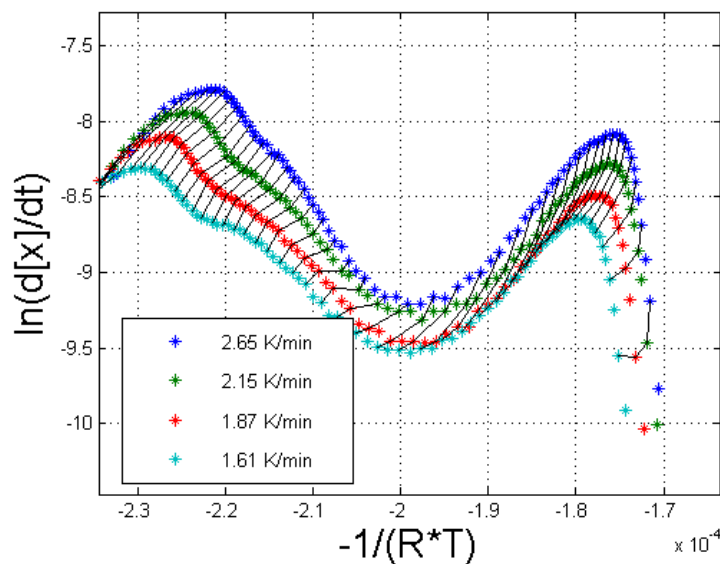


Figure 3.23: Consistency check for the 35% oxygen composition RTO experiments of Alaskan crude oil.

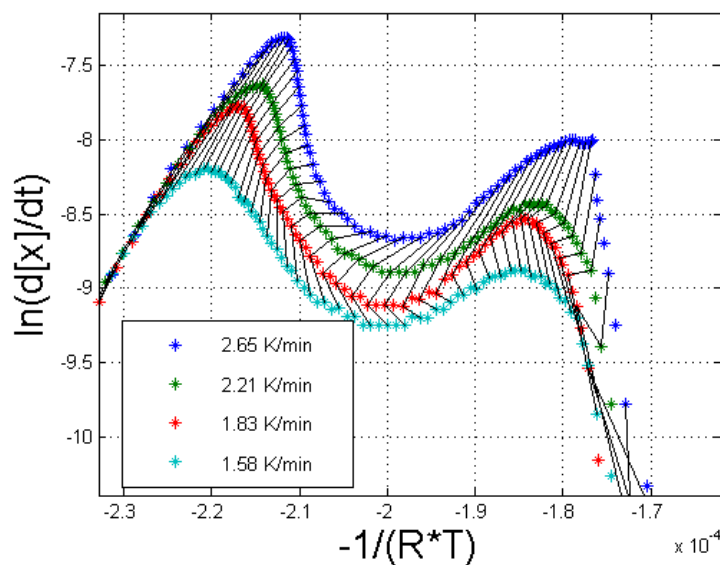


Figure 3.24: Consistency check for the 35% oxygen composition RTO experiments of Karamay crude oil.

Chapter 4

Isoconversional application

The isoconversional principle has strong power to categorize the reaction kinetics within crude-oil combustion in terms of the activation energy fingerprint. The isoconversional fingerprint inherently contains abundant kinetic information. Different reaction stages such as LTO and HTO are clearly identified. Kinetic parameters (activation energy, pre-exponential factor and reaction orders) are interpreted for reaction modeling. In this chapter, the isoconversional fingerprint is used as a qualitative analysis tool to investigate detailed aspects in the ISC process. It is applied to analyze sand and clay surface area effects on ISC kinetics, coke formation under different conditions, and to screen the crude-oil/rock-matrix pair for potential ISC candidates.

4.1 Reservoir matrix effect

Many researchers have shown that sand and clay surface area have a significant effect on crude-oil combustion [111][25][18][47][49]. The addition of clay to the rock matrix enhances the crude-oil combustion by reduction of activation energy. Large surface area and metallic catalytic components of the clay contribute to the enhancement. Vossoughi et al. [110] showed that a combustion tube run of sand/crude-oil mixture failed to achieve combustion front propagation, while a strong self-sustained combustion front was formed when mixing a certain amount of clay with the sand. In another study, Cinar et al. [18] mixed a crude oil with sand of different grain sizes:

Table 4.1: Crude-oil/rock matrix pairs for RTO experiments

Alaskan crude oil	Case 1	60 mesh fired sand + clay
	Case 2	60 mesh fired sand
	Case 3	12 mesh sand
Karamay crude oil	Case 1	reservoir sand
	Case 2	60 mesh fired sand + clay
	Case 3	60 mesh fired sand

sand crushed from reservoir rock (about 10 to 16 mesh) and artificial sand of 60 mesh, and did the combustion tube run. A sustained combustion propagation was observed for the crude oil mixed with 60 mesh sand case. The other one with larger grain size, crushed reservoir rock could not form a propagating temperature front.

Surface area alters the heat conductivity behavior of porous media. Both catalytic effect and surface area influence the reaction paths of the crude-oil combustion, and thus the apparent activation energy. Isoconversional fingerprint exhibits the activation energies as a function of oxygen conversion. Rock matrix effect on the reaction kinetics can be investigated by analyzing the fingerprint interpreted from RTO experiments. Two sets of experiments are conducted using Alaskan crude oil and Karamay crude oil. The crude oil and rock matrix conditions for the RTO experiments are listed in Table 4.1:

4.1.1 Alaskan crude-oil cases

The Alaskan crude-oil has an API of 13.3. Three cases of different sand matrix are considered. They are case 1 with 60 mesh fired sand and clay, case 2 with 60 mesh fired sand and case 3 with 12 mesh fired sand. 25 *grams* of the sand/crude-oil mixture is used in the kinetic cell. The size of the sample for a RTO experiment is defined by a series of RTO tests with different sample sizes so that temperature deviations during LTO and HTO are small enough to make the measurement consistent. The sample size still needs to be large enough to acquire precise effluent gas measurement. 1.5 *L/min* air injection rate is used for each case. The RTO measurements of temperature

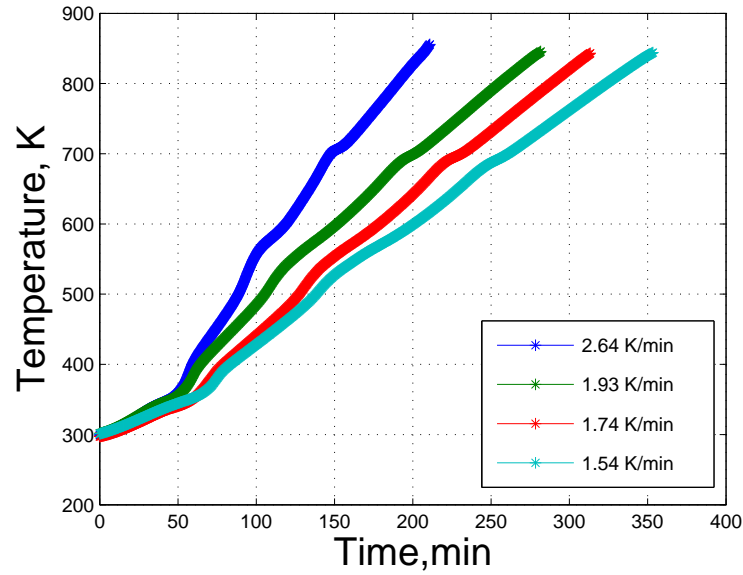
Table 4.2: Oxygen consumption comparison of LTO and HTO for Alaskan crude oil cases

	Peak oxygen consumption ratio	Amount of oxygen consumption ratio
Case 1	1.16	1.86
Case 2	0.81	1.33
Case 3	0.41	0.67

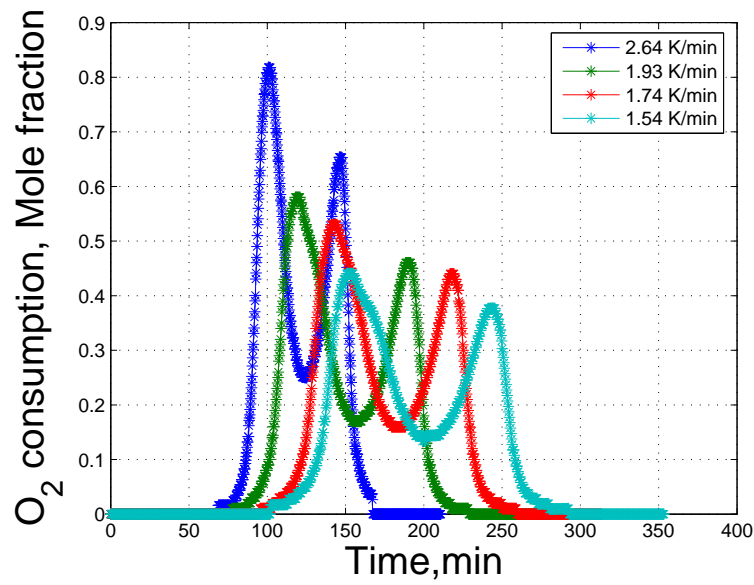
histories as well as oxygen consumption profiles for each experimental case are plotted in Figure 4.1, 4.2, and 4.3 respectively.

Case 1 with clay in Figure 4.1 exhibits very different oxygen consumption behavior from those in both case 2 and case 3, where only the sand of different grain size is mixed with crude oil. The presence of clay significantly enhances the first oxygen consumption hump, that is the low temperature oxidation regime. The enhancement in the LTO reaction stage increases the amount of fuel laid down. Fuel laid down is a critical parameter to evaluate the capability of a self-sustaining combustion front propagation. When the crude oil was mixed with sand only, case 2 and case 3 both show the oxygen consumption peak in LTO is much lower than that of HTO. This means that in the entire combustion process, a large portion of reactions occur at the high temperature regime. Comparing the peak oxygen consumption ratio of LTO and HTO in case 2 and case 3, case 2 has more oxygen consumption in LTO than that of case 3. Case 2 uses fired sand of 60 mesh, and it has larger surface area than the sand of 12 mesh used in case 3. Both cases do not have clay involved. The comparison of oxygen consumption of the three cases are listed in Table 4.2.

When using isoconversional fingerprints to compare the three cases in Figure 4.4, the same conclusion is also made that the clay addition in case 1 much enhances the LTO in terms of amount ratio of oxygen consumption in LTO and HTO, and surface effect is more favorable when using sands of smaller grain size (Table 4.2). When this goes to the kinetic analysis, comparison of the activation energy values in LTO and HTO for the three cases is very close. The LTO activation energies are between 0.7×10^5 and 0.8×10^5 *J/mole*, and the HTO activation energies are roughly 1.2×10^5

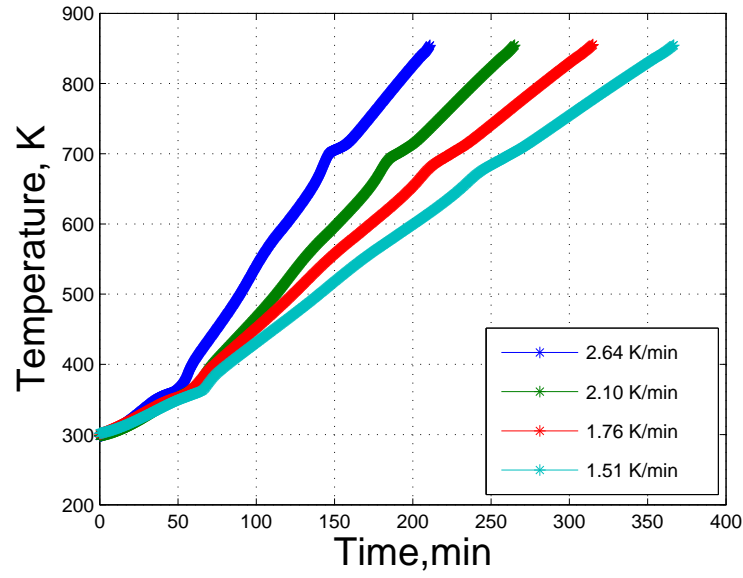


(a) Temperature histories

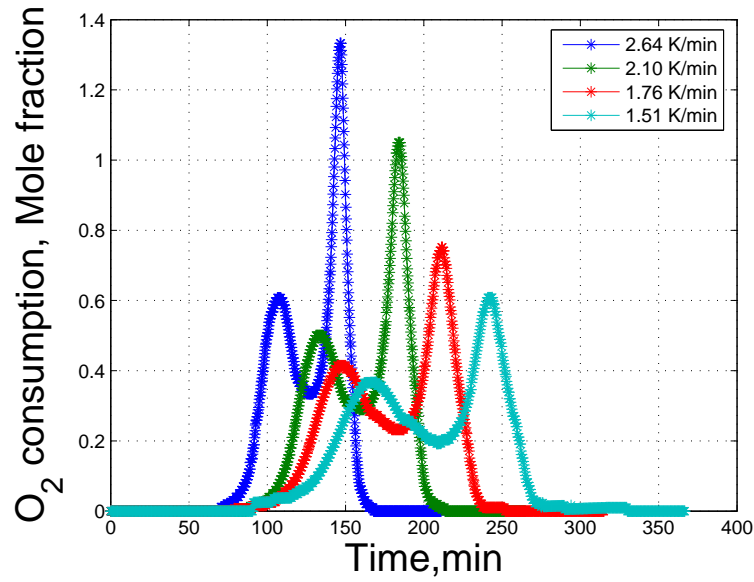


(b) Oxygen consumption histories

Figure 4.1: Alaskan crude oil case 1: 60 mesh fired sand and clay; 25g mixture of 2.04 *wt%* crude oil, 8.16 *wt%* water, 81.63 *wt%* fired sand and 8.16 *wt%* clay; Air injection rate is 1.5 *L/min*.

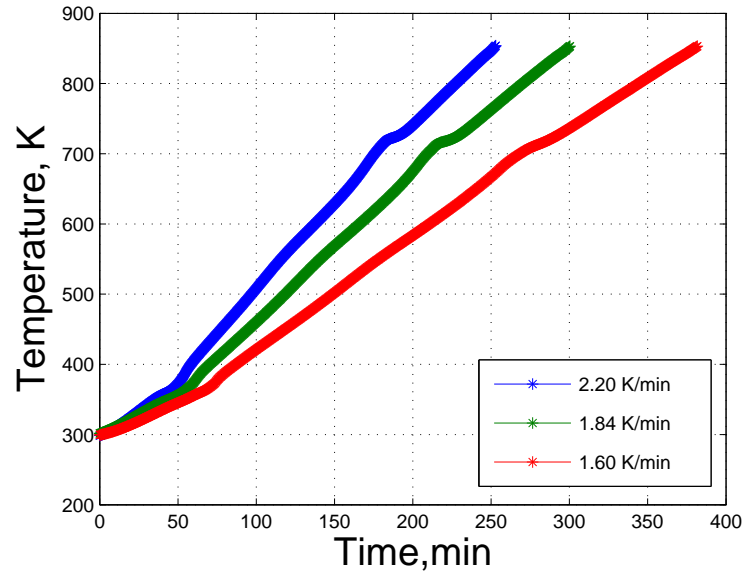


(a) Temperature histories

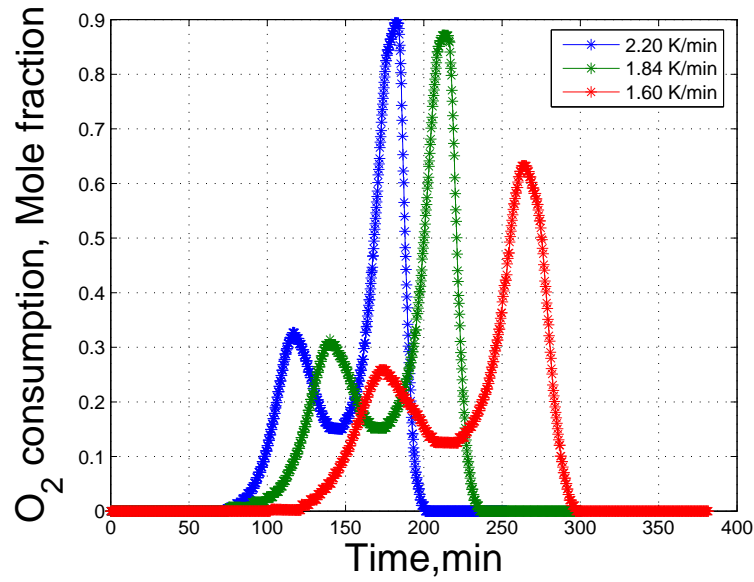


(b) Oxygen consumption histories

Figure 4.2: Alaskan crude oil case 2: 60 mesh fired sand; 25g mixture of 2.04 *wt%* crude oil, 8.16 *wt%* water, 89.90 *wt%* fired sand; Air injection rate is 1.5 *L/min*.



(a) Temperature histories



(b) Oxygen consumption histories

Figure 4.3: Alaskan crude oil case 3: 12 mesh fired sand; 25g mixture of 2.04 *wt%* crude oil, 8.16 *wt%* water, 89.90 *wt%* fired sand; Air injection rate is 1.5 *L/min*.

and 1.3×10^5 *J/mole*. The LTO region shows a flat plateau for all of the three cases, but the shapes of the HTO plateau are very different. Case 1 with clay addition shows a flat plateau in the HTO regime, while case 2 and case 3 show a flat HTO plateau at the beginning but the activation energy increases after the flat region. The increased apparent activation energies are due to some kind of coke residual with greater activation energies. Case 2 and 3 need more energy and higher temperature to burn all of the HTO residues than case 1 with a flat HTO region all the way to $X = 1$.

Besides the interesting LTO and HTO kinetic behaviors in different porous media cases, the negative temperature gradient region (NTGR) is clearly detected in case 2 and case 3 where no clay is present in the matrix. The NTGR is also referred as 'Death Valley' [22] where oxygen uptake decreases while temperature is still increased [70]. The exist once of the NTGR challenges the sustainability of the ISC due to the decrease in the reaction rate. Insufficient heat released from reactions to support high temperature when the reaction rate goes down according to the rate law. Cinar et al. [16][16][17] first investigated the NTGR character by using isoconversional fingerprint and described it using the cool flame theory: an incomplete combustion associated with the NTGR where oxygen uptake as well as heat released, decrease with increasing temperature. On an isoconversional fingerprint, NTGR exists in between the LTO and HTO regions where a local minimum activation energy is reached.

For case 2, the NTGR is located at the conversion region of 0.35 to 0.5, with a minimum activation energy value of 0.5×10^5 *J/mole*, while in the case 3 with larger sand grain size and smaller matrix surface area, the NTGR happens in the conversion region of 0.25 to 0.35 and the smallest activation energy value is about 0.22×10^5 *J/mole*. This means that case 2 more easily forms a good combustion front with a shallow NTGR and later location of it, as compared to case 3 in which sand of larger grain size is used. There is no apparent NTGR observed in case 3 where clay is mixed with the crude-oil sample. The comparison of fingerprints of the three Alaskan cases clearly demonstrates the differences in the reaction kinetic behavior of crude oil coupled with different porous media. The existence of NTGR retards the combustion propagation, while the clay addition removes the NTGR in the reaction path and

enhances crude oil combustion.

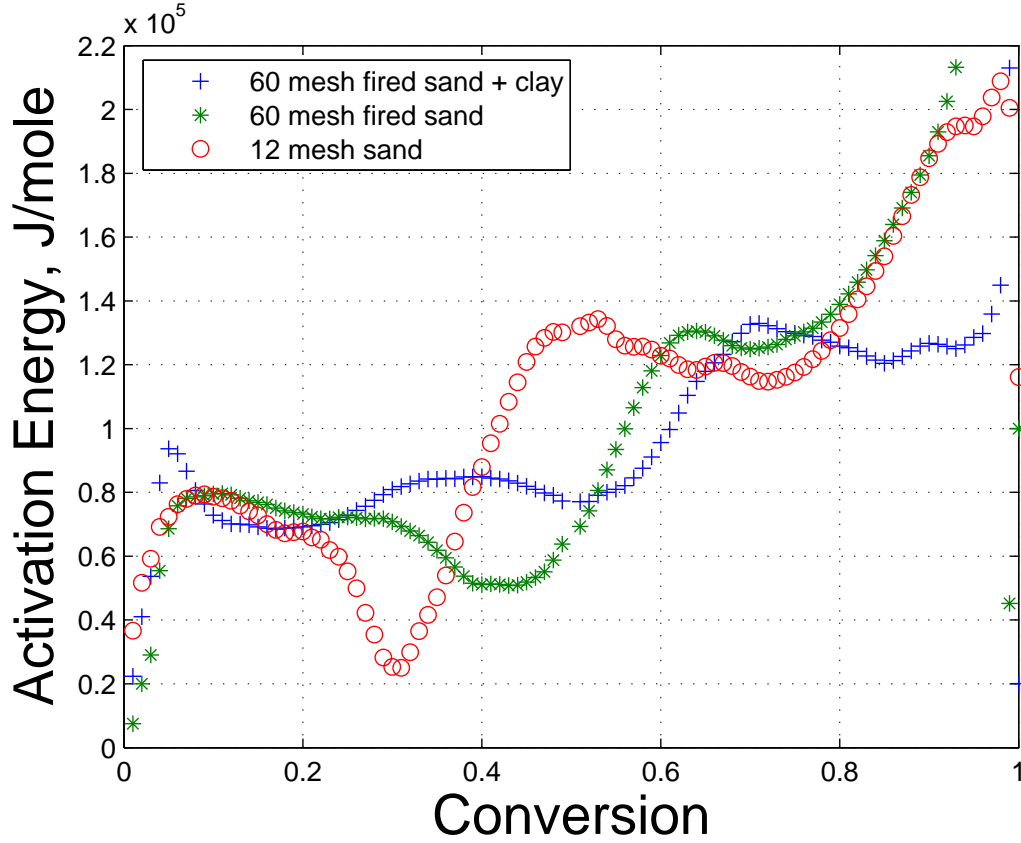


Figure 4.4: Activation energy fingerprints comparison for Alaskan crude oil cases.

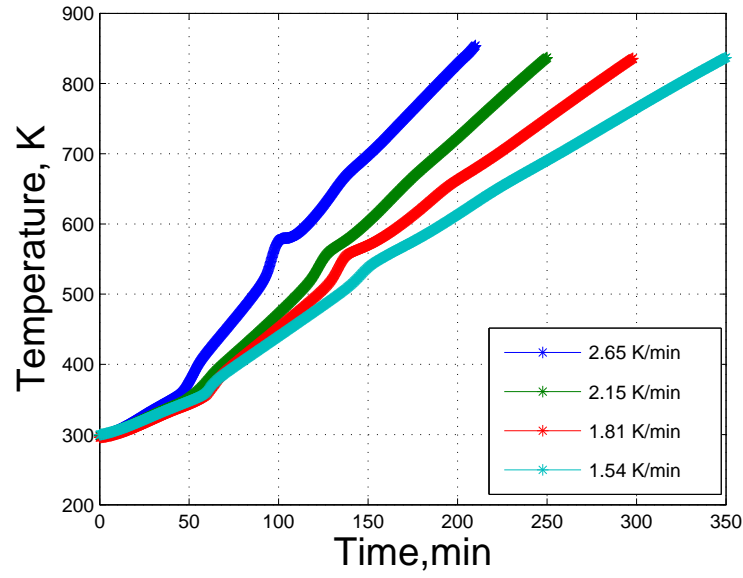
4.1.2 Karamay crude-oil cases

Another three sets of RTO experiments were carried out using the Karamay crude oil sample with 11.8 °API. The sand matrix compositions are listed in Table 4.1 for each case. The sample mixture for each case has a composition of 2.04 *wt%* crude oil, 8.16 *wt%* water, 89.90 *wt%* sand matrix and the air injection rate is 1.5 *L/min*. Case 1 is conducted with a sample mixture of real reservoir sand. The reservoir sand has finer grain size than the fired sand of 60 mesh and contains a certain amount the clay with metallic species. Case 2 is carried with 60 mesh fired sand and clay, case 3 with 60 mesh fired sand only.

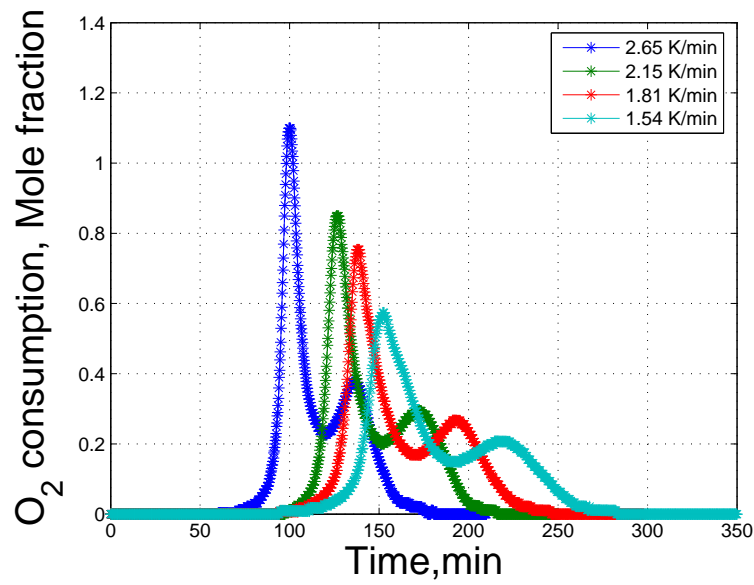
Table 4.3: Oxygen consumption comparison of LTO and HTO for Karamay crude oil cases

	Peak oxygen consumption ratio	Amount of oxygen consumption ratio
Case 1	2.83	1.86
Case 2	3.31	1.86
Case 3	1.72	1.63

RTO measurements of temperature histories as well as oxygen consumption histories for the three cases are plotted in Figure 4.5, 4.6, and 4.7 respectively. The oxygen consumption histories for all of the three case shows similar performance that LTO region consumes more oxygen than the HTO region. Comparison of oxygen consumptions based on oxygen uptake histories for the three cases are listed in Table 4.3. The LTO region is enhanced in both case 1 and case 2 where the porous media contains clay. The same kinetic analysis is done to Karamay cases using the isoconversional fingerprint. The three activation energy fingerprints are very different from each other in both LTO and HTO regions. In the LTO region, case 1 and case 2 have smaller activation energy values than case 3. In the HTO region, case 3 of no clay addition shows the highest activation energy values and has an increasing trend of activation energies when the combustion approaches to the end. Case 2 has a smaller activation energy values in the HTO region than case 3, greater values than case 1, but there is very little increasing trend in activation energies. The clay addition to the sample mixture contributes to the decrease of activation energies in case 2. The same clay effect is seen in the HTO region of case 1, where a flat activation energy plateau is formed. Analyzing the reaction region in between the LTO and HTO stages, case 3 without clay addition formed an obvious NTGR, which holds a minimum activation energy value around $0.5 \times 10^5 \text{ J/mole}$. Case 1 and Case 2 also have a NTGR-like shape in between the LTO and HTO region, but the minimum activation energy values of it are very close to that of the early stage of the LTO region. Overall, case 1 with the reservoir sand has the smoothest fingerprint regarding the difference between the maximum and minimum activation energies, case 2 with the fired sand and clay

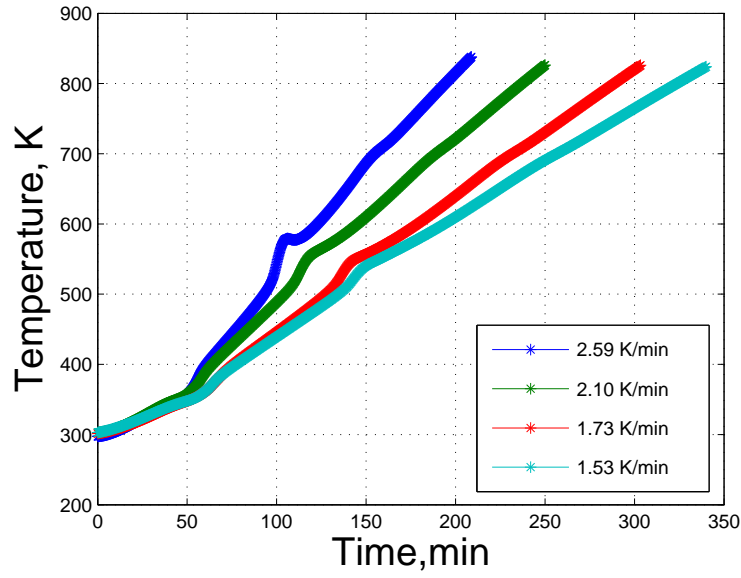


(a) Temperature histories

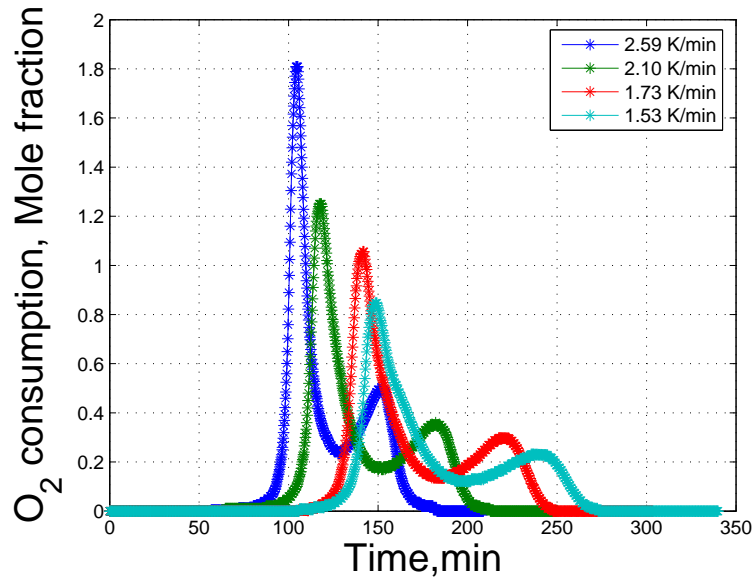


(b) Oxygen consumption histories

Figure 4.5: Karamay crude oil case 1: reservoir sand; 15g mixture of 2.04 *wt%* crude oil, 8.16 *wt%* water, 89.90 *wt%* fired sand; Air injection rate is 1.5 *L/min*.

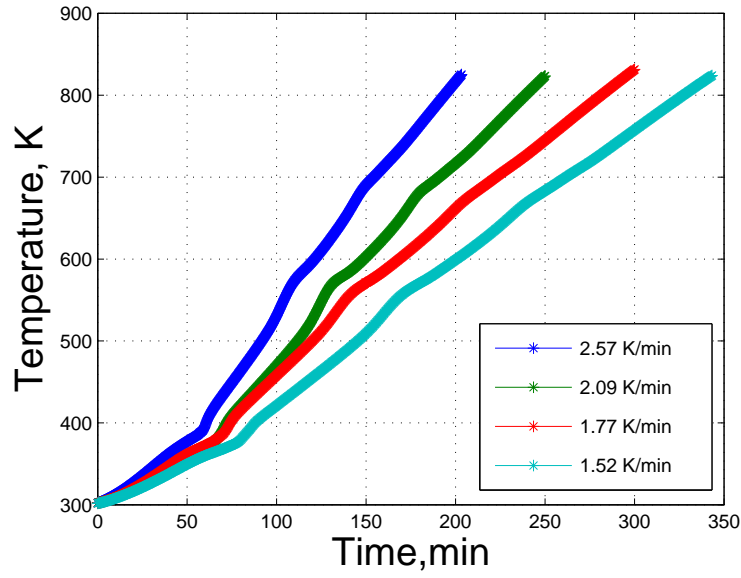


(a) Temperature histories

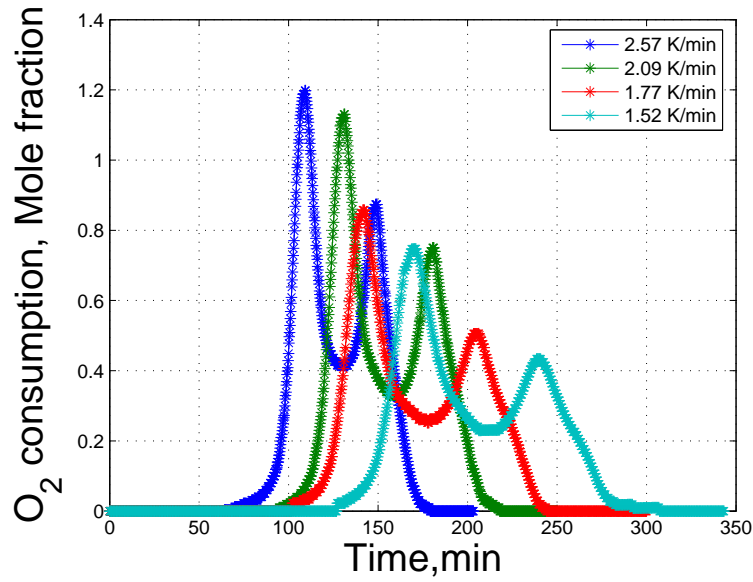


(b) Oxygen consumption histories

Figure 4.6: Karamay crude oil case 2: 60 mesh fired sand and clay; 25g mixture of 2.04 *wt%* crude oil, 8.16 *wt%* water, 81.63 *wt%* fired sand and 8.16 *wt%* clay; Air injection rate is 1.5 *L/min*.



(a) Temperature histories



(b) Oxygen consumption histories

Figure 4.7: Karamay crude oil case 3: 60 mesh fired sand; 25g mixture of 2.04 *wt%* crude oil, 8.16 *wt%* water, 89.90 *wt%* fired sand; Air injection rate is 1.5 *L/min*.

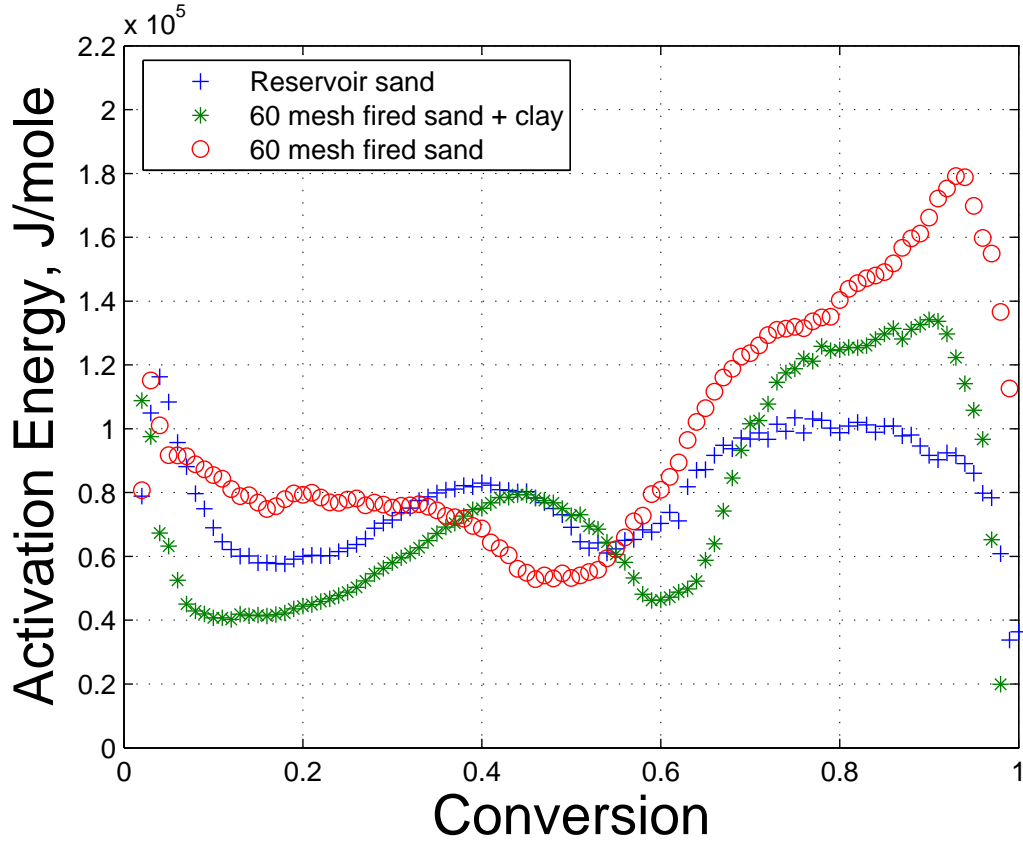


Figure 4.8: Activation energy fingerprints comparison for Karamay crude oil cases.

addition enhances the combustion in both LTO and HTO regions. Case 1 and case 2 have more favorable combustion behavior than case 3 because of larger surface and clay addition.

Based on the two crude oil samples and six RTO experiments with different porous media, the conclusion is drawn that surface area and clay effect of porous media has significant impacts on the activation energy for the whole combustion process. The isoconversional fingerprint is very useful to demonstrate the changes in the reaction paths and to identify reaction regimes, such as LTO, HTO, and NTGR.

4.2 Coke formation investigation

In the low temperature oxidation (LTO) region, series and parallel reactions [17], including dehydrogenation, cracking, and condensation, produce a carbonaceous residue on the surface of porous media. The carbonaceous residue, also referred to as coke, is a kind of solid hydrocarbon components insoluble in toluene. The heavy fraction of the crude oil, asphaltenes, is the major source to produce coke composition during ISC. The LTO reactions increase the content of asphaltene while decreasing the content of resin [73]. When crude oil reacts under an inert gas condition like nitrogen, coke is formed after an induction period under the isothermal condition of 673 K [117]. On the other hand, when under air flow condition, coke is formed immediately when the temperature goes up [17]. The amount of coke formation is a critical index for the quantity of fuel available for a self-sustainable combustion: excessive fuel deposition consumes too much crude oil and oxygen, making the advance of the combustion front very slow and the production not economical, while insufficient fuel deposition may not provide enough heat to maintain a self-sustained combustion process.

Wiehe et al. [117] used an isothermal batch reactor to study coke formation under nitrogen and air conditions, reporting different induction time for coke formation. Cinar et al. [17] followed Wiehe's way to produce coke in a quartz tube reactor under isothermal condition. They investigated two kinds of coke formed under nitrogen flow and air flow. A conclusion similar to Wiehe's is gained that coke is formed immediately under the air flow condition at atmospheric pressure and at 673 °C, while under the nitrogen flow condition, a 45 min induction period is needed to produce a significant amount of coke. XPS for coke surface scanning indicates oxygen functional groups exist on the surface of coke precipitated under air flow condition.

A stainless steel isothermal kinetic cell (KC) shown in Figure 4.9 is designed for coke formation under different gas flow condition. The isothermal KC has a stainless steel body that is 2.5 cm in diameter and 12 cm in length. Swagelock fittings are used to seal both ends of the cell. Gas is preheated initially and then injected through the bottom fitting. A thermal well is inserted to the center of the cell to record temperatures. Production gases travel through the production well in the top fitting.

Comparing to the quartz tube reactor [17], the stainless steel isothermal KC can operate at elevated temperature. Meanwhile, production gas is conducted to the gas analyzer so that the progress of a isothermal experiment is monitored and precise control is managed.

The coke formation investigation follows Cinar's method [17] and improvements on the workflow are introduced. A certain amount of crude-oil/sand mixture is padded into the KC. Pressure is elevated with gas injection till it reaches the prescribed pressure condition (normally 100 *psi* is applied). The isothermal KC is put in the furnace with a pre-set constant temperature. The long tube conducts heat from the furnace to preheat injection gas. Temperature and effluent gas data are recorded and monitored to determine when to quench the experiment. When the set time is reached, the isothermal KC is taken outside the furnace and cold water is sprayed immediately until the KC temperature goes under 40 °C. The formation coke is taken out for toluene extraction, and then it is dried out overnight in the vacuum oven. The experiments are repeated until enough coke is made for further XPS analysis and RTO experiments. XPS analysis is conducted to analyze chemical functional groups on the coke surface. RTO experiments are carried out to get the isoconversional fingerprint for the coke activation energies.

A mixture of Karamay crude-oil and the reservoir sand is used. The mixture composition is of 2.04 *wt%* crude oil, 8.16 *wt%* water and 89.90 *wt%* reservoir sand. Exactly 45 *grams* of the mixture is used for each experiment. The pressure within the kinetic cell is 100 *psi* that is the same as that used in RTO experiments. Two kinds of coke, one formed under the air flow condition and the other under the nitrogen flow condition, are investigated.

4.2.1 Coke formed under air

The coke formed in the LTO stage is the major fuel for the HTO burning. Its reaction kinetics controls the heat releasing which is essential to support the combustion front propagation. Adegbesan et. al. [2] proposed a reaction scheme for LTO (Reaction scheme 4.1), that includes the reaction paths to generate coke during the LTO period.

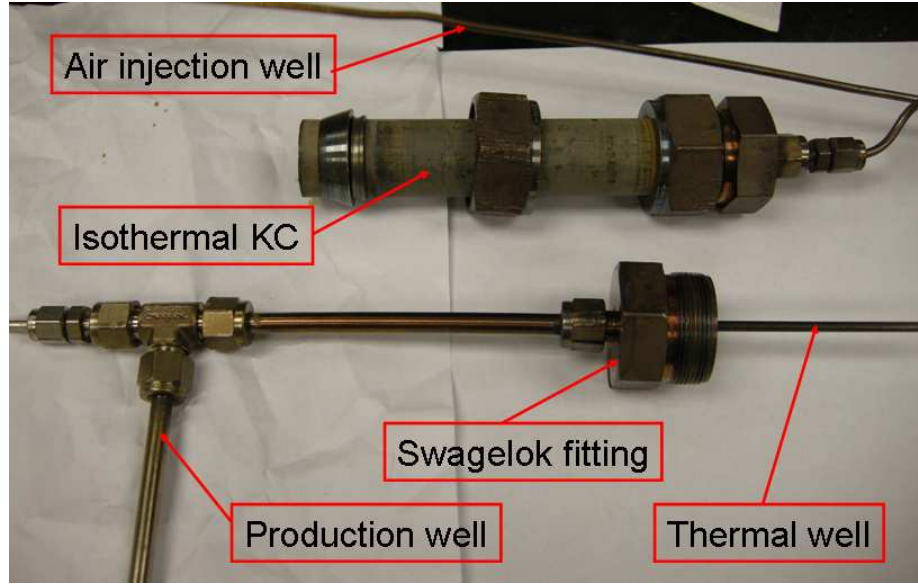


Figure 4.9: The kinetic cell for coke formation study in the isothermal condition.



The first attempt of the coke investigation is to determine the constant temperature value used in the isothermal experiment through an RTO experiment. The result of which is shown in Figure 4.10. The termination temperature value should be below the temperature triggering the HTO reactions and high enough to make LTO reaction progress quickly. According to the RTO experiment result in Figure 4.10, LTO starts at around 200 °C and terminates at around 330 °C. So 300 °C is selected for isothermal experiments.

The air injection rate of 2 L/min is used for the isothermal experiments. In total, four experiments are carried out with a sample mixture of 45 g for each. Temperatures and effluent gas data are shown in Figure 4.11. A temperature of 300 °C is set as the constant temperature for the furnace. The mixture within the kinetic cell is heated up to 283 °C in about 45 minutes and then the temperature is kept constant.

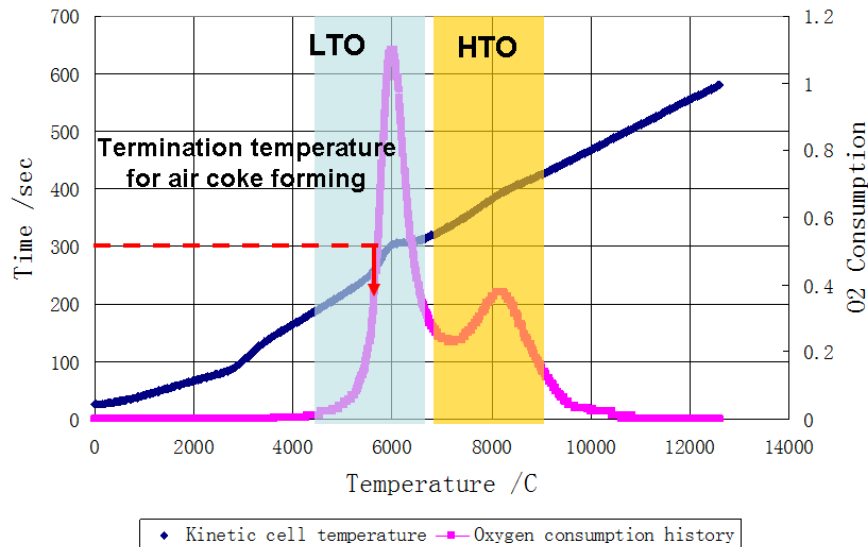


Figure 4.10: Defining the termination temperature for the isothermal experiment of air coke formation: 300 °C is selected.

The temperature gap is caused by the heat balance within the kinetic cell. Oxygen consumption is increased with the elevated temperature. The constant temperature of 283 °C is kept until LTO is nearly finished, that is oxygen consumption approaches a plateau in about 105 minutes. The kinetic cell is taken out of the furnace quickly and water is sprayed to cool it down immediately. Temperature drops from 283 °C to about 40 °C in 5 minutes. Oxygen consumption goes to zero when the kinetic cell is cooled down. Coke is collected from four experiments, crushed to make a homogeneous mixture and then cleaned by toluene to extract heavy residues of crude-oil. The coke is dried by placing it in the vacuum cell for 2 days and then it is ready for further investigation.

The kinetic analysis of the coke combustion is studied by RTO experiments and isoconversional interpretation. A coke mixture of 30 gram is put into the conventional kinetic cell. An air injection rate of 1.5 L/min is used. Four RTO experiments are conducted and temperature and effluent gas histories are shown in Figure 4.12. The oxygen consumption presents only one hump during the ramped temperature process, because LTO reactions are nearly finished in the isothermal experiments and residual

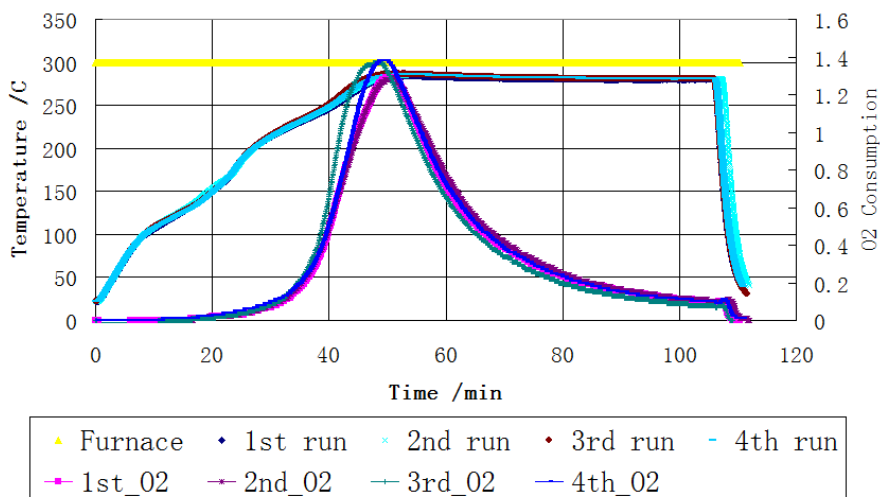
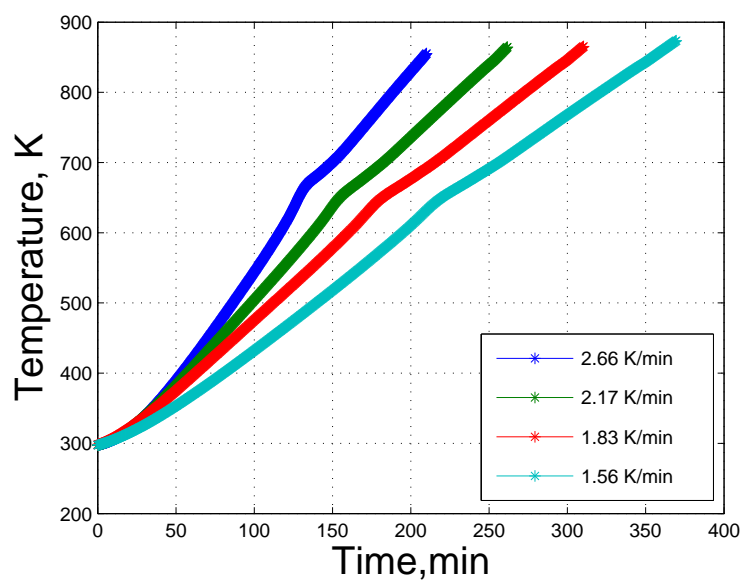
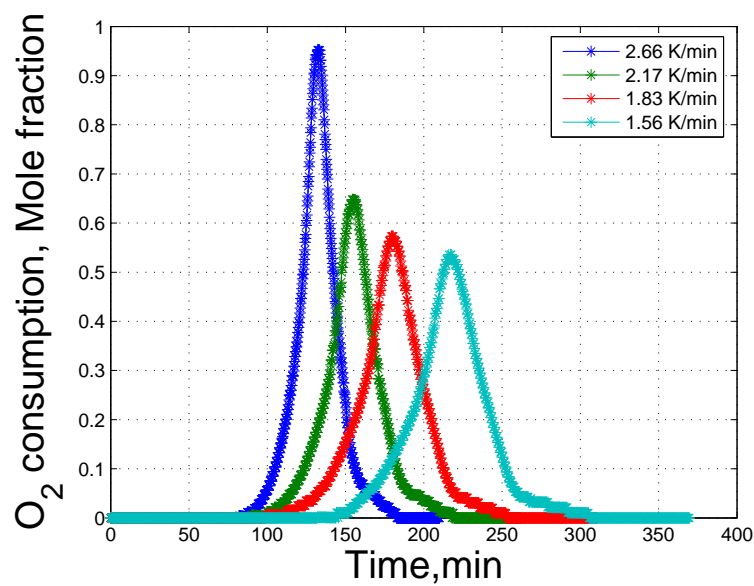


Figure 4.11: Coke is formed in the isothermal experiments.

heavy components are removed by toluene, only coke which is the major fuels for HTO reacts with oxygen in RTO experiments. The isoconversional fingerprint in Figure 4.13(a) presents a flat plateau of activation energy values, which supports the argument that one lumped reaction is enough to described the reaction kinetics for coke combustion. When the activation energy values in Figure 4.13(a) compared with those in the HTO stage of the entire crude-oil combustion shown in Figure 4.13(b), they match each other fairly well. The interesting result strongly supports the capability of isoconversional principle for deconvolving the multi-step reaction mechanism for crude-oil combustion.

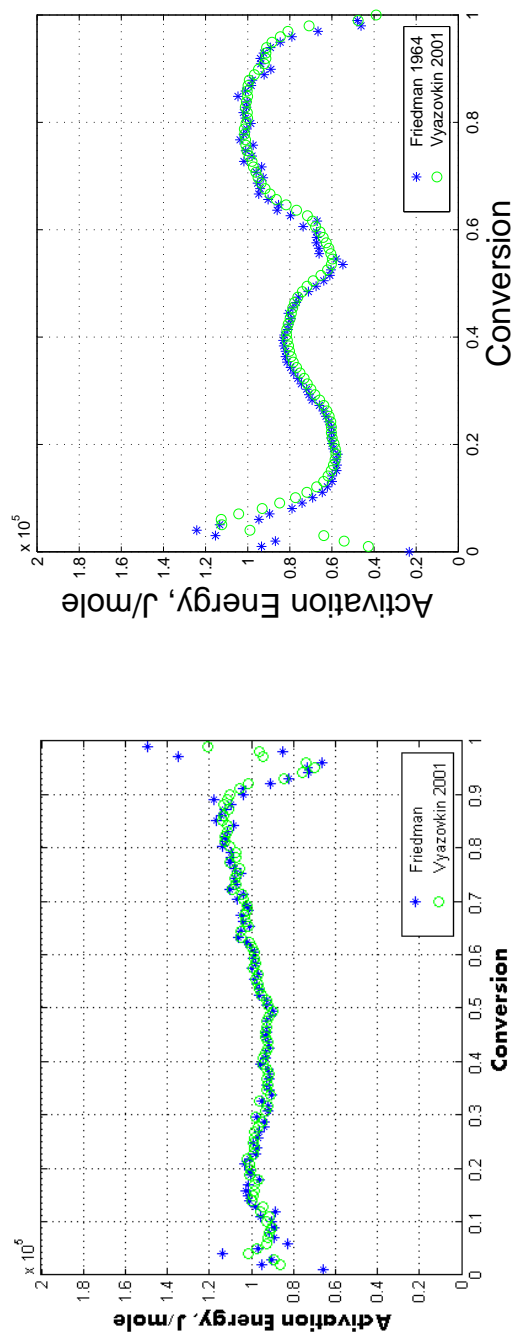


(a) Temperature histories



(b) Oxygen consumption histories

Figure 4.12: RTO experiments for the Karamay air coke.



(a) Activation energy fingerprint for Karamay air coke (b) Activation energy fingerprint for Karamay crude oil

Figure 4.13: Comparison between the activation energy fingerprints for Karamay air coke and crude oil combustion: the activation energy values on fingerprint of air coke are very close to the values of HTO region on the fingerprint of crude oil.

4.2.2 Coke formed under nitrogen

Pyrolysis reactions happen where oxygen concentration is very low and temperature is high enough to break molecular bonds of hydrocarbons, releasing light hydrocarbons such as methane. During an ISC process, pyrolysis takes place in three stages: ignition where nitrogen is injected and a heat is applied; coke zone in front of the combustion zone where oxygen is not able to penetrate the combustion front, only nitrogen and carbon oxides are present; the medium temperature reaction stage in between the LTO and HTO [8][21]. One of the products of the pyrolysis reaction is coke. It is regarded as the critical reactant during the ignition period and temperature front propagation. Hayashitani et. al. [38] proposed a reaction scheme for thermal cracking of crude oil, that is composed of three reactions and four components, asphaltenes, maltenes, coke and distillates (Reaction scheme 4.2).



Injection of N_2 gas to obtain inert conditions is done to generate pyrolysis coke (N_2 coke) in the isothermal experiments. The same procedure is conducted as that used for air coke investigation. The first is to define the termination temperature through an RTO test shown in Figure 4.14. The temperature of $420^\circ C$ is selected as methane is produced by pyrolysis reactions. The sample mixture of 45 gram is put into the isothermal kinetic cell, pressure is fixed at 100 *psi*, and a N_2 injection rate of 2 *L/min* is applied. Four isothermal experiments are carried out and the heavy residues within the porous media are removed by toluene.

RTO experiments are conducted to investigate the reaction kinetics of N_2 coke. Each experiment uses a coke mixture of 30 *grams*, and totally four RTO experiments are conducted, of which the temperature and effluent gas histories are shown in Figure 4.15. N_2 coke combustion represent a slight difference in oxygen consumption histories

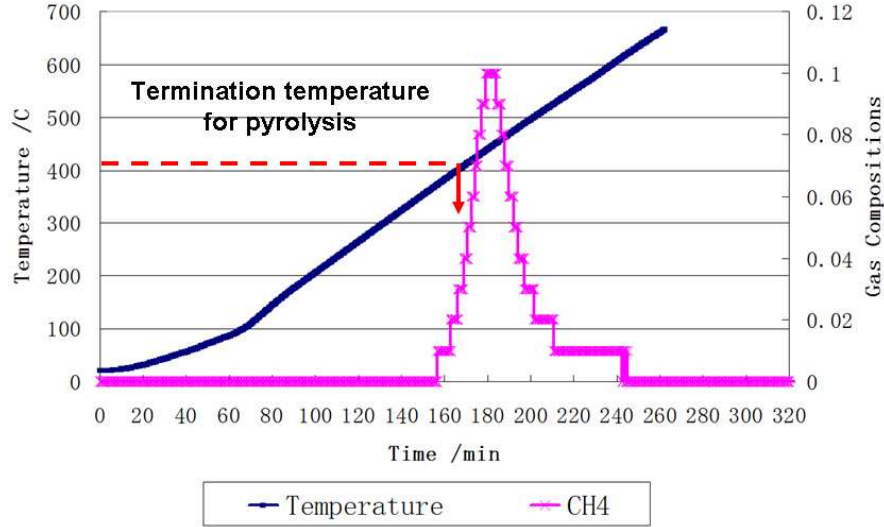
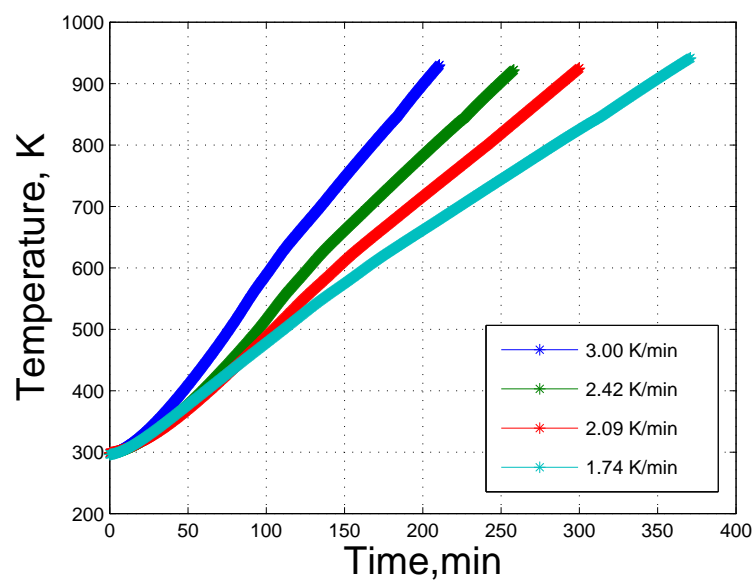


Figure 4.14: Defining the termination temperature for the isothermal experiment of N_2 coke formation: $420^\circ C$ is selected.

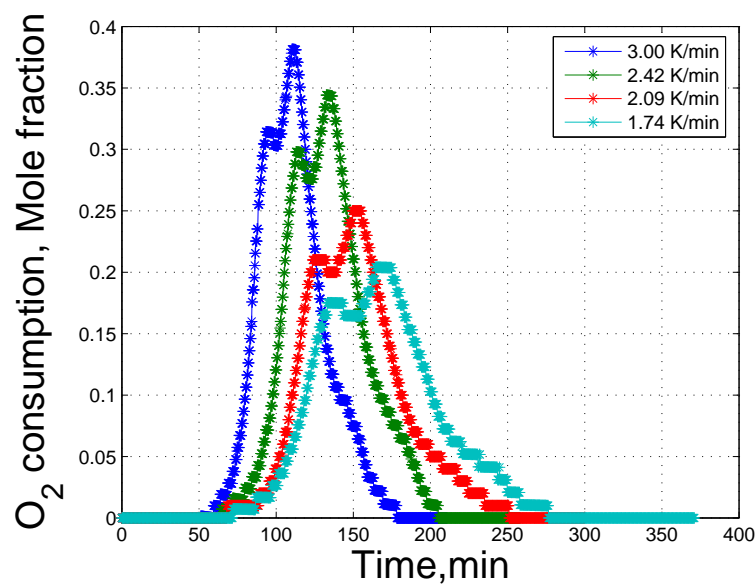
when compared to that of the air coke. Two oxygen consumption humps are observed and they are very close to each other. The isoconversional fingerprint on Figure 4.16 shows two reaction stages corresponding to the two oxygen humps. The two reaction stages have activation energies around 0.8×10^5 and 1.0×10^5 $J/mole$. Comparing with the activation energy of air coke, which is around 1.0×10^5 $J/mole$, these two kinds of different coke represents very similar kinetic character. This is also a good news for ISC modeling that when building a reaction model for burning, we do not really need to separate coke formed in different conditions, such as LTO and pyrolysis. Similar conclusion can be seen in research of Belgrave et al. [6].

4.2.3 XPS analysis

The basic theory of the XPS technique is to estimate the binding energies of the element. The solid sample is mounted on a stage within a vacuum. Monochromatic X-Rays bombard the sample, causing electrons to be released from the sample surface. The electron energy is counted and binding energies are estimated to produce



(a) Temperature histories



(b) Oxygen consumption histories

Figure 4.15: RTO experiments for the Karamay N2 coke

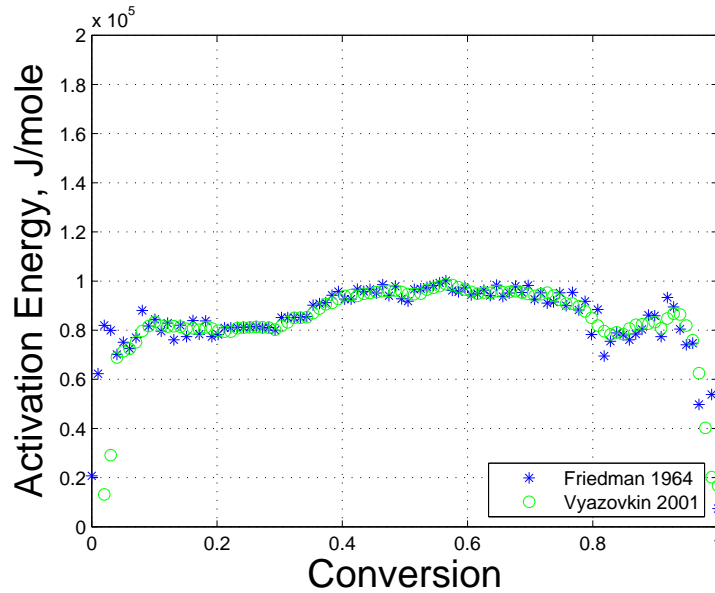


Figure 4.16: Activation energy fingerprint for Karamay N_2 coke

a spectrum of electron intensity as a function of electron energy [11][17]. Using XPS analysis, chemical elements and functional groups on the sample surface are determined.

XPS analysis is used to investigate the difference between coke formed under air and nitrogen conditions. Four spots are chosen for each coke sample. XPS survey spectra for the air coke and the nitrogen coke is shown in Figures 4.17 and 4.18 respectively. Elements of oxygen and carbon on the coke surface are identified from the survey. The ratios of oxygen and carbon are listed in Table 4.4. The oxygen compositions are detected on the coke formed under nitrogen condition. The oxygen may come from the crude-oil or from some residual air within the vacuum. Therefore, it is not the existence of oxygen on the coke surface that is interesting to us, but the oxygen carbon ratios. According to Table 4.4, the coke formed under the air flow condition has greater oxygen-carbon ratios across the sample than the coke formed under nitrogen condition. This suggests that the coke formed in the LTO reactions has oxygen bonding on the surface.

High resolution XPS spectra of coke precipitated under the air and the nitrogen

flow conditions is shown in Figure 4.19. C-O functional group can be clearly seen on the air coke sample, while only carbide is detected on the nitrogen coke sample.

Table 4.4: Oxygen carbon ratios on the surface of different coke under air and nitrogen.

Coke under air	(A)	(B)	(C)	(D)
Oxygen	40.84%	48.51%	39.64%	54.99%
Carbon	47.36%	51.49%	60.36%	45.01%
Ratio	0.86	0.94	0.66	1.22
Coke under nitrogen	(A)	(B)	(C)	(D)
Oxygen	40.65%	40.83%	39.28%	36.66%
Carbon	59.35%	59.17%	60.72%	63.34%
Ratio	0.68	0.69	0.65	0.58

4.3 ISC candidate screening

In-situ combustion has been successfully applied in many unconventional crude oil fields since the first ISC pilot in the former Soviet Union in 1933-1934 and later a field production in the USA in 1950-1951 [102][91]. Over the 80 years of research and experiences on the field operation in ISC projects, a consensus has been reached that screening of candidate fields is essential to reduce the failure risk of a commercial field project. When evaluating the feasibility of this EOR technique in a certain crude-oil reservoir candidate, reservoir geology, fluid properties and rock mineralogy need to be analyzed due to their impact factors for the success of a field implementation.

Practically in the laboratory research, considerations of impact from rock and fluid properties and the interaction between them are taken into account, while reservoir geological impacts are neglected because of the limitation on generating heterogeneity or matrix fractures in the combustion tube scale. Monitoring ISC processes at the field scale is very difficult, however, lab-scale combustion tube tests can mimic the burning characteristics so that we can study ISC with effects of varying process conditions. The combustion behavior primarily depends on its reaction kinetics. We

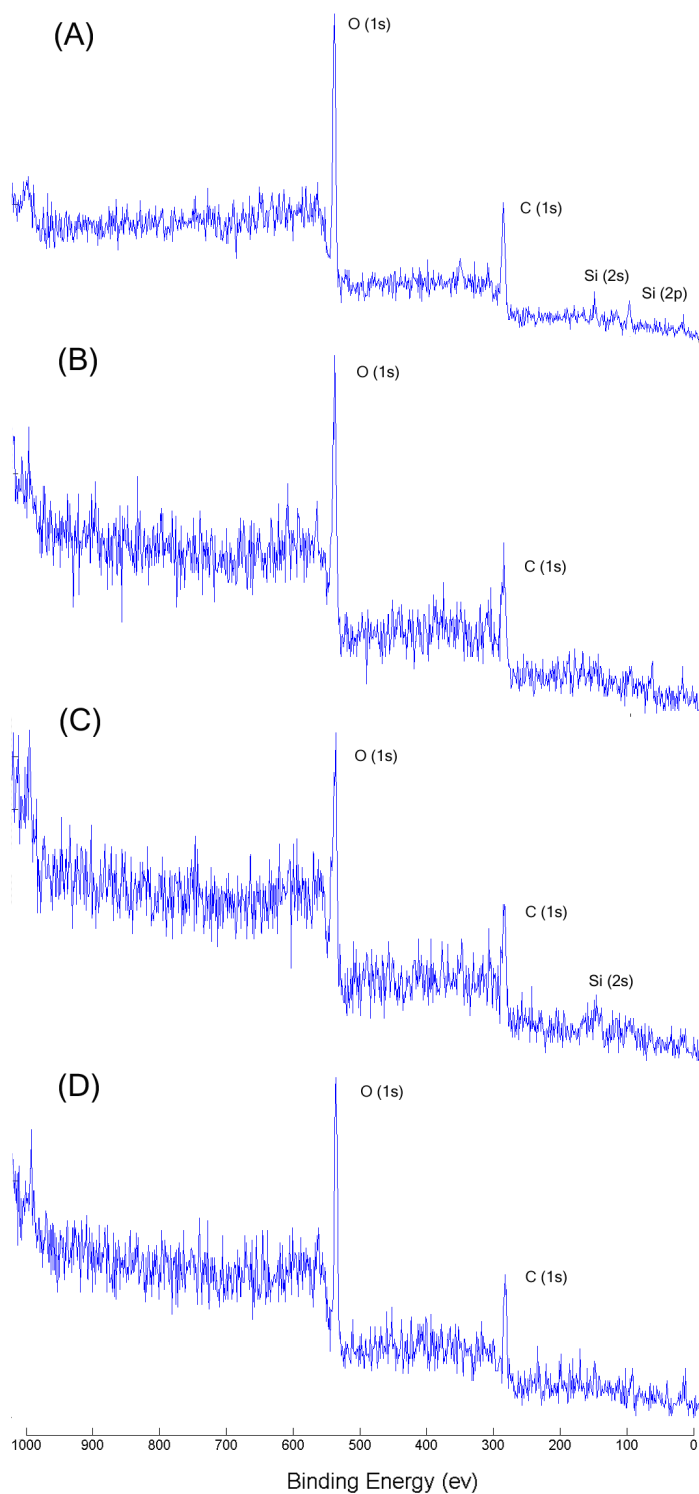


Figure 4.17: XPS survey spectra of coke formation under air flow condition. Four spots are scanned.

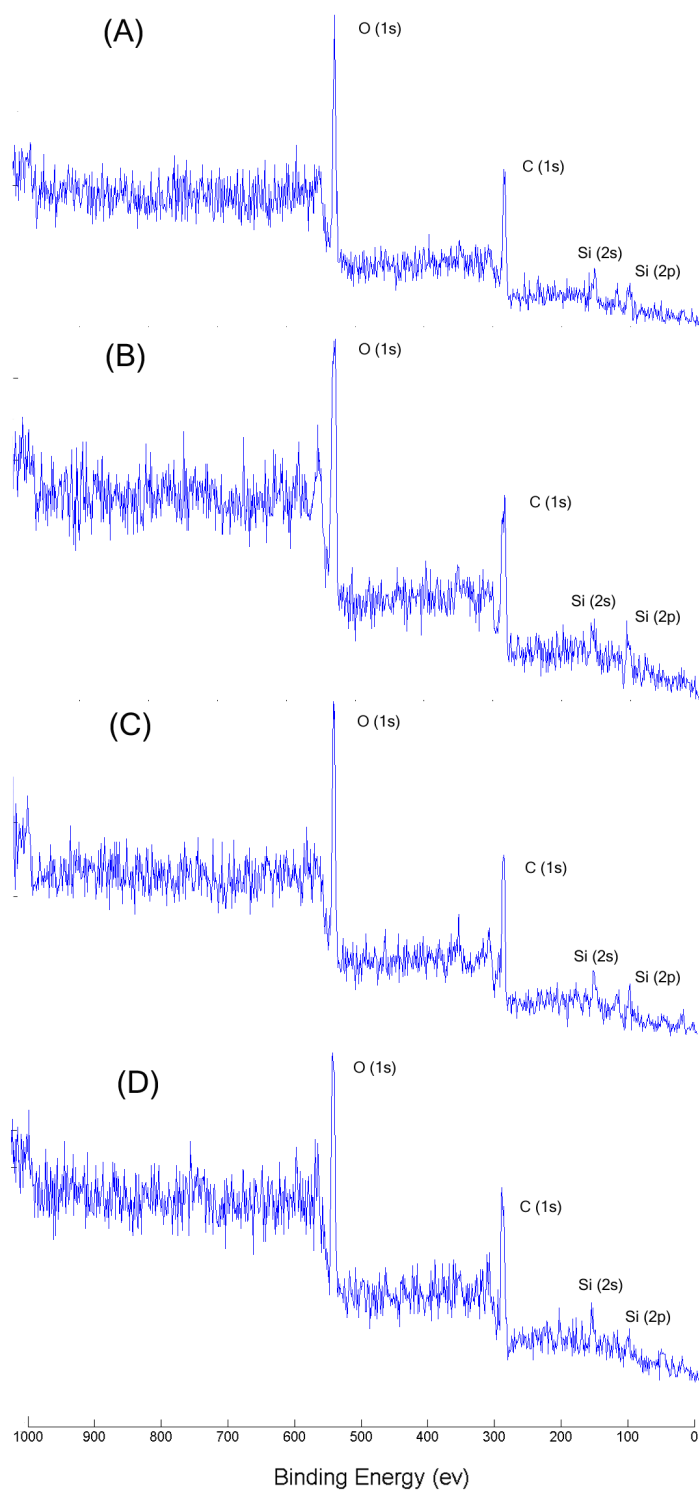


Figure 4.18: XPS survey spectra of coke formation under nitrogen flow condition. Four spots are scanned.

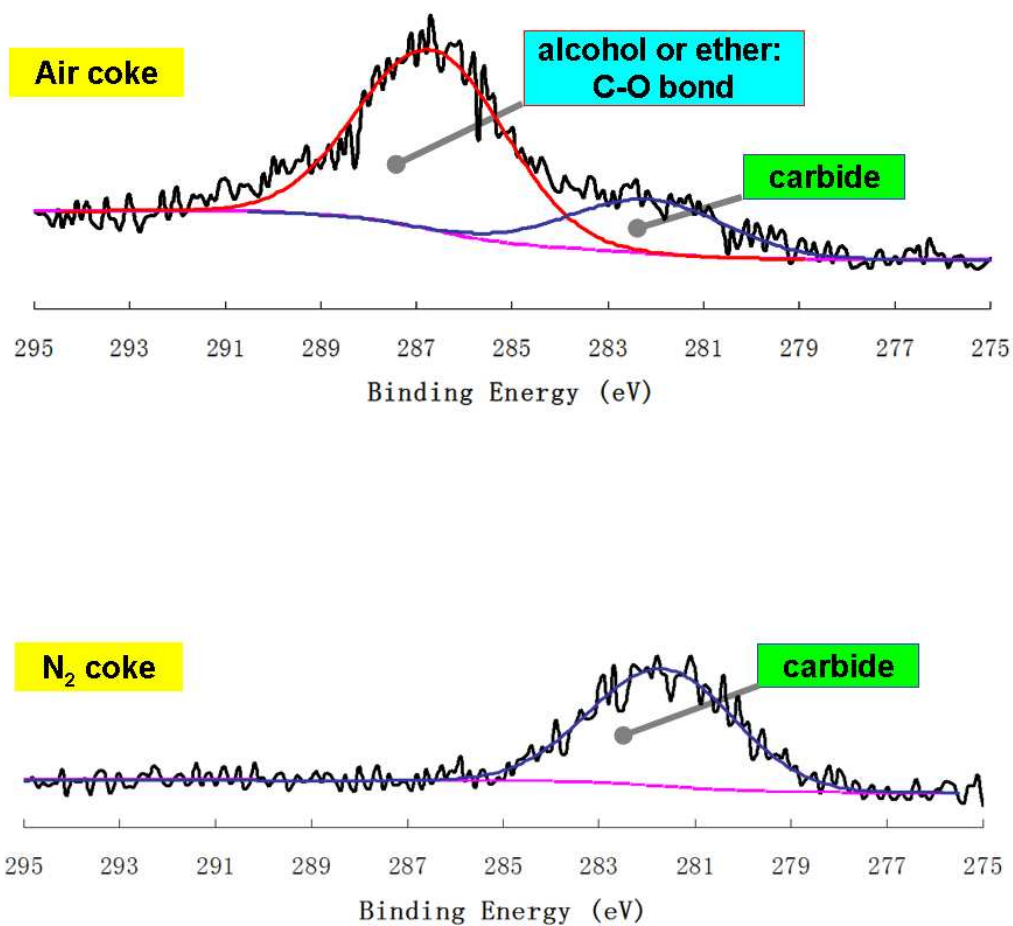


Figure 4.19: High resolution XPS C 1s spectra of coke samples precipitated under air and nitrogen flow conditions

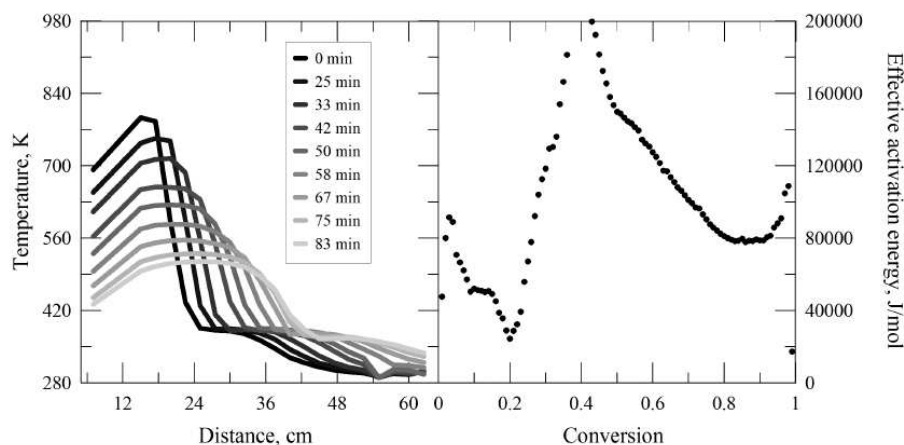


Figure 4.20: Unsuccessful combustion front propagation: (left) Combustion tube temperature profile and (right) isoconversional fingerprint [17].

make the in-situ combustion kinetic characters as the criterion to screen the crude oil candidate. As we know that the composition of the crude oil as well as the rock property determines the fuel deposition during the ISC process, and this criterion is well studied by analyzing the isoconversional fingerprint to make primary judgment whether the candidate is good or not.

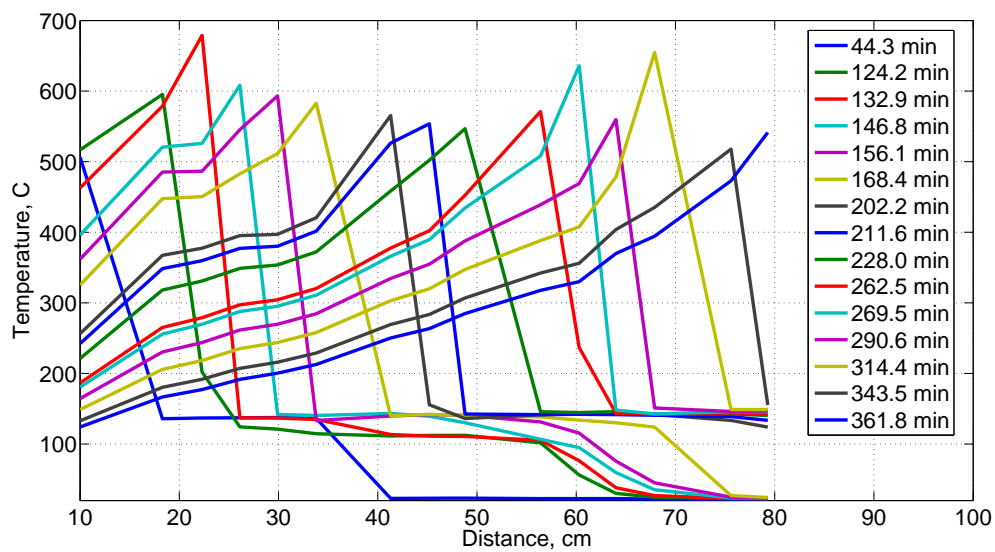
Previous research on basic screening for ISC candidates includes using TGA to measure kinetic parameters of crude oil combustion. Verkoczy et al. [105] developed screening criteria by processing the TGA results of eight primary and tertiary well-head oil samples. Another attempt comes from study by Yannimaras et al. [119]. They built the screening criterion by applying a specially modified accelerating-rate calorimeter (ARCTM) to gain reaction kinetic data for four crude oils of medium to high gravity. By applying the isoconversional principle, Cinar et al. [18][17] studied twelve crude-oil/sand-matrix pairs using RTO experiments with interpretation by the isoconversional principle to get the activation energy fingerprint. Poor ISC candidates represent very different isoconversional behavior from good candidates. On the fingerprint, an activation energy barrier is detected at the early stage of the combustion (Figure 4.20), while this energy barrier does not exist for the good candidate cases.

The isoconversional principle, as described in the previous chapter, processes temperature and effluent gas data from RTO experiments. The non-isothermal condition

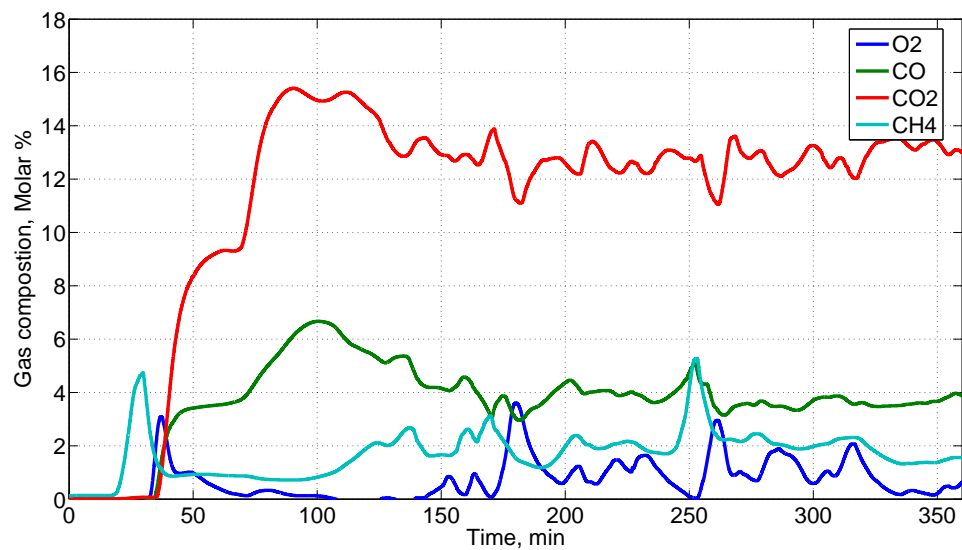
allows wider temperature measurement and thus the activation energy fingerprint represents the performance of the whole progress of the combustion. Also, as discussed before, the kinetic cell study well separates fluid flow dynamics from reaction dynamics. The fingerprint represent the apparent activation energy accounting for reaction paths influenced not only by component reaction itself, but also combines information from interaction between crude oil and rock matrix as well as interfere from phase equilibrium. So this fingerprint can be treated as a diagnostic tool to infer good candidates for an ISC process.

Isoconversional fingerprints are available for three cases: Alaska crude oil with 60 mesh sand and clay, Alaska crude oil with 60 mesh sand, and Karamay crude oil with the reservoir sand. As discussed in the Section 4.1, the three cases show typical reaction paths and no activation energy barrier is observed from the isoconversional fingerprints. The combustion tube tests for the three cases are run in the dry forward combustion mode. A heater is located near the top end of tube and thermocouples along the combustion tube record the position of temperature front.

The combustion tube results are shown in Figure 4.21, 4.22 and 4.23 respectively. When clay is mixed into the Alaskan crude oil sample (Figure 4.21), the combustion is more intensive with an average combustion front peak temperature of $560\text{ }^{\circ}\text{C}$, and CO_2/CO of 3.25. Without the clay addition (Figure 4.22), the combustion has lower front peak temperature which is $530\text{ }^{\circ}\text{C}$, and CO_2/CO of 2.4. For the Karamay crude oil with reservoir sand case in Figure 4.23, the peak front temperature is about $550\text{ }^{\circ}\text{C}$ and CO_2/CO is 6.3. The Karamay reservoir sand has clay in the mixture which enhances the combustion regarding the high propagation temperatures and the CO_2/CO ratio.

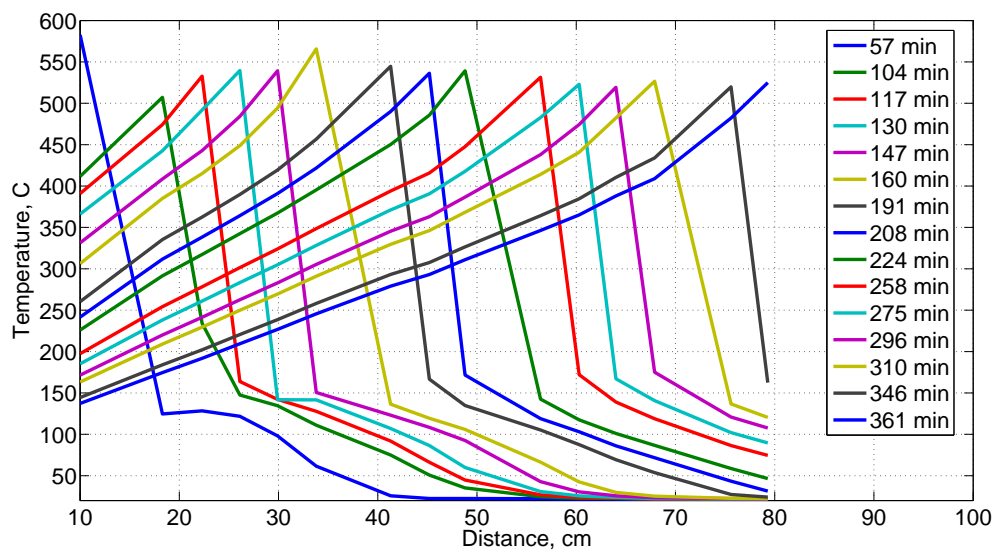


(a) Temperature propagation

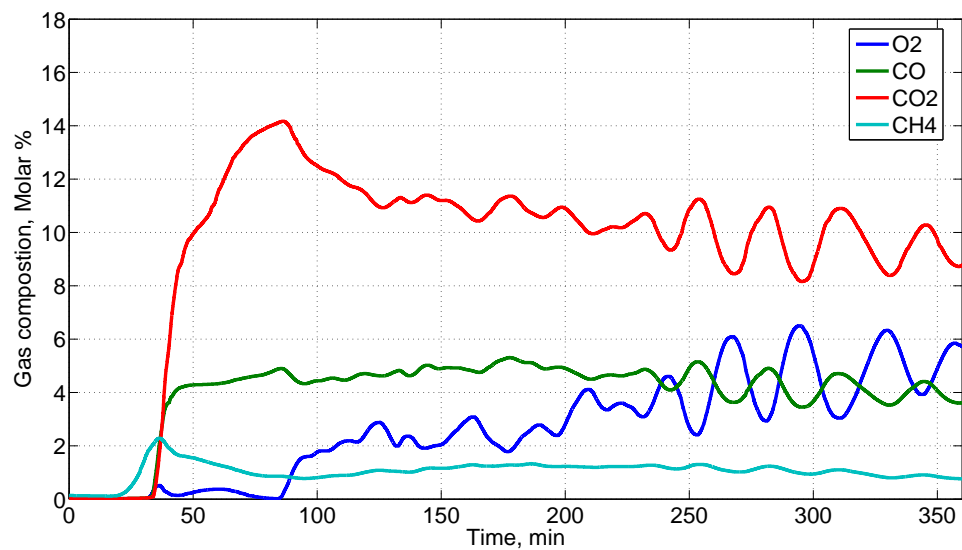


(b) Effluent gas histories

Figure 4.21: Alaska crude oil combustion tube test with 60 mesh sand and clay.

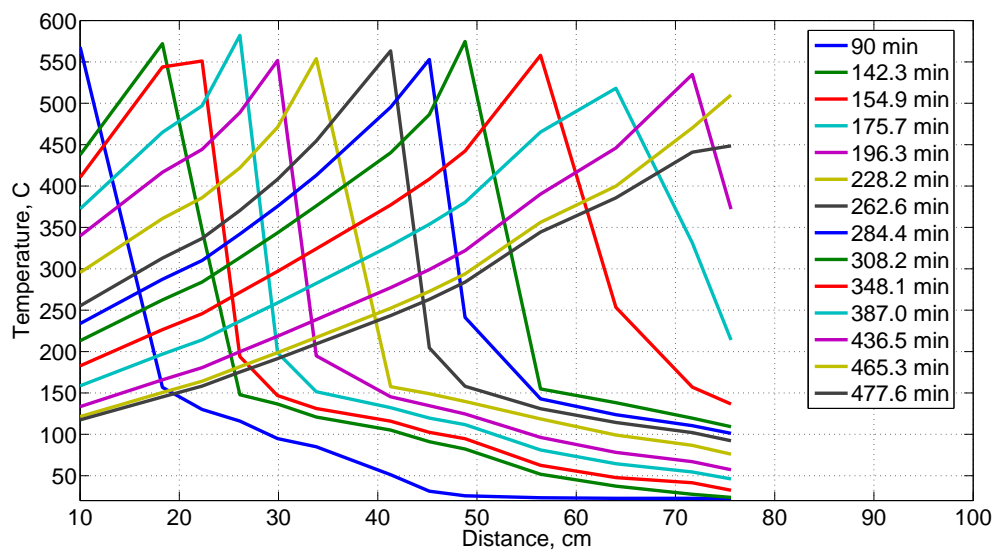


(a) Temperature propagation

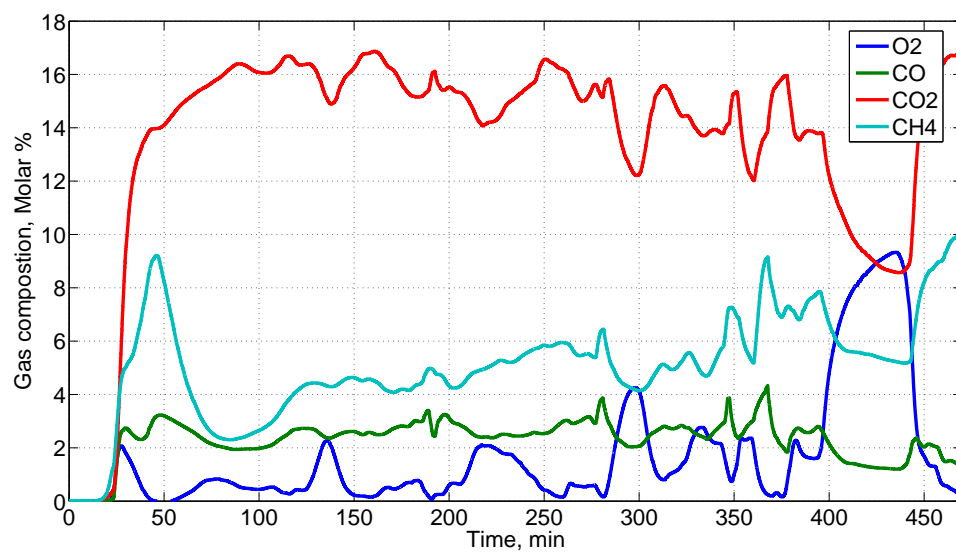


(b) Effluent gas histories

Figure 4.22: Alaska crude oil combustion tube test with 60 mesh sand.



(a) Temperature propagation



(b) Effluent gas histories

Figure 4.23: Karamay crude oil combustion tube test with reservoir sand.

Chapter 5

RTO kinetics using electromagnetic radiation

In-situ combustion is an effective thermal enhanced oil recovery (EOR) process that provides an important alternative to other EOR methods. Combustion reaction kinetics research is fundamental and essential to understand the high temperature combustion front propagation process within the reservoir so that the project operation is well controlled and the production is predictable. Conventional experimental tools to estimate kinetic parameters of crude-oil oxidation include accelerated rate calorimetry (ARC) [119] and thermogravimetric analysis (TGA) [60]. The interpretation of the measured data relies on the assumption of a reaction model, however, it may oversimplify the physics of crude-oil combustion. The isoconversional principle is an alternative to the conventional methods with its model-free character to estimate activation energy by interpreting effluent gas and temperature data from ramped temperature oxidation (RTO) experiments. Cinar et al. applied the isoconversional method to the analysis of RTO kinetic data of different crude-oil combustion experiments and reported great potential for deconvolving the parallel and series reactions characterizing ISC and screening potential candidates [14][15][16][17].

As discussed in the previous chapters, the isoconversional principle is applied to post-process temperature and effluent gas data from a series of RTO experiments of at least two heating rates. When considering the issue of data consistency, four or

more RTO experiments are needed to characterize linearity as discussed in Chapter 2. The RTO experiment within a kinetic cell system runs at a relatively low heat rate in order to reduce the temperature deviations as well as to well separate reaction stages. According to our former experiments, a heat rate less than 3 K/min is suggested. Considering a termination temperature of $650\text{ }^{\circ}\text{C}$, it may take four to seven hours to finish an experiment. Currently, the kinetic cell in the combustion lab is heated up by an electric furnace [17], that consists of a coil heater and thermal insulation paddings. Normally, the system takes overnight to allow the furnace to cool down to the ambient temperature before we can conduct new experiments. The efficient use of time is very low when we carry out four or more experiments to get the activation energy fingerprint. This motivates us to find an unconventional heating method in place of the electric furnace to heat up the kinetic cell. The electromagnetic heating has great potential to improve the kinetic cell system with respect to high efficiency in heating and cooling, parallel manipulation to process several experiments simultaneously, and a more compact system design.

Since the 1980's when the use of microwave radiation to heat chemical reactions began, thousands of publications have described this electromagnetic heating method applied in a broad range of science and engineering research, including drug discovery [56], analytical chemistry [66], organic synthesis [66], inorganic synthesis [66], food chemistry [76], materials science [44], enhanced oil recovery [13] and upgrading of oil shale [45]. Compared to conventional heating methods that depend highly on external heaters and in which energy is delivered by conduction, convection, or radiation, the benefits of microwave heating come from the direct coupling of an electromagnetic field with the sample to be heated. Accordingly, the heating efficiency is greater, the heating rate is faster, and homogeneous temperature distribution is obtained because of the deep penetration of microwave radiation.

There are two main microwave heating mechanisms [57] that are schematically plotted in Figure 5.1, dipolar polarization and ionic conduction. Both microwave heating mechanisms produce heating through molecular friction and dielectric loss. The dipole or ion field attempts to realign itself with the alternating electric field at microwave frequencies thereby attenuating electromagnetic energy. The ability of

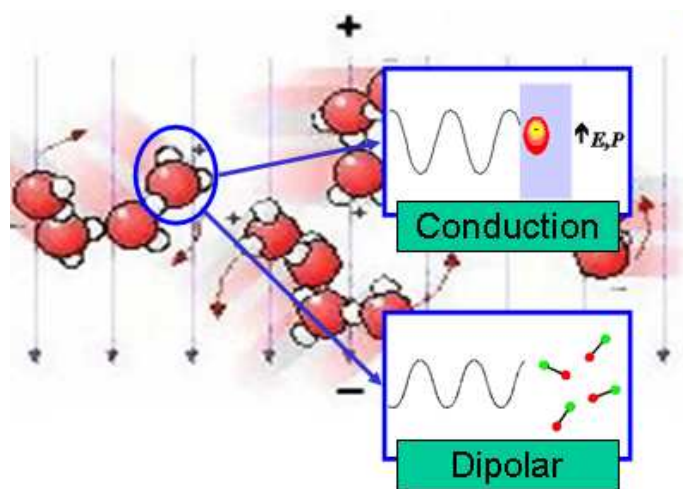


Figure 5.1: Schematic diagram of microwave heating mechanisms: dipolar polarization and ionic conduction [26].

a specific material to absorb microwave energy is determined by the so-called loss tangent, $\tan\delta$ [56][57]. Generally, high $\tan\delta$ materials are used for good absorption of microwave with the standard operating frequency, such as 2.45 GHz . Reaction vessels used in microwave assisted experiments are usually made out of microwave transparent materials such as glass or Teflon ($\tan\delta < 0.01$), so that only the reaction mixture rather than the reaction vessel is heated [57][83]. Because of direct coupling of microwaves with the sample, microwave heating presents a reverse temperature gradient to conventional heating, and it has the highest temperature in the center of samples. Both heating methods are demonstrated in Figure 5.2.

By applying RTO principles, combustion kinetics is studied in lab using a RTO kinetics cell. Currently, the kinetics cell is heated by an electric furnace that has a relatively large cavity and long heating and cooling cycles. The furnace is air cooled and usually more than a day is needed to let the system fall back to the ambient temperature before a new experiment can be started. Meanwhile, because of the large furnace size and the complicated system operation, it is hard to achieve parallel manipulation so that five or more simultaneous experiments with different heat rates are carried out for isoconversional interpretation. Introducing the microwave heating method to our oxidation kinetic experiments is attractive and has great potential in improving

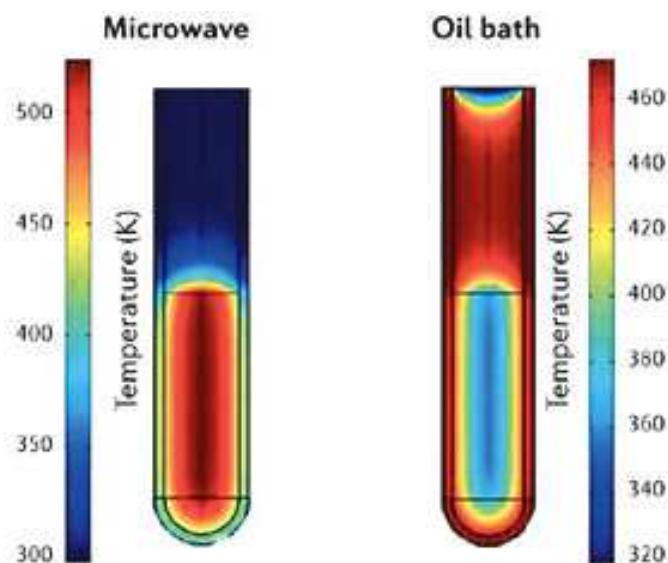


Figure 5.2: Temperature distribution difference between conventional and microwave heating [57].

data quality and quantity. Table 5.1 lists some typical aspects of microwave heating and furnace heating. As seen from the comparison in Table 5.1, microwave heating has advantages with respect to setup size, heating circle, and parallel experimental conditions. However, it does have some disadvantages in temperature measurement, system control, and setup cost. With the well developed microwave heating technologies nowadays, these disadvantages do not limit applications.

Before implementing microwave heating in our reaction kinetics experiments, we

Table 5.1: Comparison between microwave heating and furnace heating

	Microwave	(quantity)	Furnace	(quantity)
Instrument size	Small	Less than 2 <i>L</i>	Big	More than 10 <i>L</i>
Heating circle	Short	About 1 <i>hour</i>	Long	More than 1 <i>day</i>
Precise control	Difficult	–	Easy	–
T measurement	Difficult	–	Easy	–
Parallel manipulation	Easy	–	Difficult	–
System cost	High	More than \$20,000	Low	About \$1,200

have to consider various aspects: non-thermal effects of microwave radiation kinetics, temperature measurement in an electromagnetic environment, reactor design, heat loss from the reactor wall to the environment, oxidation gas supply to the reactor, effluent output and analysis, power control, and so on. These issues have been well studied through literature review and preliminary experiments.

5.1 Literature review

5.1.1 Microwave heating effect

In a microwave heating process, microwave interacts with a dielectric media and the electromagnetic energy is converted into heat inside the sample. This is in contrast to conventional heating where heat transfers from the sample surface towards the center mainly by heat conduction. In general, the temperature inside the sample within a conventional furnace is lower than that at the surface because heat has to be transported from the surface to the interior. In the case of microwave heating, the radiation energy is dissipated within the sample more or less uniformly and a much greater heating rate is obtained. As a result, a significant temperature gradient can also exist but with the inside hotter than the surface [123].

The average power, P_{abs} , dissipated in a dielectric of volume V is related to the electric field E and the material dielectric properties by Eq. 5.1 [69]:

$$P_{abs} = 2\pi f \epsilon_0 \epsilon_{eff}'' E_{rms}^2 V \quad (5.1)$$

where f is the frequency of the radiation, ϵ_0 is the permittivity of free space, and ϵ_{eff}'' is the complex component of the relative permittivity of the dielectric, also known as the effective relative dielectric loss factor, and E_{rms} is the root mean square of the electric field E . Eq. 5.1 represents the relation between the volumetric absorption of microwave power and the electromagnetic field for a given dielectric. In microwave heating, microwaves only penetrate a limited distance below the sample surface and this is represented by the penetration depth D_p [69]:

$$D_p = \frac{\lambda_0}{2\pi} \frac{\sqrt{\epsilon'}}{\epsilon''} \quad (5.2)$$

where λ_0 is the wavelength of the microwave radiation, $\sqrt{\epsilon'}$ is the dielectric constant that describes the ability of a molecule to be polarized by the electric field, and ϵ'' is the dielectric loss which measures the efficiency to convert the electromagnetic radiation into heat.

It can be seen from both Eq. 5.1 and 5.2 that the amount of microwave power absorbed by the dielectric is dependent on the electromagnetic field applied and on the dielectric property of the material heated. In a simple way, the ratio of the dielectric loss and the dielectric constant is commonly used to measure the ability of a material to convert microwave radiation into heat energy at a given frequency and temperature, and this is referred to as the loss tangent:

$$\tan\delta = \frac{\sqrt{\epsilon''}}{\epsilon'} \quad (5.3)$$

This suggests that under the same microwave heating conditions, some materials are more capable than others of absorbing microwave radiation because of their greater dielectric loss property. Passive heating elements, for example silicon carbide or graphite-doped Teflon, have big loss tangent and are widely applied to material processing that requires very high heat rates and high temperature conditions [57]. The Arrhenius expression for rate constant in Eq. 2.4 claims the increased reaction rate constant as temperature increases. The rapid heating experienced in microwave-assisted transformations may lead to altered product distributions, for instance fewer by-products are generated comparing to a conventional oil bath reflux experiment. These observed rate-accelerations and altered product distributions of microwave reactions compared to traditional heating experiments have led to debates on the existence of so-called "specific" or "non-thermal" microwave effects [57]. Pillai et al. [82] conducted comparison experiments between conventional and microwave heating hydrodechlorination reaction. An expeditious hydrodechlorination of chlorobenzenes is observed over 0.5% Pd/Al_2O_3 catalyst by conducting the reaction under microwave irradiation conditions. Djenni et al. [24] investigated microwave selective heating

phenomena and their impact on heterogeneous chemical reactions. They discussed the non-thermal effect of microwaves and claimed that direct molecular activation of microwaves should be excluded, because the energy used to ionize biological compounds (13.6 eV) is much higher than microwave energy ($1.24 \times 10^{-6} - 1.24 \times 10^{-3}\text{ eV}$). They also developed a model to predict reaction kinetics and yields under microwave heating based on the Arrhenius equation, and the model was in good agreement with experimental data and procedures. In the majority of published cases, the reasons for the observed rate enhancements and altered product distributions can probably be attributed to the high reaction temperatures that can rapidly be attained when processing heating in a microwave field. Silverwood et al. [95] compared experiments of conventional and microwave heating for the oxidation of carbon monoxide over a 6.3% Pt/SiO_2 catalyst (EUROPT-1). The microwave source used was a 2.45 GHz generator up to 1 kW . The results showed both heating methods displayed similar activities.

5.1.2 Temperature measurement

Temperature measurement inside a microwave cavity is very different as compared to that in conventional heating systems, such as isomantles, oil baths, and hot plates/wires [57]. In a microwave environment, temperature sensors are specially designed to avoid influence or damage by electromagnetic waves. Temperature measurement techniques can be classified into contact and non-contact modes. Thermocouples, resistance temperature detectors (RTDs), and thermistors are the most prevalent and low cost contact sensors. Fiber optic probes are accurate, but expensive temperature measuring units. An infrared thermometer, which is a non-contact sensor, measures infrared energy emitted by the materials. It is usually faster than the contact sensors. Besides in place temperature determination, infrared thermal imaging cameras are useful to capture temperature distribution on the sample surface [80].

During the first years of microwave assisted heating research, temperature measurement was often neglected for lack of suitable means [42]. The experimental results

were compared with data in publications. Such comparison leads to incorrect estimation of the capability of microwave radiation because of the significant difference in temperature distribution between conventional heating and microwave heating as found in later research.

A thermocouple is a thermoelectric temperature sensor consisting of two dissimilar metallic wires coupled at the probe tip (measurement junction) and extended to the reference (known temperature) junction. The temperature difference between the probe tip and the reference junction is detected by measuring the change in voltage at the reference junction. Commercially available thermocouples have a metallic body enclosing the sensor wires as insulation and protection. Using a thermocouple to measure temperature within a microwave cavity when the magnetron is on causes electrical arcing that damages the thermocouple. So early researchers turned off the magnetron and then inserted a thermocouple to measure temperature. The magnetron was then restarted and the procedure repeated. Artificial error was introduced by this approach that was corrected by some adjustments. For example, Perry et al. [80] used a normal thermocouple to gain temperature values by inserting it through a thin quartz tube into the heating sample patch bed after the microwave power was turned off. Because of the error introduced by turning off the energy source, the temperature decay curve was recorded on a strip chart recorder, and temperature versus time curve was linearized by taking the natural log of the data and extrapolated to zero time to determine operating bed temperature

A thermocouple encased in an electromagnetic sheath is currently the least expensive method for temperature measurement in a microwave condition. The thermocouple inside the sheath must be of the ungrounded tip variety, while grounding of the metallic sheath to the cavity is required to avoid arcing. Shielding the thermocouple circuit from the high voltage present in the microwave circuit required considerable effort. It was possible to reduce interference to within the thermocouple resolution ($\pm 1.5^\circ\text{C}$). General guidelines in this regard are to use shielded extension cables that should be grounded to the thermocouple amplifier circuitry and to remove such circuitry as far as possible from the high voltage area. The amplifier circuitry also needs to be designed to exclude electromagnetic interference from the high voltage

circuit [9]. It is reported that a type S shielded thermocouple with platinum foil and inert gas inlet can measure temperature up to 1700 °C in microwave sintering ceramic process [29]. Furthermore, because shielded thermocouples have significant volume due to the shielding, reaction volume should have a minimum size of approximately 30 ml [74]. Ripley [87] reported a patent on a very simple shielded thermocouple and its embodiments. The thermocouple shield includes an electrically conductive tube that protects the standard thermocouple from damage by microwave field and a ceramic sheath in between the thermocouple and the conductive tube serves as electrical insulation.

Fiber optic sensors are currently widespread but they are a relatively costly method for temperature measurement. With this method, a fiber optic sensor with gallium arsenide crystal on the tip is placed inside a protective tube directly into the reaction mixture. One disadvantage compared to other measurement systems is the more narrow operating range, usually of 0 to 300 °C. Also they are very sensitive to mechanical stress. Zhang et al. used a fiber optic sensor which had its tip at the center of the catalyst sample to monitor the temperature in the microwave condition. It is reported that sensor could in-situ measure temperature up to 1000 °C [121].

Infrared (IR) sensor is another widespread method which is noncontact and is usually used to measure surface temperature. The sensors are integrated into the wall of the microwave cavity and measurements are made from a certain distance. The disadvantage of this method is that only the temperature of the outside wall of the reactor is measured. In some experiments, sample surface temperature and center temperature are gained simultaneously with IR sensor and a thermocouple or fiber optic sensor, respectively, for comparison or feed back power controlling purposes [64].

5.1.3 Microwave heating system

Besides temperature measurement, a whole microwave heating system usually consists of a reactor, which is a key component in microwave assisted research, microwave generator, such as a magnetron, power tuning to adjust the heating rate, reaction processing visualizing and wave guiding techniques to conduct an easily manipulated

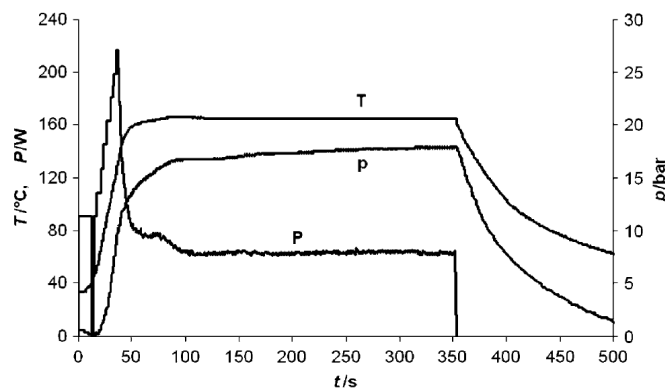


Figure 5.3: Temperature (T), pressure (p), and power (P) profile for a 3 *mL* sample of methanol heated under sealed vessel single-mode microwave irradiation conditions to 165°C (external infrared temperature monitoring) [57].

experiment.

Early pioneering experiments based on microwave assistance have been carried out in domestic microwave ovens. Since 2001, specifically designed dedicated microwave reactors have been increasingly employed. These instruments feature built-in magnetic stirrers, direct temperature control of the reaction mixture with the aid of internal fiber-optic probes or external infrared sensors, and software that enables on-line temperature/pressure control by regulation of microwave power output. Since the introduction of dedicated microwave reactors suitable for sealed vessel processing in the year 2000, more than 2500 publications have described the use of such equipment for carrying out a large variety of microwave assisted research [63] [3]. A variety of microwave reactors and processing options are available today, and more than 90% of all currently published microwave protocols involving dedicated instruments that rely on the use of so-called single-mode microwave reactors in combination with sealed vessel processing. The temperature, power, and pressure profiles for a sample of microwave-heated methanol shown in Figure 5.3 illustrate the operating principles of a modern dedicated microwave reactor run in temperature control mode [57].

5.2 Development of microwave heating systems

This section exhibits the development of three generations of microwave heating system in the combustion lab. Preliminary tests on the systems as well as problems are discussed. Meanwhile the proposal manipulations for parallel experiments are included.

5.2.1 1st generation reactor and embodiments

The 1st generation microwave heating system is the first attempt to build up a prototype. A household microwave oven of 700 W output power and 10 levels of power control is used. The kinetic cell is made of a specially designed quartz tube that has a large lip at the open end to aid the formation of a pressure-tight seal. The quartz cell can stand temperatures of 1800 °C. A well machined metallic cap is used to seal the open end of the tube and to hold the reactor in the center of the oven cavity. A thermocouple is inserted through the metallic cap into the center of the quartz tube to measure the in-situ reaction temperature. Another two holes on the top of the cap serve as air injection and effluent conducting parts. This preliminary experimental system is demonstrated in Figures 5.4 and 5.5.

Initially, we believed that microwaves from the magnetron would couple efficiently with the crude-oil sample inside the quartz tube. In actual fact, there is no heat source around the tube, as temperature increases, heat losses become larger and larger and steady state may be achieved before our expected maximum temperature. Insulation is used to reduce the heat loss from the tube to the cavity. Thermolastic insulation is used and its properties are described by Marques et al. [67]. Figure 5.6 show the insulation material and its embodiment around the quartz tube reactor.

Some basic tests showed that the dielectric properties of typical crude oils were not sufficient to reach high temperature. In the best case, crude oils can only be heated to 480 °C. Our experiments need to achieve a termination temperature up to 700 °C. The loss tangent of sintered SiC is 0.6 to 0.7 [61], and SiC is classified as a high microwave energy absorber. Small cylinders of sintered SiC are added directly to the sample to assist the absorption of microwave. The cylinders have a dimension



Figure 5.4: Prototype of the 1st generation microwave heating system. The quartz tube reactor is hung inside the microwave oven cavity.

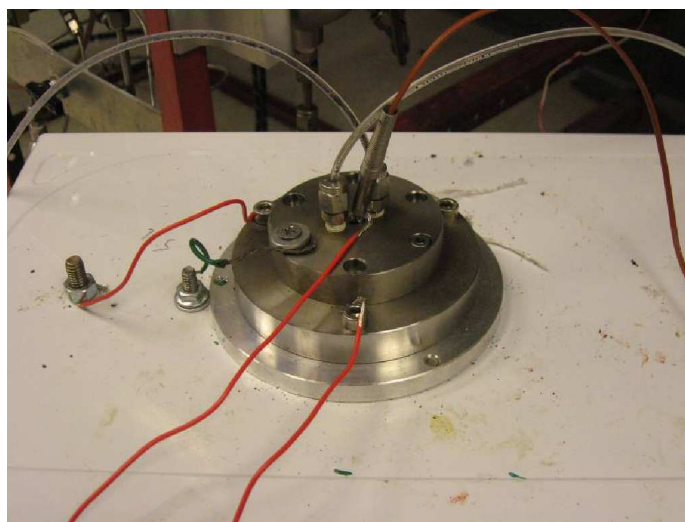


Figure 5.5: Metallic cap on the top of the microwave oven. A thermocouple is inserted through the cap. There are two connectors for injection and production gas respectively. The cap needs to be well grounded.

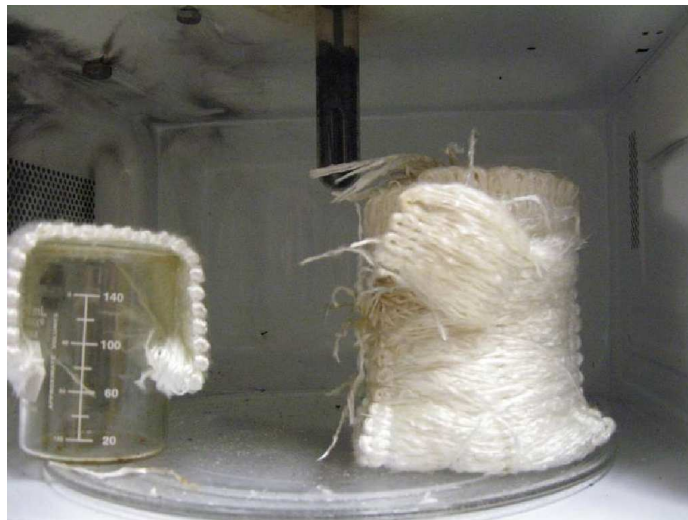


Figure 5.6: Insulation material and its embodiment around the quartz tube reactor: during an experiment, crude oil sample is put at the bottom of the quartz cell. The body of the tube is wrapped by insulation material that is transparent to microwave, reducing heat loss to the oven cavity.



Figure 5.7: Shielded thermocouple and sintered SiC cylinders: sintered SiC cylinders are mixed with crude oil sample, acting as energy absorber to assist fast heating.

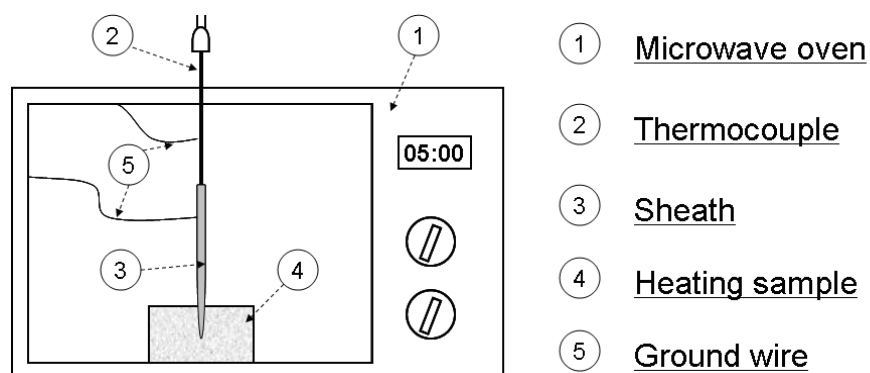


Figure 5.8: Schematic diagram of grounded circuit of a shield thermocouple.

of 5 *mm* in diameter and 10 *mm* in length. The number of SiC cylinders is varied according to the desired heating rate of the experiments (Figure 5.7).

Temperature measurement is a critical issue as described in the literature review. Fiber optic sensors have been widely used in microwave heating experiments. They are costly, and especially for measurement up to 800 °C. A shielded metallic thermocouple is used and it has worked very well for our experimental conditions. The sheath consists of a stainless steel tube that blocks the direct coupling of microwave with the metallic tip of the thermocouple. A ceramic tube is assembled in between the thermocouple and the stainless steel tube and it plays the role as electric insulation to avoid electrical arcing. Because of the metallic body of the thermocouple as well as the sheath, a thermocouple and the stainless steel protection function as a microwave antenna to conduct microwaves out of the cavity and cause hazards. The bodies of the thermocouple and the protection tube are well grounded to the interior wall of the microwave cavity. Microwaves are conducted back to the cavity rather than transported outwards. The simple assembly of the thermocouple and its embodiment in a microwave oven are displayed in Figure 5.7 and 5.8, respectively.

Two preliminary experiments were carried out to test the 1st generation system and provide proof of concept. The test includes sealing the open end of the quartz tube at elevated pressure up to 40 *psi*, measuring temperature with the shielded thermocouple, injecting air, analyzing effluent gas with a gas analyzer, changing heating rate with the various numbers of cylinders of sintered SiC, and presetting induced

Table 5.2: Experimental conditions

	Microwave	(quantity)	Furnace	(quantity)	
Experiment 1	40	6	40%	500	Air
Experiment 2	14.5	3 1	30%	2500	N/A

power of the microwave oven. The experimental conditions are listed in Table 5.2.

Effluent gas results and temperature histories of the first experiment are shown in Figure 5.9 and 5.10 respectively. From experiment 1, we find that when the temperature reached about 400 °C, crude-oil cracking happened in which molecular bonds are broken directly because of the heat. Methane was produced as a result [1]. With temperature increasing, CO and CO_2 fractions increase because of the termination reactions (i.e. bond scission). When the temperature is above 600 °C, the reaction stops because of the entire consumption of the crude oil within the quartz reactor. This experiment used six pieces of SiC cylinders as the heating element mixed with the crude-oil sample and set the power level as 40% of the full power. We achieved a temperature as high as 600 °C in about 500 seconds.

The second experiment is conducted to test the variability of heating rate by changing the number of SiC cylinders and the power level of the microwave oven. Three SiC cylinders are added to the crude oil sample and 30% of the power level is preset. We expect a lower heating rate in this experiment and the result shows a maximum temperature of 600 °C achieved in about 2500 seconds.

Also, some comments are in order about the power control of the microwave oven. When the oven is running at full power, the magnetron is working continuously. Once the power is set to be a certain level below 100%, the magnetron runs in an on/off mode in which the time portion is defined by the desired power level. So we can expect a stair-step shape of the temperature profiles versus time.

5.2.2 2nd generation reactor and embodiments

The 2nd generation reactor is designed to overcome some limitations of the 1st generation reactor. The schematic design of the new reactor is shown in Figure 5.12.

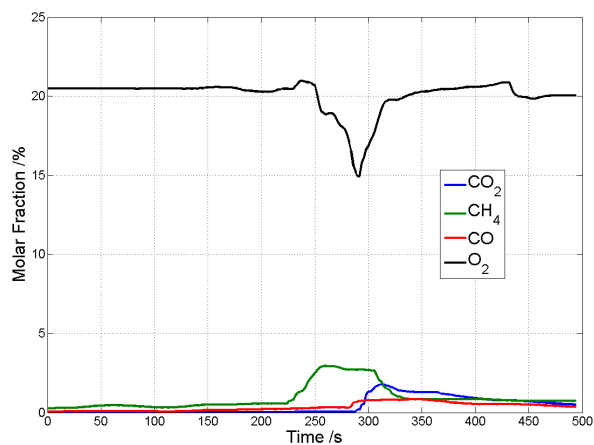


Figure 5.9: Experiment 1: effluent gas histories, 1st generation system.

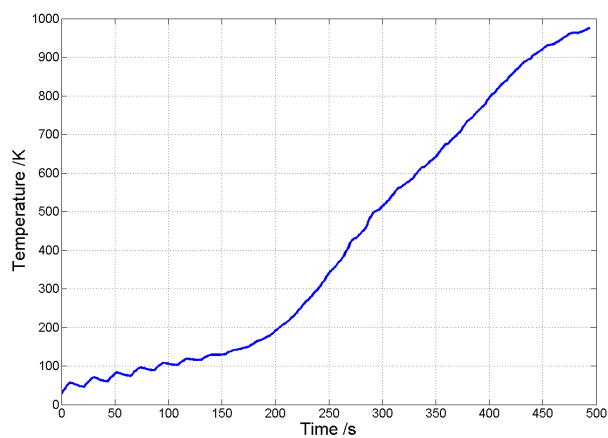


Figure 5.10: Experiment 1: temperature profile, 1st generation system.

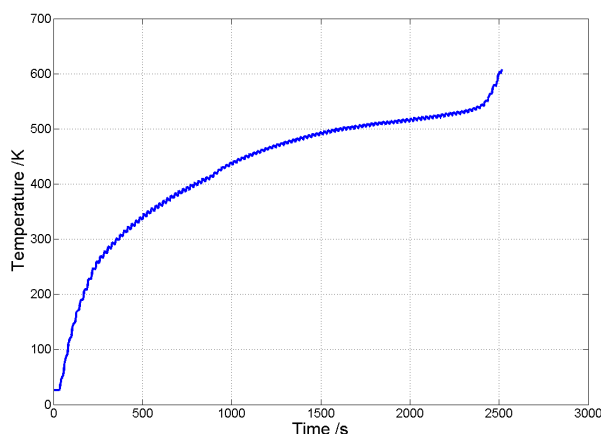


Figure 5.11: Experiment 2: temperature profile, 1st generation system.

The thermocouple is a shielded thermocouple whose sheath is grounded to the inside wall of the microwave cavity through the metal cap. Also, a channel on the top of the cap conducts effluent gas to the gas analyzer. The quartz tube is divided into two parts, and the lower part is filled with sand that disperses the injected air and the middle part that holds the crude-oil sample. The thermocouple is inserted through the metal cap into the center of the sample. An annular encasement holding sintered SiC particles is wrapped around the bore of the quartz reactor. It plays the role of energy absorber to heat up crude oil samples and to preheat the feed gas. Air is fed through the bottom fitting of the reactor and is stirred by the sand inside the tube. The gas is preheated to the same temperature as that of sample before it has reaction with the sample.

The reactor is easily adjustable for different embodiments. Figure 5.13 shows the embodiment based on a household microwave oven. We control the heating rate by controlling the built-in power tuner or the mass of SiC absorber.

A prototype of the 2nd generation reactor is built according to the design in Figure 5.12. The reactor is embodied into a household microwave oven. The reactor and the system are shown in Figure 5.14 to 5.17. The main body of the reactor is a quartz tube of 1 inch in diameter and 7 inches in length. Both open ends of the tube are sealed by Swagelok fittings with Teflon ferrules. One end the gas injection tubing is

connected, and the other end has a channel to insert a shielded thermocouple and a connector to the products filter (Figure 5.14). The bottom part of the tube is filled with fine sand to disperse the injection gas. The crude oil sample is mixed with small cylinders of sintered SiC and fills the middle part of the quartz tube. The whole reactor is hung inside the cavity of a household microwave oven (Figure 5.15). The injection tubing connected with the bottom fitting is well grounded to the interior wall of the cavity. An insulating ceramic tube is inserted into the channel first and then a normal thermocouple with an ungrounded tip. The ceramic tube protects the thermocouple from being destroyed by electrical arcing (Figure 5.16). The microwave heating system is connected with the air mass flow meter and the product filter (Figure 5.17).

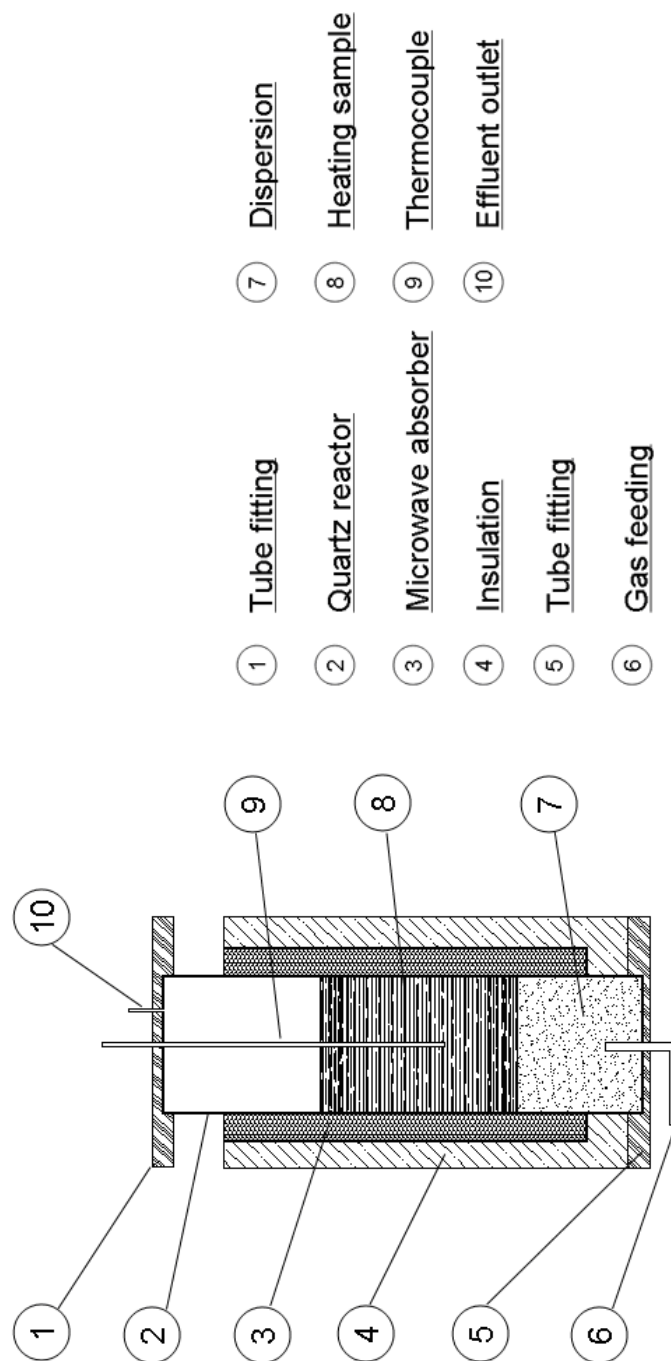


Figure 5.12: Schematic design of the 2nd generation reactor.

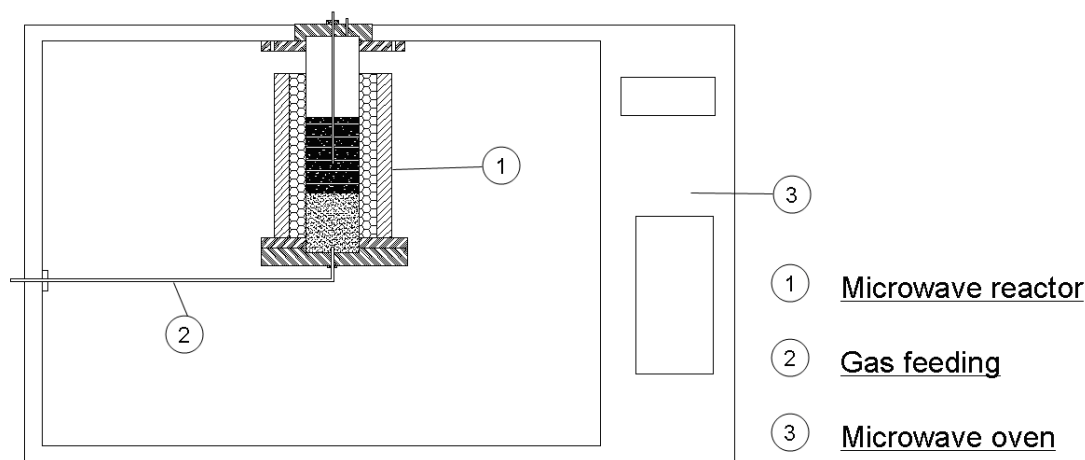


Figure 5.13: The reactor embodiment based on a microwave oven.

5.2.3 3rd generation reactor and embodiments

Based on our preliminary tests on the 2nd generation system, several drawbacks are observed. The first is that it is hard to carry out experiments at high pressure condition because of the quartz tube fittings. The quartz tube is very fragile, but we need to fasten the fitting tightly enough to stand high pressure condition. Excessive tightening breaks the quartz tube. The second drawback is to preheat the inlet gas. In-order to heat up the gas at the same temperature as that in the oil sample, extra equipment such as electrical coil or furnace and temperature feedback and controlling system are needed, which will make the system larger and more complicated. The third drawback is that it is very difficult to remove the quartz tube from the microwave cavity because of the fittings at both ends of the quartz tube. If we want to take the sample out of the cavity while the temperature is still high, it is impossible to do that because sands will leak through the bottom of the tube.

We designed the 3rd generation system which we believe overcomes the shortcomings of the 2nd generation system. The schematic design of the system is shown in Figure 5.18. There are two tubes in the design. The outer tube is the sintered SiC tube that absorbs microwave energy to generate high temperature, and the interior tube is the quartz tube that is filled by sands at the bottom and oil sample in the

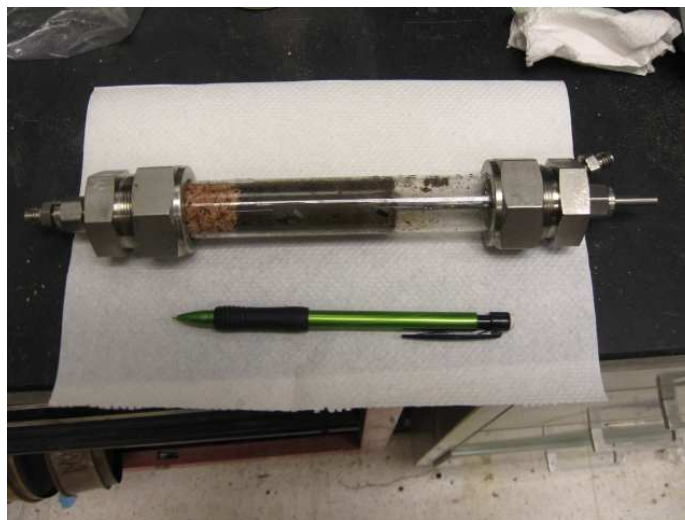


Figure 5.14: The prototype of the 2nd generation microwave reactor.



Figure 5.15: The embodiment in a household microwave oven.

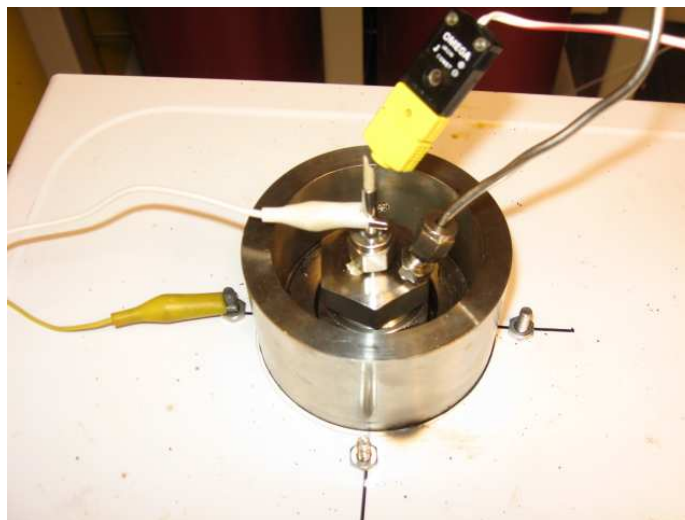


Figure 5.16: Shielded thermocouple and product filter connector.



Figure 5.17: 2nd generation microwave heating system.

middle. Between the SiC and the quartz tube, there is room to circulate the inlet gas like air or nitrogen. The sealing metallic cap consists of three pieces, the bottom, and middle and the top pieces. There is a gas inlet connector on the middle piece. The inlet gas is conducted through the connection, travels through the room between the quartz tube and the SiC tube, and then passes the hole at the bottom of the quartz tube to mix with the oil sample. In this way, the inlet gas is preheated by the SiC tube before it is mixed with the sample. Meanwhile, the heat is brought to the sample by conduction, convection and radiation, that keeps the temperature difference between the oil sample and inlet gas as small as possible. On the top piece, a thermal well that protects the thermocouple is placed. There is a connection to conduct the effluent gas to the gas analyzer on this piece as well.

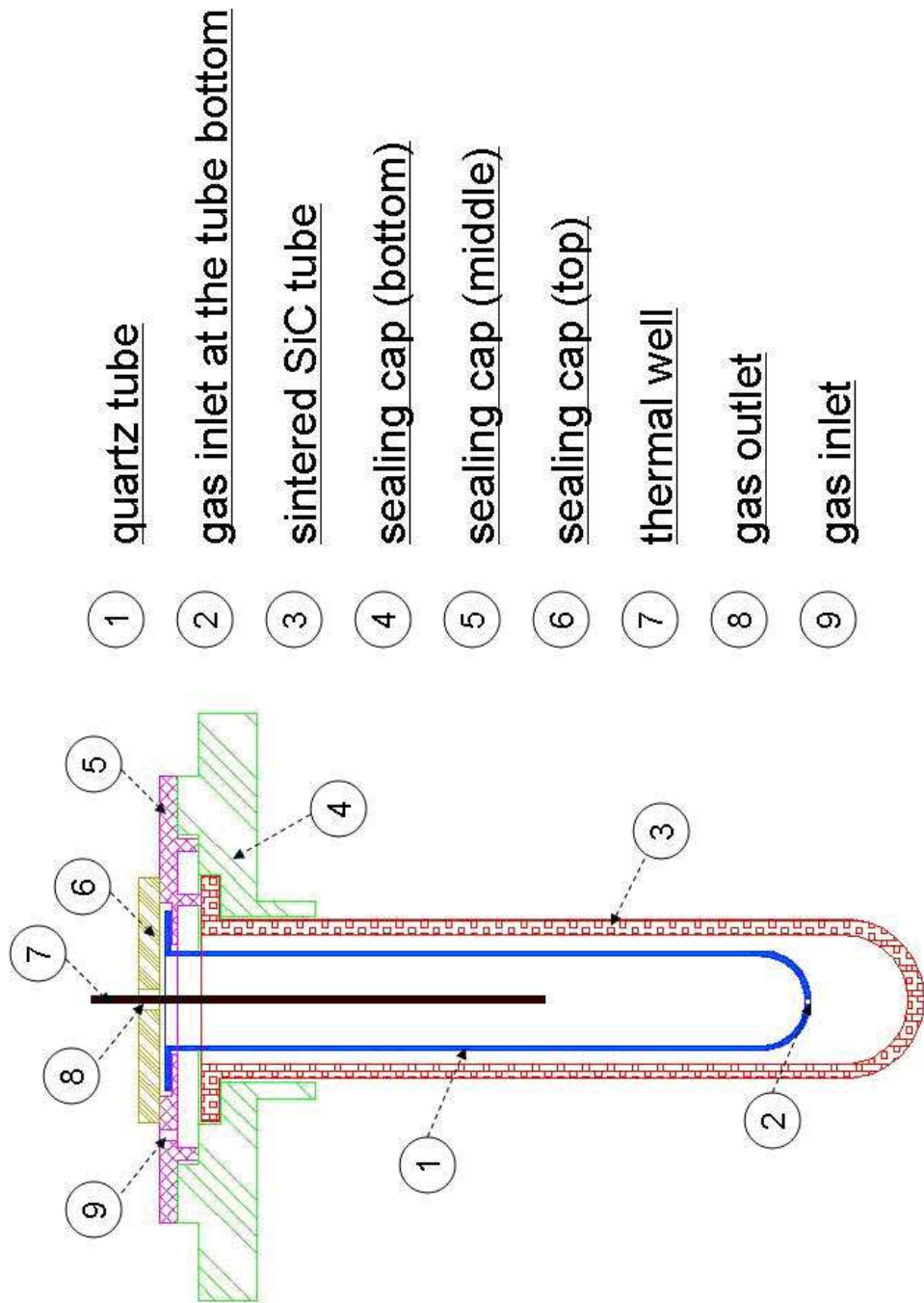


Figure 5.18: Schematic design of the 3rd generation reactor.



Figure 5.19: The prototype of the 3rd generation microwave reactor.

A prototype of the 3rd generation reactor is built according to the design in Fig. 5.19. The reactor is embodied into a household microwave oven. The reactor and the system are shown in Fig. 5.20 and 5.21. The main body of the reactor consists of a sintered SiC tube of 1.6 inches in diameter and 7.2 inches in length and a quartz tube of 1 inch in diameter and 6.5 inches in length. On one end of the quartz tube, there is a large lip for sealing and the other end of the tube is there a small hole of 0.1 inches in diameter for gas crossing. The whole reactor is hung inside the cavity of a household microwave oven. The microwave heating system is connected with the oxidation gas tank and the product filter (Figure 5.22).

The first experiment ran on the full power model of 700 W for about 15 minutes. The quartz tube was filled by fine sands and air was injection by the rate of 1 L/min. The pressure inside the kinetic cell is ambient. An insulating material, fiberglass [67], was wrapped around the body of the sintered SiC tube to reduce heat losses to the cavity. We see fast heat rate at the early stage and lower heat rate after 600 seconds because of the heat lost. The maximum temperature was around 300 °C in this case.

The second experiment ran on the same conditions as the first one except for the insulating material. Black aerogel [67] that has much better insulation effect was used in this case. A higher maximum temperature of about 530 °C was gained



Figure 5.20: The embodiment in a household microwave oven, sintered SiC tube.

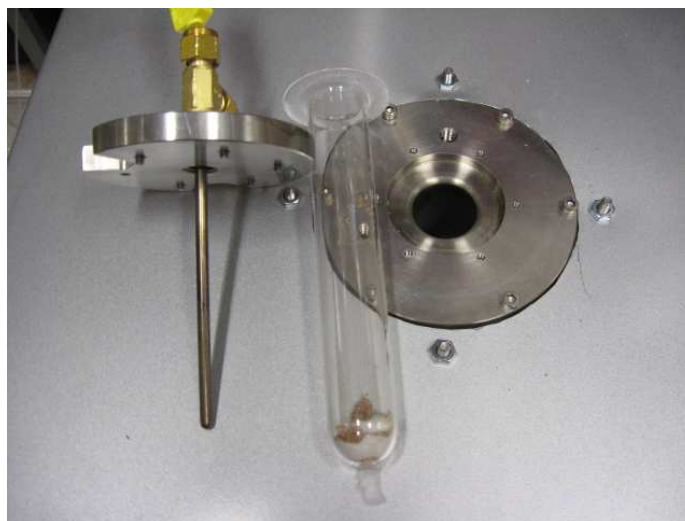


Figure 5.21: The embodiment in a household microwave oven, sealing cap and quartz tube.

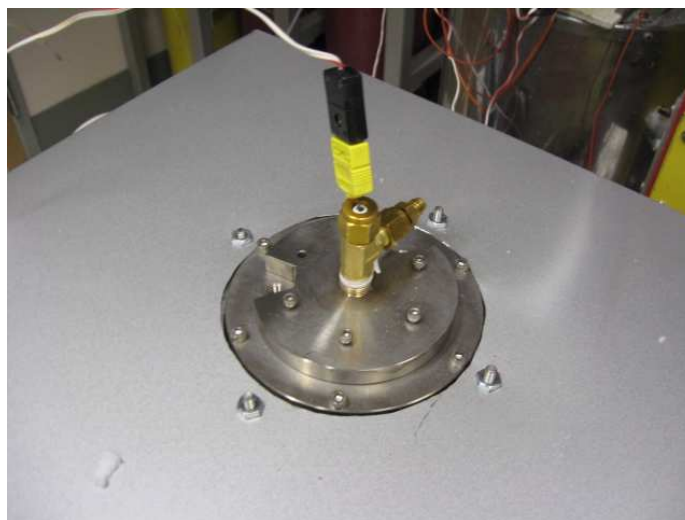


Figure 5.22: thermocouple and product filter connector.

after the system ran for about 2500 seconds. The temperature approached a plateau and it did not reach the expected temperature of $600\text{ }^{\circ}\text{C}$ in both cases. These results suggest clearly that heat losses are significant later in the test and we need to improve insulation material to keep fast heat rate when the temperature goes up.

5.2.4 Parallel electromagnetic heating system

Parallel manipulation of RTO experiments is the most attractive advantage while applying electromagnetic heating. The parallel system can be achieved by embodying several well-designed microwave reactors in a microwave oven and using different amount of sinter SiC to control energy absorption. Another way is to use waveguide technique. Figure 5.25 shows another embodiment based on a specially made microwave cavity (single mode or multi-mode) and waveguides conducting wave energy from a magnetron. Several reactors will be fixed in separate cavities and the induced power will be controlled by attenuators on the waveguide.

Besides microwave heating, induction heating is also considered to apply to the kinetic reactor [5]. The induction heating is the process of heating an electrically conducting object (usually a metal) by electromagnetic induction. A schematic design of a induction system is shown in Figure 5.26. The basic components of an induction

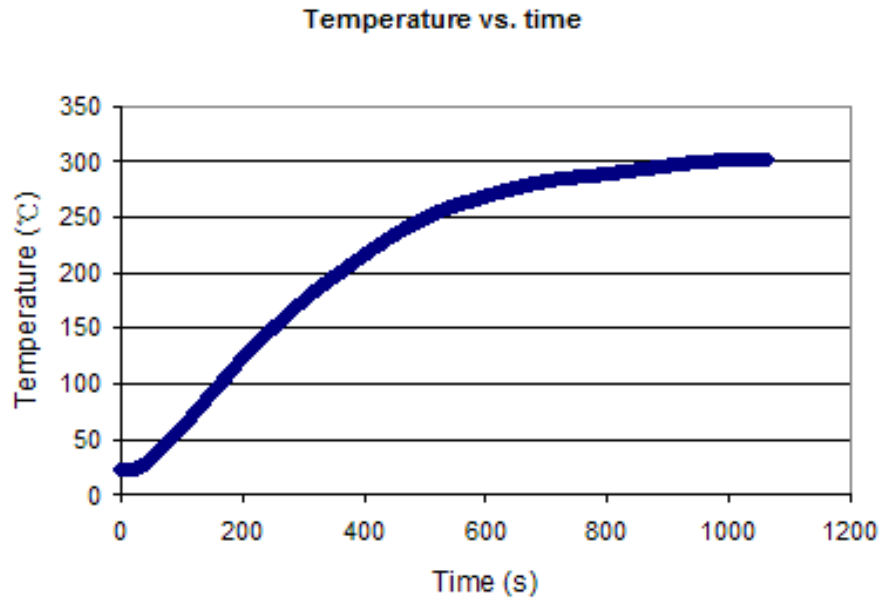


Figure 5.23: Temperature profile of microwave heating of test 1, 3rd generation system.

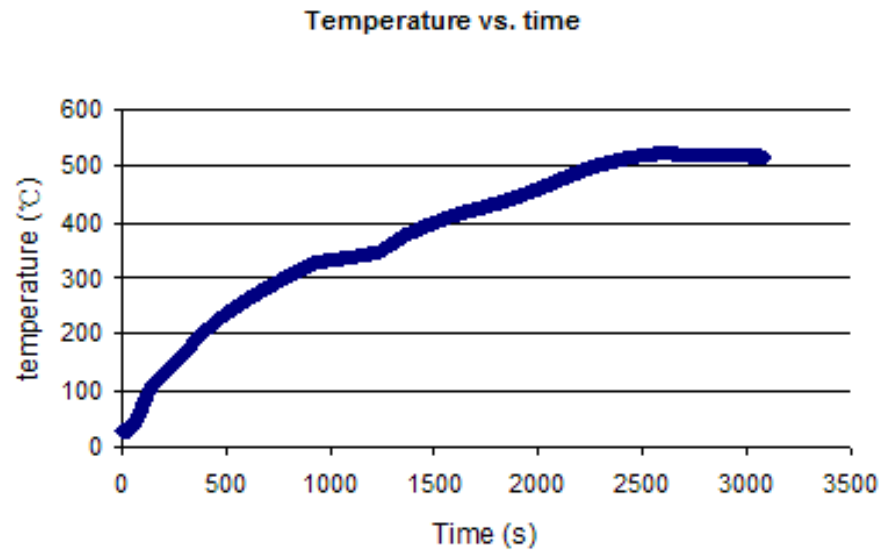


Figure 5.24: Temperature profile of microwave heating of test 2, 3rd generation system.

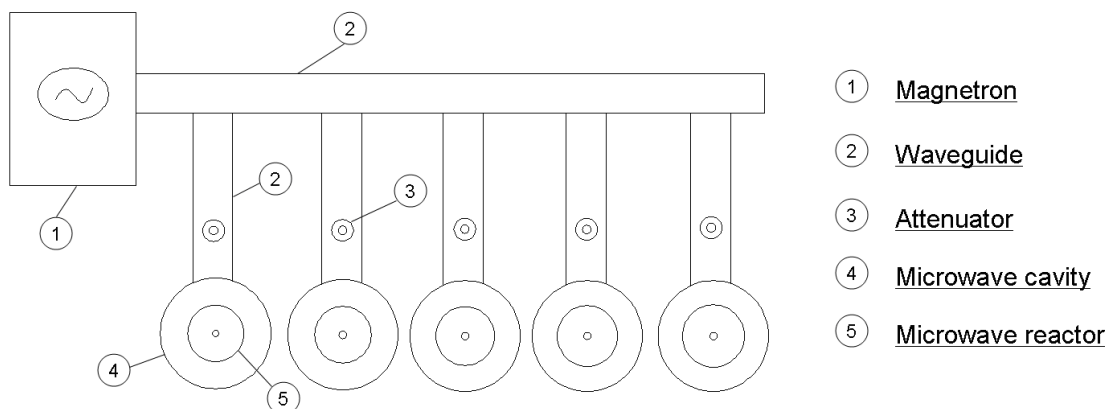


Figure 5.25: Reactors based on microwave waveguides in a parallel manipulation.

heating system are an AC power supply, induction coil, and workpiece. The power supply sends alternating current through the coil, generating a magnetic field. When the workpiece is placed in the coil, the magnetic field induces eddy current in the workpiece, generating precise amounts of clean, localized heat without any physical contact between the coil and the workpiece [88]. Parallel manipulation is easily achieved in the induction heating method and the schematic designs are shown in Figures 5.27 and 5.28. In Figure 5.27, eddy current strength is attenuated by voltage transformer, while in Figure 5.28, different amounts of materials that attenuate electromagnetic radiation are mixed with samples in each reactor, and the reactors are heated simultaneously in a semi-batch mode by the same electromagnetic radiation source.

5.3 Discussion

Literature review has been done to show issues we have to figure out before building a sophisticated electromagnetic heating system. Totally three generation microwave heating systems have been built. Basic tests are conducted to show great potential of applying electromagnetic heating to carry out ramped temperature oxidation experiments.

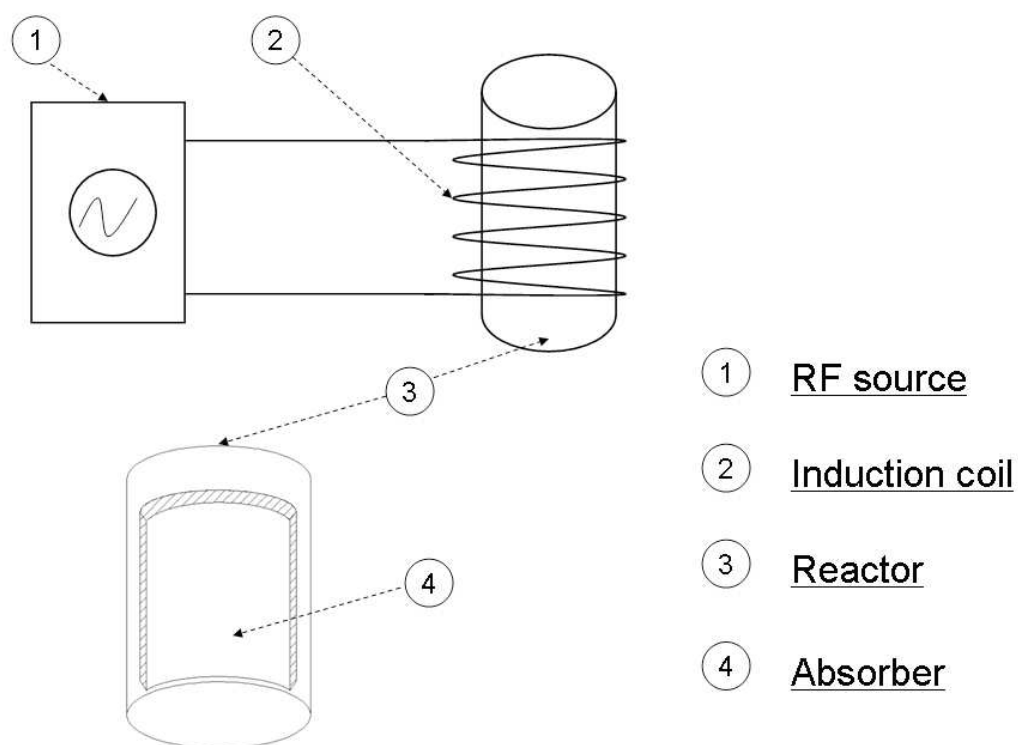


Figure 5.26: Schematic of reactor heated by RF radiation.

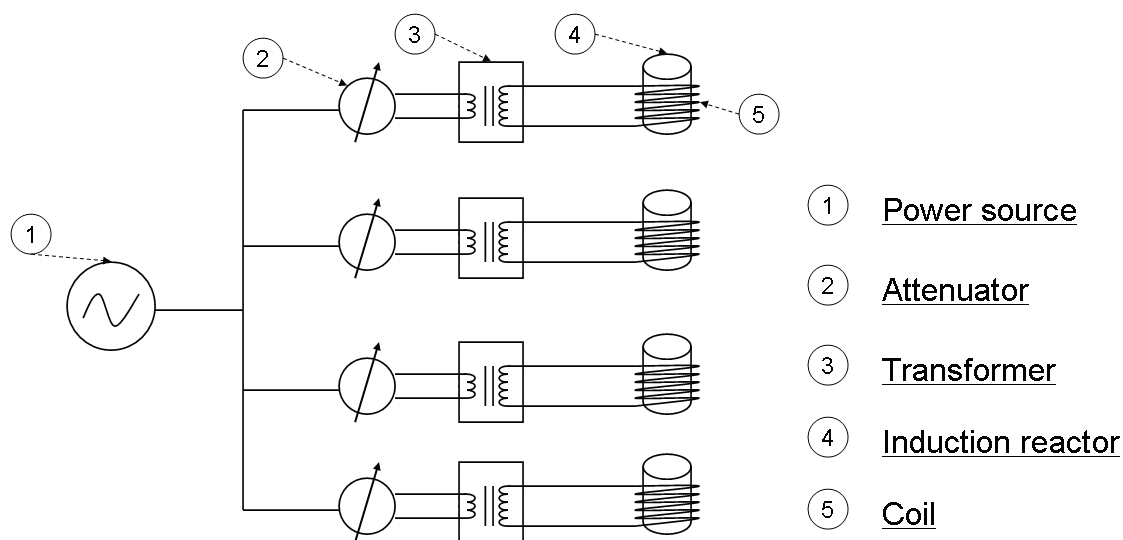


Figure 5.27: Induction heating with separate attenuator to achieve parallel heating.

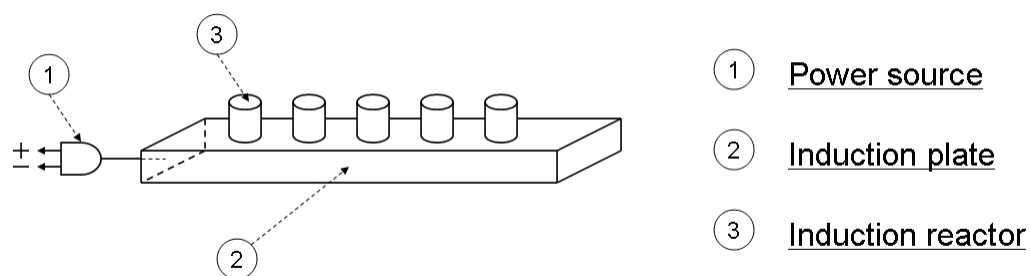


Figure 5.28: Induction heating with different masses of RF absorber to achieve parallel heating.

Future work is needed to reach reliably high temperatures. A better insulating material may be needed to reduce the heat loss. Mixing small SiC cylinders with the crude-oil sample is a good alternative to achieve high temperature as shown in the 1st generation system, and improvement is needed to make the temperature distribution more homogeneous during the heating period. Rather than using the built-in power control system of the microwave oven, an well-designed power control system is needed to control the temperature program more precisely.

Chapter 6

Summary and discussion

The combination of the ramped temperature oxidation (RTO) experiment and the isoconversional principle interpretation unlocks the reaction kinetics of crude-oil combustion in a practical fashion. The nonisothermal RTO experiments that undergo different heating rates widen the temperature range of data collection. This is believed to be of great advantage over those experiments carried out under the isothermal condition. The isoconversional principle is a model-free interpretation tool. The apparent activation energy fingerprint represents the reaction paths. The two representative reaction stages, LTO and HTO are easily identified. An ignition zone at the very beginning and a transition zone in between LTO and HTO stages are also found. The isoconversional fingerprint inherently contains impact factors on reaction paths of the crude-oil combustion, such as reactions in different phases, interaction between components, reservoir matrix surface area affect, and so on. Analyzing the fingerprint provides significant information on the reaction kinetics of crude-oil combustion.

When applying the isoconversional principle to interpret effluent data from RTO experiments, the very first and essentially important issue is the reliability of experiments and data interpretations. This goes to the issue of consistency. Because of the complicated reaction mechanism of the crude-oil combustion, minimizing heat released from exothermic reactions is critical and necessary. This argument is supported by both simulations with a four-reaction synthetic model in a virtual kinetic cell (VKC) simulator and experiments of different crude-oil sample mixtures. The

heat released from reactions causes deviations on temperature profiles, that alter the reaction paths and thus the isoconversional fingerprint. On the other hand, when the heat released is controlled at a very low level, experiments of different injection gas flow rates, different crude-oil sample sizes, and different kinetic cell designs exhibit consistent isoconversional fingerprints. The results not only support the model-free nature of the isoconversional principle, but also they convince us the combination of RTO experiments and the isoconversional principle provide a reliable workflow to investigate crude-oil combustion kinetics.

The activation energy values are the most critical parameter in building a reaction model. The isoconversional principle is first developed to interpret activation energy, however, its capability is far beyond the activation energy interpretation. Combining both the isoconversional principle and conventional interpretation methods determines values for kinetic parameters, such as pre-exponential factor and reaction orders. Rather than optimizing a multi-object function of the kinetic model (that is always questioned by many researchers because of the mathematical solution lack of physical meaning) interpreting parameter values from experimental measurements using the combination method is more promising. A three-reaction scheme is proposed based on the analysis of the isoconversional fingerprint and effluent data. Three reaction stages are described in the scheme, including ignition, LTO and HTO stages. Both simulations and experimental cases show the combination workflow to build a reaction model for each reaction of the scheme. The simulation results for the combustion of two crude-oil mixtures within a kinetic cell show good history matches with respect to effluent gases and temperatures.

The isoconversional fingerprint represents the apparent reaction paths of the crude-oil combustion. The reaction paths may have strong responses when the crude-oil is mixed with rock matrix of different characters. The matrix surface area is a critical factor for the heat conductivity during the combustion process, and thus the reaction paths that are altered according to temperature variations. The surface area effect, when analyzing the isoconversional fingerprint interpreted from RTO experiments, is clearly observed. Smaller grain size implies greater surface area, and thus more enhancement of crude-oil combustion. Coke formations under air and nitrogen

conditions are investigated. The fuel for the HTO reaction is generated in a isothermal batch reactor at a certain temperature. The coke is extracted by toluene from the fuel. Its characteristics are studied by RTO experiments and XPS analysis. The isoconversional principle naturally deconvolves the multi-step reaction mechanism of the crude-oil combustion. LTO and HTO reaction stages are easily identified from the fingerprint. The isoconversional principle is applied to the RTO experiments to interpret the activation energy fingerprint for coke. A good match of activation energy values between the coke and the HTO stage of the crude oil combustion is found. XPS analysis of different kinds of coke formed under air and nitrogen conditions shows more oxygen composition is found in the air coke than the nitrogen coke. Last but not least is applying the isoconversional fingerprint as a diagnostic tool to screen the crude-oil/matrix pairs as good candidates for the ISC process. The fingerprint of a good candidate shows a smooth shape, while a bad candidate normally has an energy barrier at the very beginning of the combustion process.

Applying the isoconversional interpretation to RTO experiments needs at least four experiments at different heating rates. Because of the long heating-cooling cycle of the electric furnace system, a faster and more compact kinetic cell system is more preferred. Electromagnetic heating is a good candidate to replace the conventional electric heating system. Not only the unconventional heating method makes the system compact, achieving fast heating rates, shortening the heating-cooling circle, but also the method can easily be expanded to parallel operation where several RTO experiments are carried out simultaneously. Microwave are a kind of electromagnetic energy. Three generations of the microwave heating system have been developed to date. A maximum temperature of 500 °C is achieved.

The isoconversional principle is a useful interpretation tool to deconvolve the reaction kinetics of crude-oil combustion. Future work is suggested to focus on applying the principle to RTO experiments at large heating rates ($> 20^{\circ}\text{C}/\text{min}$). Because of the complication of crude-oil reaction kinetics and the overlapped reaction zones, faster heating rate experiments are expected to get lower apparent activation energies than that of experiments of low heating rates. Meanwhile more work is needed to improve the proposed workflow of defining reaction parameters, such as reaction

orders for fuel and oxygen partial pressure, and frequency factors. A more sophisticated workflow is needed to post-process the RTO experiment data so that a robust reaction model is built. The electromagnetic heating is believed to be great potential to the RTO experiments. More work is needed to improve the system to achieve high temperature, accurate temperature control and working under elevated pressure conditions.

Appendix A

Updates for the kinetic cell and combustion tube systems

1. Electric Furnace: Thermcraft No. XSL-3-0-18-1C is installed.
2. Solid state relay: No. SSR330DC25, 24 to 330 *VAC*, 25 *Amp*.
3. Temperature USB hub: 8 Channel Thermocouple Data Acquisition (DAQ) Module.
4. Kinetic cell: the wall thickness is machined to be thinner than the previous design. The adjustment is to make the temperature respond more quickly.
5. Isothermal kinetic cell: as described in Figure 4.9 in Chapter 4, the kinetic cell is used to generate coke components at elevated pressure. It can be used as the normal kinetic cell in RTO as well.
6. Gas analyzer: SERVOPRO 4200. The calibration gases for the gas analyzer is O_2 - 50%, CO_2 - 25%, CO - 25%, N_2 - 100%. The upper limit for measurement of CO and CO_2 is 25%.
7. Mass flow controller: it needs to be calibrated before experiments. Table A.1 is for reference of air calibration.

Table A.1: Mass flow controller calibration table for air

Inlet, L/min	Outlet, L/min
0.85	0.80
1.06	1.00
1.66	1.50
2.20	2.00
4.55	4.01

Table A.2: Thermocouple enumeration for the kinetic cell system

Thermocouple location	Port on the USB hub
bottom of kinetic cell	Dev.0 Ti.0
center of kinetic cell	Dev.0 Ti.1
top of kinetic cell	Dev.0 Ti.2
furnace	Dev.0 Ti.7

8. Electric fan: the electric fan located at the bottom of the electric furnace is used to assist cooling of the furnace. Using the electric fan, the furnace is cooled from $650\text{ }^{\circ}\text{C}$ to $60\text{ }^{\circ}\text{C}$ in 2 hours. During the cooling period, the preparation for the new experiment is processed, the gas analyzer is calibrated. 3 to 4 RTO experiments can be processed per day.
9. Copper gasket: 500 pieces. O.D = 1.5 inch, I.D = 1.1 inch, thickness = 0.125 inch. (unit cost - \$1.6; ordered from Ace Seal, LLC, 23 Las Colinas Lane Suite 108, San Jose, CA 95119)
10. Thermocouples enumeration: Table A.2 for kinetic cell system; Table A.3 for combustion tube.

Table A.3: Thermocouple enumeration for the combustion tube

Thermocouple location	Port on the USB hub
Heater	Dev.1 Ti.0
CH.1	Dev.1 Ti.1
CH.2	Dev.1 Ti.2
CH.3	Dev.1 Ti.3
CH.4	Dev.1 Ti.5
CH.5	Dev.1 Ti.6
CH.6	Dev.1 Ti.7
CH.7	Dev.2 Ti.0
CH.8	Dev.2 Ti.2
CH.9	Dev.2 Ti.3
CH.10	Dev.2 Ti.4
CH.11	Dev.2 Ti.5
CH.12	Dev.2 Ti.7
CH.13	Dev.3 Ti.0
CH.14	Dev.3 Ti.2
CH.15	Dev.3 Ti.3

Appendix B

Background correction of effluent data

Effluent data drift causes the tail of the gas production history to be non-zero. It makes the isoconversional interpretation inconsistent. The data drift is caused by two factors: electric current of the gas module drifts in the gas analyzer, and some components in the sand mixture are oxidized at high temperatures. The objective of background correction of the effluent data is to force the non-zero values at the tail of the gas production history to be zero.

The proposed method rotates the effluent data curve by a certain angle. The value of the angle is determined by the first non-zero oxygen consumption point (i.e. where the oxidation starts) and the expected completion point at the end of the oxidation. Figure B.1 shows two similar temperature histories whose effluent data is expected to be very similar as well. Because of the data drift, effluent data in Figure B.2(a) is not consistent. After background correction by curve rotation, the result is shown in Figure B.2(b), exhibiting very consistent behaviors.

```
% curve_shift.m  
% rotate effluent curves to do back ground correction.  
% Bo Chen, SUPRI-A, Stanford University
```

```

clc;
clear all;
end_point_time = 18185; %second

load E:\matlabworks\Preprocessing\input.txt;
plot(input(:,1),input(:,2));
grid on;
hold all;
index_end_point_time = find(input(:,1)==end_point_time);
plot(input(index_end_point_time,1),input(index_end_point_time
    ,2),'r*');
hold all;

shit_tan_angel = input(index_end_point_time,2)/input(
    index_end_point_time,1);
first_non_zero = find(input(:,2)>0);
first_non_zero = first_non_zero(1);
initial_part = input(1:first_non_zero-1,:);
end_part = input(index_end_point_time+1:end,:);
end_part(:,2) = 0;
shitf_part = input(first_non_zero:index_end_point_time,:);
if shit_tan_angel > 0
    shitf_part(:,2) = shitf_part(:,2) - shitf_part(:,1)*
        shit_tan_angel;
else
    shitf_part(:,2) = shitf_part(:,2) - shitf_part(:,1)*
        shit_tan_angel;
end
shitf_curve = [initial_part;shitf_part;end_part];

plot(shitf_curve(:,1),shitf_curve(:,2),'g');

```

```
hold off;  
legend('original ','shifted');
```

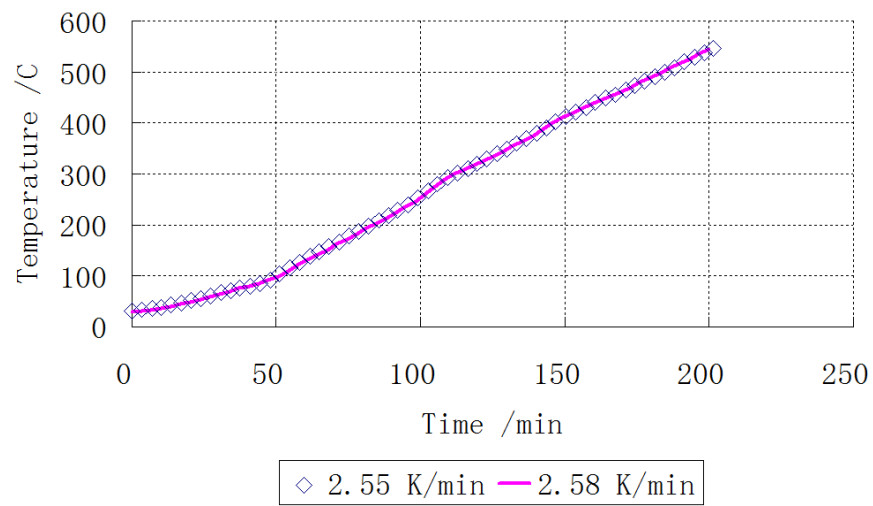
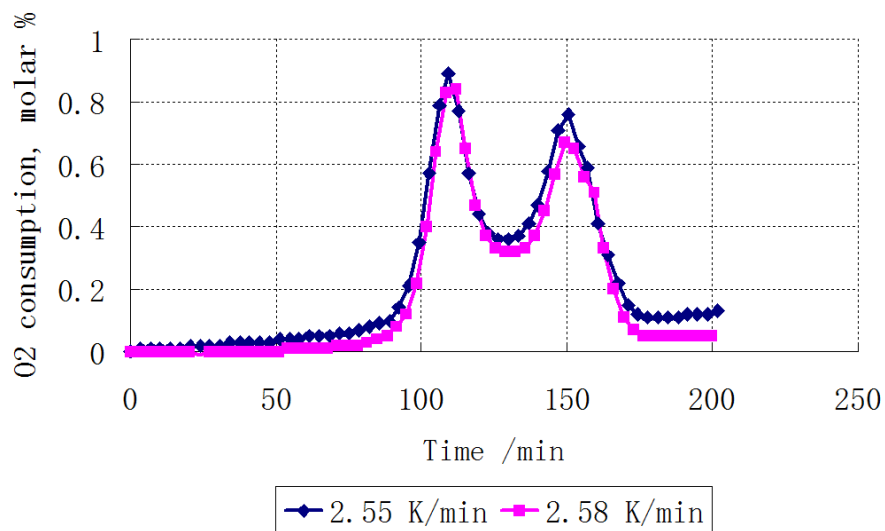
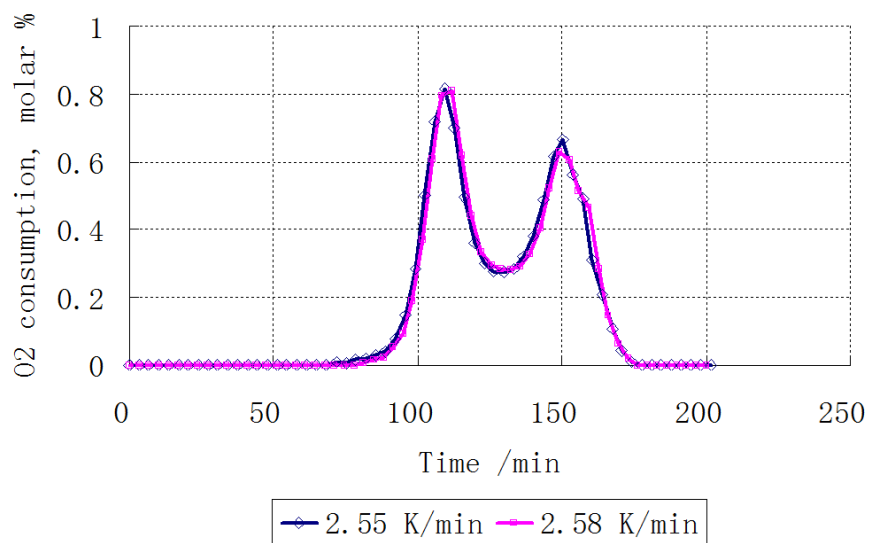


Figure B.1: Temperature histories for RTO experiments.



(a) Before data background correction.



(b) After data background correction.

Figure B.2: Background correction example for two RTO experiments.

Appendix C

Kinetic cell experiment preparation

Preparing the crude-oil sample mixture for consistent RTO experiments is critical. Much care is needed. Some tips from my experience on preparing the sample mixture are listed:

1. Sand is cooked for at least 4 hours at a temperature of $650\text{ }^{\circ}\text{C}$ to oxidize reactive components on the sand surface.
2. Use 25 *g* of the fired sand to fill up the dispersion cup at the bottom of the kinetic cell.
3. A bigger sample mixture than the one used in the experiment is prepared. For instance, while the Karamay crude-oil/sand mixture of 15 *gram* is used in the RTO experiment, a bigger sample mixture of 25 *gram* is made. 15 *gram* is taken from the bigger sample mixture and used in the experiment. This is just to reduce errors caused by oil and water vaporization, oil residues on the mixing spoons and cups, and imperfect mixing to make homogeneous sample mixture.
4. Two spoons are suggested when mixing the sample, so that the residual oil on a spoon can be removed by the other one.

5. After putting the crude-oil mixture in the center of the kinetic cell, the rest room of the cell chamber is filled up with fired sand.
6. Fresh sample mixture is suggested for every RTO experiment, but it is not necessary. The exposure of the mixture in the air causes water and light components of the crude oil to be vaporized, but these components do not react with oxygen during the RTO experiment.
7. Clean screws with lubricant everytime before assembling the kinetic cell. Wait until the kinetic cell completely cooled down before unscrewing screws.

Appendix D

Codes for virtual kinetic cell simulation and isoconversional interpretation

The VKC and both differential and integral isoconversional methods are coded in MATLAB. Functions of the simulator are listed:

- ISCMaInStart.m — input parameters and result plots;
- ActEnergy.m — differential and integral isoconversional methods;
- govenEqn.m — governing equations for the VKC;
- ISCsolver.m — equation solver;
- phiEnergy.m — sub-equation for the integral isoconversional method;
- prodRate.m — net reaction rate;
- prodRate2.m — net reaction rate;
- reactionRate.m — Arrhenius rate law;

```
***** ISCMaInStart.m
% Virtual Kinetic Cell Simulation
% version 2.0, updated on April 15, 2011
% Developed by Bo Chen, SUPRI-A, Stanford University

% Totally 7 species are in the reaction scheme:
% A, C, and D are in liquid/solid phase;
% Others are in gas phase;
% Number of reactions is expandable through stoichiometri
  coefficient matrices

% reaction mechanism
% A + B -> C, k1
% C -> D + F, k2
% A + B -> H + G + F, k3
% D + B -> H + G + F, k4

clc;
clear all;

MD.Arrhenius = [1, 1, 100, 80;...
                63000, 80000, 125000, 100000]'; % constant
                [1/(mole*s)]; activation energy [J/mole]

MD.heatReaction = [-10000, 40000, -60000, -40000]'; % heat of
  reaction [J/mole]

MD.Cp = [200.0, 35, 100, 100, 50, 60, 35]'; % heat capacity [
  J/mole]
```

```

MD.nu_ji_p = [1, 1, 0, 0, 0, 0, 0; ... // stoichiometri
               coefficient matrices
               0, 0, 0, 0, 0, 0, 0; ... // reactant
               0, 0, 0, 0, 0, 0, 0; ...
               0, 1, 0, 1, 0, 0, 0];
MD.nu_ji_dp = [0, 0, 0, 1, 0, 0, 0; ... // products
               0, 0, 0, 0, 0, 0, 0; ...
               0, 0, 0, 0, 0, 0, 0; ...
               0, 0, 0, 0, 1, 1, 1]; ...

MD.reaction_order_P = [1, 1, 0, 0, 0, 0, 0; ... // reaction
                       orders
                       0, 0, 0, 0, 0, 0, 0; ... // reactant
                       0, 0, 0, 0, 0, 0, 0; ...
                       0, 1, 0, 1, 0, 0, 0];

MD.reaction_order_dP = [0, 0, 0, 0, 0, 0, 0; ... // products
                       0, 0, 0, 0, 0, 0, 0; ...
                       0, 0, 0, 0, 0, 0, 0; ...
                       0, 0, 0, 0, 0, 0, 0]; ...

% Initial & Boundary conditons
IC.T0 = 298.15; % [K]
IC.Ua = 15000; % [J/(m^3*s*k)]
IC.V = 0.00004; % [m^3]
IC.q = 2/(1000*60); % volume frow rate
IC.P = 0.8*100*6.894e3; % pis
R = 8.314;
IC.initialCond = [20000, IC.P/(R*IC.T0), 0, 0, 0, 0, 0, IC.T0];
%rateHeat = [3, 4, 5, 6]'/60; % K/sec
rateHeat = [1.54, 1.74, 1.93, 3.3]'/60; % K/sec

```

```

% Solve the governing equation
Tspan= [0,500*60];
T_int = 6000;

for i = 1:length(rateHeat)
    IC.rateHeat = rateHeat(i); % K/sec
    [T, Y] = ISCsolver(MD, IC, Tspan); % small numerical
        solver for kinetic cell
    time_line(:,i) = linspace(0,Tspan(2),T_int)';
    consumption_B(:,i) = IC.P/(R*IC.T0) - interp1(T,Y(:,2),
        time_line(:,i));
    index_negative = find(consumption_B(:,i)<0);
    consumption_B(index_negative,i)=0;
    Temp_line(:,i) = interp1(T,Y(:,end),time_line(:,i));
end

figure
for i = 1:length(rateHeat)
    plot(time_line(:,i),consumption_B(:,i),'*');
    hold all;
end
xlabel('Temperature');
ylabel('Consumption');

est_range = [-1e2,1e6];
[AEnergy1, Conversion1] = ActEnergy(consumption_B, Temp_line,
    time_line,'Friedman',est_range);
%[AEnergy2, Conversion2] = ActEnergy(consumption_B, Temp_line,
    time_line,'Vyazovkin 1997',est_range);

```

```

[AEnergy3, Conversion3] = ActEnergy(comsuption_B, Temp_line,
    time_line, 'Vyazovkin 2001', est_range);

figure
%subplot(2,1,1)
for i = 1:length(rateHeat)
    plot(time_line(:,i)/60,comsuption_B(:,i),'*-');
    hold all;
end
axis([0,Tspan(2)/60,0,25]);
grid on;
xlabel('Time,min','FontSize',14,'FontName','Aharoni');
ylabel('O2 comsuption, mole/m^3','FontSize',14,'FontName','Aharoni');
legend('1.54 K/min','1.74 K/min','1.93 K/min','2.64 K/min');
set(legend,'FontSize',14,'FontName','Aharoni');
hold off;

figure
%subplot(2,1,2)
for i = 1:length(rateHeat)
    plot(time_line(:,i)/60,Temp_line(:,i)-273.15,'*-');
    hold all;
end
grid on;
xlabel('Time,min','FontSize',14,'FontName','Aharoni');
ylabel('Temperature, K','FontSize',14,'FontName','Aharoni');
legend('1.54 K/min','1.74 K/min','1.93 K/min','2.64 K/min');
set(legend,'FontSize',14,'FontName','Aharoni');
hold off;

```

```

figure
%subplot(2,2,3)
plot(Conversion1,AEnergy1,'*',Conversion3,AEnergy3,'go');
axis([0,1,0.4e5,1.4e5]);
grid on;
xlabel('Conversion','FontSize',14,'FontName','Aharoni');
ylabel('Activation Energy, J/mole','FontSize',14,'FontName','Aharoni');
legend('Friedman','Vyazovkin 2001','Location','SouthEast');
set(legend,'FontSize',14,'FontName','Aharoni');
hold off;

*****

***** ActEnergy.m
function [AEnergy, Conversion] = ActEnergy(comsuption_B,
    Temp_line, time_line, options, est_range)

% Isoconversional method
% activation energy solver

R = 8.314;
num_expij = size(comsuption_B);
num_exp = num_expij(2);
length_B = num_expij(1);
num_interp = 100;

x= linspace(0.001,0.999,num_interp);
x = x';

```



```

for i = 1:num_exp
    index = find(comsuption_B(:,i)>0.001);
    index_start = index(1);
    index_end = index(end);
    Temp_temp = Temp_line(index_start:index_end,i);
    Time_temp = time_line(index_start:index_end,i);
    Time_span_temp = [Time_temp(2:end);0] - Time_temp;
    Time_span = [Time_span_temp(1:end-1); Time_span_temp(end
        -1)];
    isoconversionB = comsuption_B(index_start:index_end,i).*
        Time_span;
    B_total(i) = sum(isoconversionB);
    xx = zeros(length(isoconversionB),1);
    for j = 1:length(isoconversionB);
        xx(j) = sum(isoconversionB(1:j))/B_total(i);
    end
    Temp_x(:,i) = interp1(xx,Temp_temp,x);
    x_Time(:,i) = interp1(xx,Time_temp,x);
end

if strcmp(options, 'Friedman')
    for i = 1:num_exp
        dxdt(:,i) = interp1(time_line(:,i),comsuption_B(:,i)
            ,x_Time(:,i),'spline')/B_total(i);
    end
    ln_dxdt = log(dxdt);

    for j = 1:num_interp
        LineSlope = polyfit(-1./(R*Temp_x(j,:)),ln_dxdt(j,:),1);
        AEnergy(j) = LineSlope(1);
    end
end

```

```

AEnergy = AEnergy';
Conversion = x;

end
% Vyazovkin

if strcmp(options, 'Vyazovkin 1997')
    delta_t = num_interp;
    for index_x = 2:num_interp
        if index_x <= delta_t
            Cal_Ex (index_x-1) = fminbnd(@(Ex) phiEnergy( Ex,
                Temp_x(1:index_x,:), x_Time(1:index_x,:) ),
                est_range(1),est_range(2));
        else
            Cal_Ex (index_x-1) = fminbnd(@(Ex) phiEnergy( Ex,
                Temp_x(index_x-delta_t+1:index_x,:), x_Time(
                index_x-delta_t+1:index_x,:) ),est_range(1),
                est_range(2));
        end
    end
    AEnergy = Cal_Ex;
    Conversion = x(2:end);

end

if strcmp(options, 'Vyazovkin 2001')
    delta_t = 2;
    for index_x = 2:num_interp
        if index_x <= delta_t

```

```

    Cal_Ex (index_x-1) = fminbnd(@(Ex) phiEnergy( Ex,
        Temp_x(1:index_x,:) , x_Time(1:index_x,:) ),
        est_range(1),est_range(2));
    else
    Cal_Ex (index_x-1) = fminbnd(@(Ex) phiEnergy( Ex,
        Temp_x(index_x-delta_t:index_x,:) , x_Time(index_x-
        delta_t:index_x,:) ),est_range(1),est_range(2));
    end
end
AEnergy = Cal_Ex;
Conversion = x(2:end);

end

*****

***** govenEqn.m

function dydt = govenEqn(t,y,MD,IC)

% y = [x1,x2,x3...xi,T]

Arrhenius = MD.Arrhenius;
heatReaction = MD.heatReaction;
Cp = MD.Cp;
nu_ji_p = MD.nu_ji_p;
nu_ji_dp = MD.nu_ji_dp;
reaction_order_P = MD.reaction_order_P;
reaction_order_dP = MD.reaction_order_dP;
dim_nu = size(MD.nu_ji_p);

```

```

num_spec = dim_nu(2);
num_reac = dim_nu(1);

% Initial & Boundary conditons
T0 = IC.T0;
Ua = IC.Ua;
V = IC.V;
q = IC.q;
rateHeat = IC.rateHeat;
R = 8.314;    % J/mole.k
P = IC.P; % pa

index_T = num_spec + 1;
dydt = zeros(index_T,1); % mole concentration and T
kfr = reactionRate(num_reac, Arrhenius, y(index_T));
if (imag(y(1)) ~= 0)
    y(1) = 0;
end

if y(1) < 0
    y(1) = 0;
end

omega_j = prodRate(MD, kfr, [y(1); IC.initialCond(2); y(3:
    end-1)]);
omega_i = prodRate2(MD, kfr, [y(1); IC.initialCond(2); y(3:
    end-1)]);

F_B0 = P*q/(R*T0);
v_rate = q; % m^3/s

```

```

theta = zeros(num_spec,1);
for j = 1:num_spec
    theta(j) = (y(j)*v_rate)/F_B0;    %mole Fraction
    *****
end

theta(1) = 0;
theta(3) = 0;
theta(4) = 0;

Ta = T0 + rateHeat*t;
Q = Ua*V*(Ta-y(index_T));

% Govening eqautions
dydt(1) = omega_j(1);    % y is mole concentration
dydt(2) = (F_B0 - F_B0*theta(2))/V + omega_j(2);
dydt(3) = omega_j(3);
dydt(4) = omega_j(4);
dydt(5) = (-F_B0*theta(5))/V + omega_j(5);
dydt(6) = (-F_B0*theta(6))/V + omega_j(6);
dydt(7) = (-F_B0*theta(7))/V + omega_j(7);

sum1 = 0;
sum3 = 0;
for j = 1:num_spec
    sum1 = sum1 + theta(j)*Cp(j)*(y(index_T) - Ta);
    sum3 = sum3 + y(j)*Cp(j);
end

```

```

delta_Cp_i = nu_ji_dp*Cp - nu_ji_p*Cp;
heat_Reaction_i = delta_Cp_i.*(y(index_T) - T0)+heatReaction;
heat_Reaction_ij(1) = heat_Reaction_i(1)*omega_i(1);
heat_Reaction_ij(2) = heat_Reaction_i(2)*omega_i(2);
heat_Reaction_ij(3) = heat_Reaction_i(3)*omega_i(3);
heat_Reaction_ij(4) = heat_Reaction_i(4)*omega_i(4);

```

```

sum2 = sum(heat_Reaction_ij);

```

```

dydt(index_T) =(Q - F_B0*sum1 + V*sum2)/(sum3*V);    % eqn.
5.32

```

```

*****

```

```

***** ISCsolver.m

```

```

function [T, Y] = ISCsolver( MD, IC, Tspan)

```

```

options = odeset('RelTol',1e-7);

```

```

[T Y] = ode15s(@(t,y) govenEqn(t,y,MD,IC),Tspan,IC.
    initialCond,options); % Solve ODE

```

```

end

```

```

*****

```

```
***** phiEnergy.m
```

```
function phi_Ex = phiEnergy( Ex,Temp_x, x_Time )
```

```
num_exp = size(Temp_x);
```

```
num_exp = num_exp(2);
```

```
R = 8.314;
```

```
for i = 1:num_exp
```

```
    J_E_Tt(i) = trapz(x_Time(:,i),exp(-Ex./(R*Temp_x(:,i)
    )));
```

```
end
```

```
sum = 0;
```

```
for i = 1:num_exp
```

```
    for j = 1:num_exp
```

```
        if j ~= i
```

```
            sum = sum +J_E_Tt(i)/J_E_Tt(j);
```

```
        end
```

```
    end
```

```
end
```

```
phi_Ex = sum;
```

```
*****
```

```
***** prodRate.m
```

```
function [ omega_j ] = prodRate(Nu, kfr, MoleFraction )
```

```
% Net production rate for each speices j
```

```

% Nu.nu_ji_p , Nu.nu_ji_dp
% omega_j = sum(nu_ji*q_i) ... eqn 4.31 from An Introduction
    to Combustion
% nu_ji = nu_ji_dp - nu_ji_p ... eqn 4.32 from An
    introduction to Combustion
% q_i = k_fi * ([x_j])^(v

% j — Species example 1: A,B,C,D,F,G,H
% i — Reaction example 1: R1,R2,R3,R4
% kf_i — Forward reaction rate of reaction i
% kr_i — backward reaction rate of reaction i
% MoleFraction = [A,B,C,D,F,G,H]

nu_ji_p = Nu.nu_ji_p;
nu_ji_dp = Nu.nu_ji_dp;
nu_ji = nu_ji_dp - nu_ji_p;

reaction_order_P = Nu.reaction_order_P;
reaction_order_dP = Nu.reaction_order_dP;

kf_i = kfr(:,1);
kr_i = kfr(:,2);

Num_reac = length(nu_ji_p(:,1));
Num_spec = length(nu_ji_p(1,:));

moleFracProd_p = ones(Num_reac,1)';
moleFracProd_dp = ones(Num_reac,1)';
for i = 1:Num_reac
    for j = 1:Num_spec

```



```

        moleFracProd_p(i) = moleFracProd_p(i)*MoleFraction(j)
        ^reaction_order_P(i,j);
        moleFracProd_dp(i) = moleFracProd_dp(i)*MoleFraction(
            j)^reaction_order_dP(i,j);
    end
end

q_i = kf_i.*moleFracProd_p' - kr_i.*moleFracProd_dp';

for i = 1:Num_reac
    omega(i,:) = nu_ji(i,:)*q_i(i);
end

for j = 1:Num_spec
    omega_j(j) = sum(omega(:,j));
end

*****

***** prodRate2.m

function [ omega_i ] = prodRate2( Nu, kfr, MoleFraction )

nu_ji_p = Nu.nu_ji_p;
nu_ji_dp = Nu.nu_ji_dp;
nu_ji = nu_ji_dp - nu_ji_p;
reaction_order_P = Nu.reaction_order_P;
reaction_order_dP = Nu.reaction_order_dP;

```

```

kf_i = kfr(:,1);
kr_i = kfr(:,2);

Num_reac = length(nu_ji_p(:,1));
Num_spec = length(nu_ji_p(1,:));

moleFracProd_p = ones(Num_reac,1)';
moleFracProd_dp = ones(Num_reac,1)';
for i = 1:Num_reac
    for j = 1:Num_spec
        moleFracProd_p(i) = moleFracProd_p(i)*MoleFraction(j)
            ^reaction_order_P(i,j);
        moleFracProd_dp(i) = moleFracProd_dp(i)*MoleFraction(
            j)^reaction_order_dP(i,j);
    end
end

q_i = kf_i.*moleFracProd_p' - kr_i.*moleFracProd_dp';

for i = 1:Num_reac
    omega(i,:) = nu_ji(i,:)*q_i(i);
end

omega_i(1) = omega(1,1);
omega_i(2) = omega(2,3);
omega_i(3) = omega(3,1);
omega_i(4) = omega(4,4);

```

```
*****
```

```
***** reactionRate.m
```

```
function [ kfr ] = reactionRate( Num_Reaction, Arrhenius ,  
    T_current )
```

```
kfr = zeros(Num_Reaction,2); % reversed reaction not  
    considered yet
```

```
R = 8.314; % J/mole.k
```

```
kfr(:,1) = Arrhenius(:,1).*exp(-Arrhenius(:,2)./(R*T_current)  
    );
```

```
end
```

Appendix E

Input file of kinetic cell simulation for CMG-STARS

****-----INPUT-OUTPUT CONTROL**

*TITLE1 'Simulation of ramped temperature oxidation within a
kinetic cell system'

*TITLE2 'Bo Chen, SURPI-A, Stanford University '

*TITLE3 'updated at July 12, 2012'

*INUNIT *LAB **Input/output data unit

*OUTUNIT *LAB

*WPRN *GRID *TIME **WPRN controls the frequency of writing
to the output print file information flagged by *OUTPRN

*WPRN *ITER *TIME **ITER pertains to the brief well rate
report as well as simulator performance, e.g., material
balance

*OUTPRN *GRID *PRES *TEMP *Y *X *MASS *SOLCONC

```

*OUTPRN *WELL *WELLCOMP
*OUTPRN *ITER *BRIEF  ** interation result

*WSRF *GRID *TIME
*WSRF *WELL *TIME

**OUTSRF *WELL *MASS *COMPONENT *ALL
*OUTSRF *WELL *MOLE *COMPONENT *ALL
*OUTSRF *GRID *PRES *TEMP *Y *X *MASS *SOLCONC

*OUTSRF *SPECIAL MATBAL CURRENT 'CO'
                                MATBAL CURRENT 'CO2'
                                MATBAL CURRENT 'N2'
                                MATBAL CURRENT 'O2'
                                MATBAL CURRENT 'H2O'
                                MATBAL CURRENT 'Coke'

                                MATBAL REACTION 'CO'
                                MATBAL REACTION 'CO2'
                                MATBAL REACTION 'O2'
                                MATBAL REACTION 'H2O'
                                MATBAL REACTION 'Coke'

                                MOLEFRAC 'PRODUCER' 'CO' GAS
                                MOLEFRAC 'PRODUCER' 'CO2' GAS
                                MOLEFRAC 'PRODUCER' 'N2' GAS
                                MOLEFRAC 'PRODUCER' 'O2' GAS

                                BLOCKVAR TEMP 1,1,3
                                BLOCKVAR TEMP 1,1,4
                                BLOCKVAR TEMP 1,1,5

```

BLOCKVAR TEMP 4,1,4 **Heater

*INTERRUPT *STOP

**-----RESERVOIR DESCRIPTION

** Kinetic cell I.D. = 3.1 cm.

** Total lenght of the kinetic cell 12.0 cm

*GRID *RADIAL 4 1 7 *RW 0

*KDIR *Up

*DI *IVAR 1.55 0.5 0.5 8

*DJ *CON 360

*DK *KVAR 10 1.5 4 4 4 1.5 10

*POR *CON 0.4

 *MOD 2:4 1 1:7 = 0.0 ** kinetic cell

** 1 1 1:2 = 0.0

** 1 1 6:7 = 0.0

*PERMI *CON 30000

 *MOD 2:4 1 1:7 = 0

** 1 1 1:2 = 0.0

** 1 1 6:7 = 0.0

*PERMJ *EQUALSI

*PERMK *EQUALSI

*end-grid

** Rock 1: oil mixture

```

** Rock 2: stainless steel 316
** Rock 3: air
** Rock 4: furnace

```

```

*ROCKTYPE 1  ** oil mixture
*PRPOR 100.
*CPOR 7.E-06
*ROCKCP 4.39      **J/cm^3.C
*THCONR 9.236E-01
*THCONS 9.236E-01
*THCONW 2.708
*THCONO 9.236E-01
*THCONG 4.167E-02
*THCONMIX SIMPLE

```

```

*ROCKTYPE 2  ** Stainless Steel 316
*ROCKCP 4.016
*THCONR 9.7

```

```

*ROCKTYPE 3  ** Air
*ROCKCP 0.00121
*THCONR 4.16e-2

```

```

*ROCKTYPE 4  ** Furnace
*ROCKCP 20
*THCONR 2e6

```

```

*THTYPE *IJK 1 1 3:5 1
              2 1 2:6 2
              1 1 2 1
              1 1 6 1

```

```

3 1 1:7 3
2 1 1 2
2 1 7 2
1 1 1 1
1 1 7 1
4 1 1:7 4

**INCLUDE 'reaction_model_alaska.txt'
** ===== FLUID DEFINITIONS =====
*model 9 8 3
** Number of noncondensable gases is numy-numx = 5
** Number of solid components i s ncomp-numy = 1

*compname 'H2O'      'OIL2'  'OIL'   'N2'      'O2'      '
          CO2'      'CO'    'Gas'   'Coke'
**
          -----
          -----  ---CH_0.166---
*cmm      0  6.15E-01  6.15E-01  2.8E-02   3.20E-02   4.40E-02
          2.80E-02      2.8e-2    1.2166E-2
*pcrit    0  890   890      3392      5033      7377
          3496      3496
*tcrit    0  171   171      -147      -118      31
          -144      -144

*KV1 0 0.00E+00 0.00E+00
*KV2 0 0.00E+00 0.00E+00
*KV3 0 0.00E+00 0.00E+00
*KV4 0 0.00E+00 0.00E+00
*KV5 0 0.00E+00 0.00E+00

```



```

*avg 0.00E+00 0.0001610891804 0.0001610891804 0.0003500869287
      0.000362791571 0.0001865724378 0.0003315014585
      0.0003315014585
*bvg 0.00E+00 0.7453161006 0.7453161006 0.6927470725
      0.7120986013 0.7754816784 0.7037315714 0.7037315714
**avisc 0.00E+00 1.426417368E-11 1.426417368E-11
**bvisc 0.00E+00 10823.06574 10823.06574
*cpg1 0.00E+00 26.804420692906 26.804420692906
      30.956477056957 28.600167325729 19.474325955388
      30.990187019402 30.990187019402
*cpg2 0.00E+00 0.005649089963 0.005649089963 -0.012716023994
      -0.003497011859 0.075654731286 -0.01392019971
      -0.01392019971
*cpg3 0.00E+00 0.000095012314 0.000095012314 0.000025490143
      0.000024399453 -0.000060750197 0.00003014996
      0.00003014996
*cpg4 0.00E+00 -0.000000054709 -0.000000054709
      -0.000000011065 -0.000000014928 0.000000020109
      -0.00000001415 -0.00000001415

*cpl1 0.00E+00 524.8821790 524.8821790 0.00E+00 0.00E+00 0.00
      E+00 0.00E+00 0.00E+00
*cpl2 0.00E+00 1.148635444845 1.148635444845 0.00E+00 0.00E
      +00 0.00E+00 0.00E+00 0.00E+00
*hvr 1.00E+00 0.00E+00 0.00E+00
*ev 0.00E+00 0.00E+00 0.00E+00

**molden 0.00E+00 0.001686 0.001686
*cp 0.00E+00 7.25E-07 7.25E-07
*ct1 0.00E+00 0.00069242 0.00069242
*ct2 0.00E+00 0.00E+00 0.00E+00

```

**MOLVOL 0.00E+00 899 899

*MASSDEN 0.00E+00 0.987e-3 0.987e-3

*solid_den 'Coke' 0.0014 0 0

*solid_cp 'Coke' 6.96015 0.03645

*visctable

10	0	994916.5474	994916.5474
20	0	303084.8762	303084.8762
25	0	289000	289000
50	0	11900	11900
80	0	903	903
120	0	107	107
160	0	26.5	26.5
200	0	10.9	10.9
250	0	4.916946375	4.916946375
300	0	2.760860766	2.760860766
350	0	1.910831503	1.910831503
400	0	1.511176928	1.511176928
500	0	1.182780529	1.182780529
600	0	1.070632992	1.070632992
1000	0	1.001866585	1.001866585

**Reac t ions

**compname	'H2O'	'OIL2'	'OIL'	'N2'	'O2'	'CO2'
	'CO'	'Gas'	'Coke'			

**
 _____ CH0.166

** Oil2 —> OIL

*storeac 0 1 0.00E+00 0 0.00 0.00 0.00E+00 0 0.00

```
*stoprod  0  0  1.00E+00 0.00E+00  0.00E+00 0  0  0  0
*RORDER   0.00E+00 1  0.00E+00 0.00E+00  0.00E+00 0.00E+00
          0.00E+00 0  0.00E+00
```

```
*freqfac 1E+10
```

```
*eact 1.0E+005
```

```
*renth 3.6e6
```

```
**O2PP 'O2'
```

```
**Reac t ions
```

```
**compname 'H2O'      'OIL2'  'OIL'   'N2'    'O2'    'CO2'
           'CO'      'Gas'    'Coke'
**
```

```
_____
_____ CH0.166
```

```
** Oil + 15 O2 —> 15 coke + 18.4504 H2O + 2.0661
   CO + 5 CO2 + 12.1089 gas
```

```
*storeac 0.00E+00 0 1.00E+00 0.00E+00 15.000 0.00E+00
          0.00E+00 0 0.00E+00
```

```
*stoprod 18.11 0 0.00E+00 0.00E+00 0.00E+00 5.0000
          2.066115 12.1089 12.5
```

```
*RORDER 0.00E+00 0 1.83E+00 0.00E+00 0.90E+00 0.00E+00
          0.00E+00 0 0.00E+00
```

```
*freqfac 3.69E+15
```

```
*eact 8.5E+004
```

```
*renth 18.6e6
```

```
**O2PP 'O2'
```

```
**compname 'H2O'      'OIL2'  'OIL'   'N2'    'O2'    'CO2'
           'CO'      'Gas'    'Coke'
**
```

```

**      _____
      _____ CH_0.166
** CH_0.166 + 0.8958 O2 —> 0.2083 CO + 0.7917 CO2 +
      0.0831 H2o

*storeac  0.00E+00 0  0.00E+00 0.00E+00 0.8958      0.00E+00
      0.00E+00 0      1.00E+00
*stoprod  0.0831    0  0.00E+00 0.00E+00 0.00E+00 0.7917
      0.2083      0  0.00E+00
*RORDER   0.00E+00 0  1.45E+00 0.00E+00 1.0E+00 0.00E+00 0.00
      E+00 0      1.1E+00
*freqfac  9.95E+013
*eact      1.30E+005
*renth     1.0E+006
**O2PP 'O2'

** Reference conditions

*prsr 101.325
*temr 25
*psurf 101.325
*tsurf 25

*ROCKFLUID

*RPT 1 LININTERP WATWET
*swt **Water-oil relative permeabilities

```

** Sw Krw Krow

** ——— ——— ———

0.18 0 1
 0.2 0.000000217 0.862816
 0.22 0.00000347 0.740736
 0.235 0.0000124 0.658348
 0.25 3.25E-05 0.58327
 0.265 7.07E-05 0.515026
 0.28 0.000135 0.453161
 0.3 0.000281 0.379842
 0.35 0.00113 0.236425
 0.4 0.003171 0.139158
 0.45 0.007193 0.076303
 0.5 0.014193 0.038131
 0.55 0.025367 0.016787
 0.6 0.042117 0.00615
 0.625 0.053007 0.003372
 0.65 0.066047 0.001685
 0.7 0.098964 0.000272
 0.75 0.142877 0.000012
 0.775 0.169641 0.000000531
 0.8 0.2 0
 1 0.6 0

*slt ** Liquid-gas relative permeabilities

** Sl Krg Krog

** ——— ——— ———

0.3 0.718068 0
 0.320968 0.672114 0.000174
 0.362903 0.584799 0.000681
 0.404839 0.503605 0.001952

```

0.446774 0.428524 0.004596
0.530645 0.296665 0.017658
0.614516 0.189147 0.049986
0.698387 0.105876 0.116768
0.740323 0.073298 0.169396
0.782258 0.046733 0.23901
0.824194 0.026159 0.329258
0.866129 0.011546 0.444239
0.908065 0.002853 0.588519
0.92 0.001 0.63
0.93 0.0003 0.67
0.94 0.00005 0.71
0.95 0 0.76715
1 0 1

```

**-----INITIAL CONDITION

```

*INITIAL
*PRES *CON 689.4757  ** kPa, 100 psi
*TEMP *CON 25.0
      *MOD 4 1 1:7 = 60
          3 1 1:7 = 60
**          2 1 1 = 60
**          2 1 7 = 60
**          1 1 1 = 60
**          1 1 7 = 60

```

```

*SW *IJK 1 1 1:3 0.0
          1 1 4 0.168993763
          1 1 5:7 0.0
*SO *IJK 1 1 1:3 0.0
          1 1 4 0.043376222
          1 1 5:7 0.0

```

```

*SG *IJK 1 1 1:3 1
          1 1 4 0.787630015
          1 1 5:7 1

```

```

** Gas in tube is air (79.3% N2 & 20.7% O2)
*mfrac_gas 'N2 ' *con 0.793
*mfrac_gas 'O2 ' *con 0.207

```

```

**-----NUMERICAL CONTROL

```

```

*NUMERICAL
*DIMAX 5
*MAXSTEPS 19999

```

```

**-----RECURRENT DATA

```

```

*RUN
*TIME 0
*DTWELL 0.01

```

```

*WELL 'PRODUCER'

```

*WELL 'INJECTOR'

**-----HEATERS ON-----

*HEATR *IJK 4 1 1:7 6.8e4

**-----AIR INJECTION PERIOD-----

*INJECTOR 'INJECTOR'

*TINJW 25

*INCOMP *GAS 0 0 0 0.7930 0.2070 0 0 0

*OPERATE *STG 1500 **cm³/min

*GEOMETRY *K 0.15 1 1 0

*PERF *TUBE-END 'INJECTOR'

1 1 1 1

**===== GAS PRODUCTION =====

*PRODUCER 'PRODUCER'

*OPERATE *MIN *BHP 689.4757

*GEOMETRY *K 0.15 1 1 0

*PERF *TUBE-END 'PRODUCER'

1 1 7 1

*TIME 2

*TIME 4

*TIME 6

*TIME 8

*TIME 10

*TIME 12

*TIME 14

*TIME	16
*TIME	18
*TIME	20
*TIME	22
*TIME	24
*TIME	26
*TIME	28
*TIME	30
*TIME	32
*TIME	34
*TIME	36
*TIME	38
*TIME	40
*TIME	42
*TIME	44
*TIME	46
*TIME	48
*TIME	50
*TIME	52
*TIME	54
*TIME	56
*TIME	58
*TIME	60
*TIME	62
*TIME	64
*TIME	66
*TIME	68
*TIME	70
*TIME	72
*TIME	74
*TIME	76

*TIME 78
*TIME 80
*TIME 82
*TIME 84
*TIME 86
*TIME 88
*TIME 90
*TIME 92
*TIME 94
*TIME 96
*TIME 98
*TIME 100
*TIME 102
*TIME 104
*TIME 106
*TIME 108
*TIME 110
*TIME 112
*TIME 114
*TIME 116
*TIME 118
*TIME 120
*TIME 122
*TIME 124
*TIME 126
*TIME 128
*TIME 130
*TIME 132
*TIME 134
*TIME 136
*TIME 138

*TIME	140
*TIME	142
*TIME	144
*TIME	146
*TIME	148
*TIME	150
*TIME	152
*TIME	154
*TIME	156
*TIME	158
*TIME	160
*TIME	162
*TIME	164
*TIME	166
*TIME	168
*TIME	170
*TIME	172
*TIME	174
*TIME	176
*TIME	178
*TIME	180
*TIME	182
*TIME	184
*TIME	186
*TIME	188
*TIME	190
*TIME	192
*TIME	194
*TIME	196
*TIME	198
*TIME	200

*TIME 202
*TIME 204
*TIME 206
*TIME 208
*TIME 210
*TIME 212
*TIME 214
*TIME 216
*TIME 218
*TIME 220
*TIME 222
*TIME 224
*TIME 226
*TIME 228
*TIME 230
*TIME 232
*TIME 234
*TIME 236
*TIME 238
*TIME 240
*TIME 242
*TIME 244
*TIME 246
*TIME 248
*TIME 250
*TIME 252
*TIME 254
*TIME 256
*TIME 258
*TIME 260
*TIME 262

```
*TIME 264
*TIME 266
*TIME 268
*TIME 270
*TIME 272
*TIME 274
*TIME 276
*TIME 278
*TIME 280
*STOP
```

Bibliography

- [1] S. A. Abu-Khamsin, The Reaction Kinetics of Fuel Formation For In-situ Combustion, PhD Dissertation, The Department of Petroleum Engineering, Stanford University, 1984.
- [2] K. O. Adegbesan, J. K. Donnelly, R. G. Moore, and D. W. Bennion, Liquid phase oxidation kinetics of oil sands bitumen: Models for in situ combustion numerical simulators. *AIChE Journal*, 32(8), pp. 1242-1252, 1986.
- [3] J. Asmussen, H. H. Lin, B. Manring, R. Fritz, Single-mode or controlled multi-mode microwave cavity applicators for precision materials processing, *Review of Scientific Instruments*, 58, pp.1477-1486, 1987.
- [4] J. H. Bae, Characterization of crude oil for fireflooding using thermal analysis methods. *SPE Journal*, 17(3), pp. 211-218, 1977. (SPE 6173-PA)
- [5] M. Bazargan, A. Lapene, B. Chen, L. Castanier, and A. R. Kavscek, An Induction Reactor For Studying Crude-Oil Oxidation Relevant to In-Situ Combustion, pending.
- [6] J. D. M. Belgrave, R. G. Moore, M. G. Ursenbach and D. W. Bennion, A Comprehensive Approach to In-Situ Combustion Modeling, *SPE Advanced Technology Series*, pp. 98-107, 1993. (SPE 20250-PA)
- [7] I. Bousaid, Oxidation of Crude Oil in Porous Media, Ph.D Thesis, Texas A&M University, 1967.

- [8] I. Bousaid and H.J. Ramey Jr. Oxidation of crude oil in porous media. SPE Journal, 8(2), pp. 137-148, 1968. (SPE 1937-PA)
- [9] S. M. Bradshaw, E. J. Wyk, J. B.Swardt, Microwave Heating Principles and the Application to the Regeneration of Granular Activated Carbon, Journal of The South African Institute of Mining and Metallurgy, 98, pp. 201-210, , 1998.
- [10] W. E. Brigham, L. M. Castanier, In-Situ Combustion, Chapter 17, Petroleum Engineers Handbook, Society of Petroleum Engineers, 2004.
- [11] D. Briggs and J. T. Grant, Surface Analysis by Auger and X-Ray Photoelectron Spectroscopy. IM Publications, Chichester, U.K, 2003.
- [12] J. Cheng, R. Roy, D. Agrawal, Experimental proof of major role of magnetic field losses in microwave heating of metal and metallic composites, 20, pp. 1561-1563, 2004.
- [13] A. B. Chhetri and M. R. Islam, A Critical Review of Electromagnetic Heating for Enhanced Oil Recovery, Petroleum Science and Technology, 26, pp. 1619-1631, 2008.
- [14] M. Cinar, L. M. Castanier, A. R. Kavscek, Improved Analysis of the Kinetics of Crude-Oil In-Situ Combustion, SPE Western Regional and Pacific Section AAPG Joint Meeting, Bakersfield, California, USA, 29 March-2 April 2008. (SPE 113948-MS)
- [15] M. Cinar, L. M. Castanier, A. R. Kavscek, Isoconversional Kinetic Analysis of the Combustion of Heavy Hydrocarbons, SPE Western Regional Meeting, San Jose, California, 24-26 March 2009. (SPE 120995-MS)
- [16] M. Cinar, L. M. Castanier, A. R. Kavscek, Isoconversional Kinetic Analysis of the Combustion of Heavy Hydrocarbons, Energy and Fuels, 23, pp. 4003-4015, 2009.

- [17] M. Cinar, Kinetics of Crude Oil Combustion in Porous Media Interpreted Using Isoconversional Methods, PhD Dissertation, The Department of Energy Resources Engineering Stanford University, 2011.
- [18] M. Cinar, B. Hascakir, L. M. Castanier, A. R. Kavscek, Predictability of Crude Oil In-Situ Combustion by the Isoconversional Kinetic Approach, SPE Journal, Volume 16, Number 3, pp. 537-547, 2011. (SPE 148088-PA)
- [19] CMG-STARs. Advanced Process and Thermal Reservoir Simulator. Computer Modelling Group Ltd, Alberta, Canada, 2008.
- [20] R. B. Crookston, W. E. Culham, and W. H. Chen. A numerical simulation model for thermal recovery processes. SPE Journal, 19(1), pp. 37-58, 1975. (SPE 6724-PA)
- [21] M. K. Dabbous, P. Fulton, Low Temperature Oxidation Reaction Kinetics and Effects on the In-Situ Combustion Process, SPE Journal, 14(3), pp. 253-262, 1974. (SPE 4143-PA)
- [22] J. C. Dechaux, J. L. Flament, and M. Lucquinm, Negative temperature coefficient in the oxidation of butane and other hydrocarbons. Combustion and Flame, 17(2), pp. 205-214, 1971.
- [23] B. Dechelette, O. Heugas, G. Quenault, and Bothua, Air injection-improved determination of the reaction scheme with ramped temperature experiment and numerical simulation, Journal of Canadian Petroleum Technology, 45(1), pp. 41-47, January 2006.
- [24] Z. C. Djenni, B. Hamada, F. Chemat, Atmospheric Pressure Microwave Assisted Heterogeneous Catalytic Reactions, Molecules, 12, pp. 1399-1409, 2007.
- [25] O. Drici, S. Vossoughi, Study of the Surface Area Effect on Crude Oil Combustion by Thermal Analysis Techniques, Journal of Petroleum Technology, pp. 731-735, 1985.

- [26] R. Dubey, New Era In The Field Of Synthetic Chemistry: Microwave Assisted Synthesis, 2008, <http://www.pharmainfo.net/reviews/new-era-field-synthetic-chemistry-microwave-assisted-synthesis>.
- [27] M. B. Dusseault, Comparing Venezuelan and Canadian Heavy Oil and Tar sands, Canadian International Petroleum Conference, Calgary, Alberta, Canada, Jun. 12-14, 2011.
- [28] E. V. Eycken, P. Appukkuttan, W. D. Borggraeve, W. Dehaen, D. Dallinger, C. O. Kappe, High-speed microwave-promoted Hetero-Diels-Alder reactions of 2(1H)-pyrazinones in Ionic Liquid Doped Solvents, *The Journal of Organic Chemistry*, Vol. 67, pp. 7904 -7907, 2002.
- [29] M. L. Fall and W. J. Walker, Sintering Wear Parts with Microwave Heating, paper presented at the 104th Annual Meeting and Exposition of the American Ceramic Society St. Louis, MO, April 2002.
- [30] M. R. Fassihi, Analysis of Fuel Oxidation in In-situ Combustion Oil Recovery, PhD dissertation, Stanford University, Stanford, CA, 1981.
- [31] M. R. Fassihi, W. E. Brigham, Jr. Ramey, J. Henry, Reaction Kinetics of In-Situ Combustion: Part 1-Observations, *SPE Journal*, pp. 399-407, 1984. (SPE 8907-PA)
- [32] M. R. Fassihi, W. E. Brigham, Jr. Ramey, J. Henry, Reaction Kinetics of In-Situ Combustion: Part 2-Modeling, *SPE Journal*, pp. 408-416, 1984. (SPE 9454-PA)
- [33] A. Fini, A. Breccia, Chemistry by microwaves, *Pure and Applied Chemistry*, 71, 573-579. 1999.
- [34] N. P. Freitag and D. R. Exelby. A sara-based model for simulating the pyrolysis reactions that occur in high-temperature eor processes. *Journal of Canadian Petroleum Technology*, 45(3), pp. 38-44, 2006.
- [35] H. L. Friedman, Kinetics of thermal Degradation of Char-Forming Plastics from Thermogravimetry. Application to a Phenolic Plastic, *Journal of Polymer Science: Part C*, 6, 183-195, 1964.

- [36] C. Gabriel, S. Gabriel, E. H. Grant, B. S. J. Halsteadb, D. M. P. Mingosb, Dielectric Parameters Relevant to Microwave Dielectric Heating, *Chemical Society Reviews*, 27, 213, 1998.
- [37] Z. Gao, I. Amasaki, T. Kaneko, M. Nakada, Assessment of the error of the pre-exponential factor obtained from the isoconversional plot and the single heating rate plot for dynamic thermogravimetric measurement of polymer degradation, *Polymer Degradation and Stability*, 83, pp. 67-70, 2004.
- [38] S. D. Gardner, C. S. K. Singamsetty, G. L. Booth, G. He, and C. U. Pittman, Surface characterization of carbon
bers using angle-resolved xps and iss. *Carbon*, 33(5), pp. 587-595, 1995.
- [39] R. Gedye, F. Smith, K. Westaway, H. Ali, L. Baldisera, L. Laberge, J. Rousell, The use of microwave ovens for rapid organic synthesis *Tetrahedron letters*, 27, 279-282, 1986.
- [40] M. Gerritsen, A. Kavscek, L. Castanier, J. Nilsson, R. Younis, B. He, Experimental Investigation and High Resolution Simulator of in-situ Combustion Processes; 1. Simulator Design and Improved Combustion with Metallic Additives, SPE International Thermal Operations and Heavy Oil Symposium and Western Regional Meeting, Bakersfield, California, 16-18 March 2004. (SPE 86962-MS)
- [41] M. Gerritsen and A. Kavscek, Experimental Investigation and High Resolution Simulation of In-Situ Combustion Processes, DOE Award No.: DE-FC26-03NT15405, 2008.
- [42] R. J. Giguere, T. L. Bray, S. M. Ducan, G. Majetich, Application of commercial microwave ovens to organic synthesis, *Tetrahedron letters*, vol. 27, no41, pp. 4945-4948, 1986.
- [43] P. Glarborg, R. J. Kee, J. F. Grcar, J. A. Miller, PSR: A Fortran Program for Modeling Well-Stirred Reactors, Sandia Report, SAND86-8209, 1986.

- [44] P. Groombridge, A. Oloyede, E. Siores, A Control System for Microwave Processing of Materials, *Journal of Manufacturing Science and Engineering*, FEBRUARY 2000, Vol. 122, 2002
- [45] B. Hascakir, T. Babadagli, S. Akin, Experimental and Numerical Simulation of Oil Recovery from Oil Shales by Electrical Heating, *Energy and Fuels*, 22, 3976-3985, 2008.
- [46] B. Hascakir, G. Glatz, L. M. Castanier and A. R. Kavscek, In-Situ Combustion Dynamics Visualized With X-Ray Computed Tomography, *SPE Journal*, pp. 524-536, 2011. (SPE 135186-PA)
- [47] B. Hascakir, C. M. Ross, L. M. Castanier, A. R. Kavscek, Fuel Formation During In-Situ Combustion of Heavy Oil, *SPE Annual Technical Conference and Exhibition*, 30 October-2 November 2011, Denver, Colorado, USA. (SPE 148754-MS)
- [48] M. Hayashitani, D. W. Bennion, J. K. Donnelly, and R.G. Moore. Thermal cracking models for athabasca oil sands. In *SPE Annual Fall Technical Conference and Exhibition Proceedings*, Houston, Texas, 1-3 October 1978. SPE. SPE Annual Fall Technical Conference and Exhibition. (SPE 7549-MS)
- [49] B. He, Q. Chen, L. M. Castanier, A. R. Kavscek, Improved In-Situ Combustion Performance With Metallic Salt Additives, *SPE Western Regional Meeting*, Mar 30 - Apr 01, 2005 2005, Irvine, California. (SPE 93901-MS)
- [50] J. Y. Hwang, S. Shi, Z. Xu, K. W. Peterson, Synthesis of Monodispersed Iron Oxide Particles by a Large-Scale Microwave Reactor, *Chemical Engineering Communications*, 193, 1586-1591, 2006.
- [51] K. J. Hughes, T. Turanyi, A. R. Clague, M. J. Pilling, Development and testing of a comprehensive chemical mechanism for the oxidation of methane, *International Journal of Chemical Kinetics*, 33(9), pp. 513-538, 2001.
- [52] R. J. J. Jachuck, D. K. Selvaraj, R. S. Varma, Process Intensification: Oxidation of Benzyl Alcohol Using a Continuous Isothermal Reactor Under Microwave Irradiation, *Green Chemistry*, 8, 29-33, 2006.

- [53] C. Jackson, Upgrading a heavy oil using variable frequency microwave energy, paper SPE 78082 presented at the International Thermal Operations and Heavy Oil Symposium and International Horizontal Well Technology Conference, Alberta, Canada, November 4-7, 2002. (SPE 78982-MS)
- [54] J. Jacob, L. H. L. Chia, F. Y. C. Boey, Review Thermal and non-thermal interaction of microwave radiation with materials, *Journal of Materials Science*, 30, 5321-5327, 1995.
- [55] L. A. Jermolovicius, B. Schneiderman, J. T. Senise, Alteration of Esterification Kinetics Under Microwave Irradiation, presented at the 7th International Conference on Microwave and High Frequency Heating, Valencia, Spain, 1999.
- [56] C. O. Kappe, D. Dallinger, The Impact of Microwave Synthesis on Drug Discovery, *Nature Reviews Drug Discovery*, 5, 51-63, 2006.
- [57] C. O. Kappe, Microwave dielectric heating in synthetic organic chemistry, *Chemical Society Reviews*, 37, 1127-1139, 2008.
- [58] R. S. Kasevich, S. L. Price, D. L. Faust, and M. F. Fontaine, Pilot Testing of a Radio Frequency Heating System for Enhanced Oil Recovery from Diatomaceous Earth, SPE 28619 presented at the 69th Annual Technical Conference and Exhibition held in New Orleans, LA, USA, 25-28, 1994. (SPE 28619-MS)
- [59] S. A. Abu-Khamsin, The Reaction Kinetics of Fuel Formation For In-situ Combustion, PHD Dissertation, The Department of Petroleum Engineering, Stanford University, 1984.
- [60] R. Kharrat, S. Vossoughi, Feasibility Study of the In-Situ Combustion Process Using TGA/DSC Techniques, *Journal of Petroleum Technology*, Volume 37, Number 8, pp. 1441-1445, 1985.
- [61] J. M. Kremsner, C. O. Kappe, Silicon Carbide Passive Heating Elements in Microwave-Assisted Organic Synthesis, *The Journal of Organic Chemistry*, 71 (12), pp 4651-4658, 2006.

- [62] N. E. Leadbeater, Fast, Easy, Clean Chemistry by Using Water as A Solvent and Microwave Heating: the Suzuki Coupling as An Illustration, *Chemical Communications*, 23, 2881-2902, 2005.
- [63] G. P. Lewis, S. R. Wylie, A. Shaw, A. I. Al-Shamma, D. Phipps, R. Alkhaddar, G. Bond, Monitoring and control system for tuneable high frequency microwave assisted chemistry, *Journal of Physics: Conference Series* 76 012058, 2007.
- [64] M. E. Lucchesi, F. Chemat, J. Smadja, Solvent-free microwave extraction of essential oil from aromatic herbs: comparison with conventional hydro-distillation, *Journal of Chromatography A*, 1043 pp. 323-327, 2004.
- [65] D. D. Mamora, Kinetics of In-Situ Combustion, PhD dissertation, The Department of Petroleum Engineering, Stanford University, 1993.
- [66] F. Marken, Chemical and electro-chemical applications of in situ microwave heating, *Annual reports on the progress of chemistry. Section C, Physical chemistry*, 104, pp. 124-141, 2008.
- [67] C. Marques, L. M. Castanier, A. R. Kovscek, Thaw Front Dynamics and Super Insulated Wells for Thermal Recovery in Cold Environments, paper SPE 121059 presented at the 2009 SPE Western Regional Meeting held in San Jose, 2009. California, USA, March 24-26. (SPE 121059-MS)
- [68] J. A. Menendez, E. M. Menendez, M. J. Iglesias, A. Garcia, J. J. Pis, Modification of the surface chemistry of active carbons by means of microwave-induced treatments, *Carbon*, 37 pp. 1115-1121, 1999.
- [69] A. C. Metaxas, R. J. Meredith, 1983. *Industrial Microwave Heating*, Peter Peregrinus Ltd., London, 1983.
- [70] R. G. Moore, J. D. M. Belgrave, R. Mehta, M. Ursenbach, C.J. Laureshen, and K. Xi, Some insights into the low-temperature and high-temperature in-situ combustion kinetics, In *SPE/DOE Enhanced Oil Recovery Symposium Proceedings*,

- Tulsa, Oklahoma, 22-24 April 1992. SPE/DOE. SPE/DOE Enhanced Oil Recovery Symposium.
- [71] R. G. Moore, J. D. M. Belgrave, M. G. Ursenbach, and S. A. Mehta. In-situ combustion in heavy oil reservoirs: problems and perspectives. *In Situ*, 21, pp. 1-26, 1997.
- [72] R. G. Moore, S. A. Mehta, D. Gutierrez, Potential for In Situ Combustion in Depleted Conventional Oil Reservoirs, the Eighteenth SPE Improved Oil Recovery Symposium, Tulsa, Oklahoma, 2012. (SPE 154299-MS)
- [73] S. E. Moschopedis and J. G. Speight. Oxidation of a bitumen. *Fuel*, 54(3), pp. 210-212, 1975.
- [74] M. Nuchter, B. Ondruschka, W. Bonrathb, A. Gum, Microwave Assisted Synthesis - A Critical Technology Overview, *Green Chemistry*, 6, pp. 128-141, 2004.
- [75] O. Ogunbanwo, M. Gerritsen, A. Kavscek, Uncertainty Analysis on In-Situ Combustion Simulations Using Experimental Design, SPE Western Regional Meeting, 21-23 March 2012, Bakersfield, California, USA. (SPE 153887-MS)
- [76] V. Orsat, G. S. V. Raghavan, Initial Studies on Super-High-Frequency Microwave Heating of Foods, *Drying' 2002-Proceedings of the 13th International Drying Symposium*, Beijing, China, August 27-30, 2002
- [77] C. Ovalles, A. Fonseca, A. Lara, V. Alvarado, K. Urrecheaga, A. Ranson, H. Mendoza, Opportunities of Downhole Dielectric Heating in Venezuela: Three Case Studies Involving Medium, Heavy and Extra-Heavy Crude Oil Reservoirs, paper SPE 78980 presented at the 2002 SPE International Thermal Operations and Heavy Oil Symposium and International Horizontal Well Technology Conference held in Calgary, Alberta, Canada, November 4-7, 2002. (SPE 78980-MS)
- [78] E. G. Pana, A. A. Ravaevb, Microwave synthesis of advanced dental ceramic-alloy materials, *Materials Letters* 58 pp. 2679- 2683, 2004.

- [79] C. R. Patrick, Reactions in the Gas and Liquid Phases: Comparison of Kinetic and Thermodynamic Data, *International Journal of Chemical Kinetics*, VOL. 5, pp. 769-776, 1973.
- [80] W. L. Perry, J. D. Katz, D. Rees, M. T. Paffet, A. K. Datyey, Kinetics of the Microwave-Heated CO Oxidation Reaction over Alumina-Supported Pd and Pt Catalysts, *Journal of Catalysis* 171, 431-438, 1997.
- [81] W. L. Perry, A. K. Datye, A. K. Prinja, L. F. Brown, J. D. Katz, Microwave Heating of Endothermic Catalytic Reactions: Reforming of Methanol, *AIChE Journal*, 48, 820-831, 2002.
- [82] U. R. Pillai, E. S. Demessie, R. S. Varma, Hydrodechlorination of Chlorinated Benzenes in a Continuous Microwave Reactor, *Green Chemistry*, 6, 295-298, 2004.
- [83] D. M. Pozar, *Microwave Engineering*, 3rd Edition, 2004.
- [84] M. Prats, *Thermal Recovery*, Vol. 7 of SPE Monograph Series, Society of Petroleum Engineers, 1986.
- [85] R. Roy, R. Peelamedu, L. Hurtt, J. Cheng, D. Agrawa, Definitive experimental evidence for Microwave Effects: radically new effects of separated E and H fields, such as decrystallization of oxides in seconds, *Materials Research Innovations*, 6, pp.128-140, 2002.
- [86] K. I. Rybakov, V. E. Semenov, S. V. Egorov, A. G. Ereemeev, I. V. Plotnikov, Y. V. Bykov, Microwave Heating of Conductive Powder Materials, *Journal of Applied Physics*, 99, 023506, 2006.
- [87] E. B. Ripley, Thermocouple shield, Patent, US 2008/0232428 A1, 2008.
- [88] V. I. Rudnev, D. Loveless, R. Cook, M. Black, *Handbook of Induction Heating: Manufacturing Engineering and Materials Processing*, New York : Marcel Dekker, 2003.

- [89] A. Sahni, M. Kumar, R. B. Knapp, Electromagnetic Heating Methods for Heavy Oil Reservoirs, 2000 Society of Petroleum Engineers SPE/AAPG, 2000.
- [90] K.A. Safinya, A. Kovcek, B. Chen, Apparatus and Method for Characterizing Parameters for the Cracking, In-Situ Combustion, and Upgrading of Hydrocarbons, Patent, 2010. doe/pc/91008-0375, United States Department of Energy, National Petroleum Technology Office, January 1999.
- [91] P. Sarathi, In-situ combustion handbook principles and practices. Final report: November 1998,
- [92] P. Sarathi, Environmental Aspects of Heavy-Oil Recovery by Thermal EOR Processes, Journal of Petroleum Technology, 43(6), pp. 662-666, 718-721, 1991.
- [93] P. Sarathi, In-Situ Combustion Handbook - Principles and Practices, Report: DOE/PC/91008-0374, OSTI-ID: 3174, National Petroleum Technology Office, U.S. D.O.E., Tulsa, OK, 1999.
- [94] M. Shimada, Y. Azuma, K. Okuyama, Y. Hayashi, E. Tanabe, Plasma Synthesis of Light Emitting Gallium Nitride Nanoparticles Using a Novel Microwave-Resonant Cavity, Japanese Journal of Applied Physics, 45, pp. 328-332, 2006.
- [95] I. Silverwood, G. McDougall, G. Whittaker, Comparison of Conventional Versus Microwave Heating of The Platinum Catalysed Oxidation of Carbon Monoxide Over EUROPT-1 in A Novel Infrared Microreactor Cell, Journal of Molecular Catalysis A: Chemical, 269, pp.1-4, 2007.
- [96] M. D. Smooke, V. Giovangigli, Reduced Kinetic Mechanisms and Asymptotic Approximations for Methane-Air Flames, Lecture Notes in Physics, 384, 2, pp. 29-47, 1991.
- [97] K. Srogi, A Review: Application of Microwave Techniques for Environmental Analytical Chemistry, Analytical Letters, 39, pp.1261-1288, 2006.

- [98] D. Stuerge, P. Gaillard, Microwave heating as a new way to induce localized enhancements of reaction rate Non-Isothermal and heterogeneous kinetics, *Tetrahedron*, 52, pp. 5505-5510, 1996.
- [99] G. A. Tompsett, W. C. Conner, K. S. Yngvesson, Microwave Synthesis of Nanoporous Materials, *ChemPhysChem*, 7, pp.296-319, 2006
- [100] M. Y. Tse, M. C. Depew, K. S. Jeffrey, Applications of High Power Microwave Catalysis in Chemistry, *Research on Chemical Intermediates*, 13, pp. 221-236, 1990.
- [101] T. N. Tulasidas, G. S. V. Raghavan, A. S. Mujumdar, Microwave Drying of Grapes in a Single Mode Cavity at 2450 Mhz - i: Drying Kinetics, *Drying Technology*, 13, pp. 1949-1971, 1995.
- [102] A. T. Turta, S. K. Chattopadhyay, R. N. Bhattacharya, A. Condrachi, W. Hanson, Current Status of Commercial In Situ Combustion Projects Worldwide, *Journal of Canadian Petroleum Technology*, Volume 26, No. 11, 2007, pp. 8-14
- [103] A. T. Turta, R. Coates, M. Greaves, In-Situ Combustion in the Oil Reservoirs Underlain by Bottom Water. Review of the Field and Laboratory Tests, *Canadian International Petroleum Conference*, Calgary, Alberta, Jun 16-18, 2009.
- [104] S. F. Uy, A. J. Easteal, M. M. Farid, R. B. Keam, G. T. Conner, Seaweed Processing Using Industrial Single-mode Cavity Microwave Heating: a Preliminary Investigation, *Carbohydrate Research*, 340, 1357-1364, 2005.
- [105] B. Verkoczy, K. N. Jha, Saskoil, Screening Of Heavy Oil Reservoirs For Enhanced Oil Recovery By Thermal Methods, *Annual Technical Meeting*, Jun 2 - 5, 1985 , Edmonton, Alberta, Canada.
- [106] B. Verkoczy, Factors Affecting Coking in Heavy Oil Cores, Oils and SARA Fractions Under Thermal Stress, *Journal of Canadian Petroleum Technology*, pp. 25-33, 1993.

- [107] B. Verkoczy, N. P. Freitag, Oxidation Of Heavy Oils And Their Sara Fractions - Its Role In Modelling In-Situ Combustion, Technical Meeting / Petroleum Conference Of The South Saskatchewan Section, Oct 19 - 22, 1997, Regina.
- [108] F. Vermeulen, B. C. W. McGee, In Situ Electromagnetic Heating for Hydrocarbon Recovery and Environmental Remediation, Journal of Canadian Petroleum Technology, 39, pp. 24-28, 2000.
- [109] S. Vossoughi, G. W. Bartlett, G. P. Willhite, Development of a Kinetic Model for In-Situ Combustion and Prediction of the Process Variables using TGA/DSC Techniques, SPE Annual Technical Conference and Exhibition, 26-29 September 1982, New Orleans, Louisiana.
- [110] S. Vossoughi, G. P. Willhite, W. P. Kritikos, I. M. Guvenir, Y. EL Shoubary, Automation of an In-Situ Combustion Tube and Study of the Effect of Clay on In-situ Combustion Process, SPE Journal, 22(4), pp. 493-502, 1982
- [111] S. Vossoughi, G. W. Bartlett, G. P. Willhite, Prediction of In-Situ Combustion Process Variables By Use of TGA/DSC Techniques and the Effect of Sand-Grain Specific Surface Area on the Process, SPE Journal, Volume 25, Number 5, pp. 656-664, 1985.
- [112] S. Vyazovkin, Evaluation of Activation Energy of Thermally Stimulated Solid-State Reactions under Arbitrary Variation of Temperature, Journal of Computational Chemistry, 18, 393-402, 1997.
- [113] S. Vyazovkin and C. A. Wight, Isothermal and Nonisothermal Reaction Kinetics in Solids: In Search of Ways toward Consensus, J. Phys. Chem. A, 101, pp. 8279-8284, 1997.
- [114] S. Vyazovkin, N. Sbirrazzuoli, Isoconversional method to explore the mechanism and kinetics of multi-step epoxy cures, Macromol. Rapid Commun. 20(8), pp. 387-389, 1999.

- [115] S. Vyazovkin, Modification of the Integral Isoconversional Method to Account for Variation in the Activation Energy, *Journal of Computational Chemistry*, 22, 178-183, 2001.
- [116] Z. S. Wei, Z. Y. Du, Z. H. Lin, H. M. He, R. L. Qiu, Removal of NO_x by microwave reactor with ammonium bicarbonate and Ga-A zeolites at low temperature, *Energy*, 32, pp. 1455-1459, 2007.
- [117] I. A. Wiehe, A phase-separation kinetic model for coke formation, *Industrial and Engineering Chemistry Research*, 32(11), pp. 2447-2454, 1993.
- [118] H. Will, P. Scholz, B. Ondruschka, Microwave-Assisted Heterogeneous Gas-Phase Catalysis, *Chemical engineering and technology*, 27, pp.113-122, 2004.
- [119] D.V. Yannimaras and D.L. Tiffin, Screening of oils for in-situ combustion at reservoir conditions by accelerating-rate calorimetry, *SPE Reservoir Engineering*, 10(1), pp. 36-39, February 1995.
- [120] N. Yoshikawa, E. Ishizuka, K. Mashiko, S. Taniguchi, Difference in Carbo-thermal Reduction Reaction Kinetics of NiO in Microwave E- and H-fields, *Materials Letters*, 61, pp.2096-2099, 2006.
- [121] X. L. Zhang, D. O. Hayward, M. P. Mingos, Apparent equilibrium shifts and hot-spot formation for catalytic reactions induced by microwave dielectric heating, *Chem. Commun.*, pp.975-976, 1999.
- [122] X. L. Zhang, D. O. Hayward, M. P. Mingos, Microwave Dielectric Heating Behavior of Supported MoS₂ and Pt Catalysts, *Industrial and Engineering Chemistry Research*, 40, pp. 2810-2817, 2001.
- [123] X. L. Zhang, D. O. Hayward, Applications of microwave dielectric heating in environment-related heterogeneous gas-phase catalytic systems, *Inorganica chimica acta incorporating f-Block elements*, 359, pp.3421-3433, 2006.

- [124] Z. Zhu, M. Bazargan, A. Lapene, M. Gerritsen, L. Castanier and A. Kavscek, Upscaling for Field-scale In-situ Combustion Simulation, SPE Western North American Region Meeting, Anchorage, Alaska, USA, 7-11 May 2011.
- [125] http://www.netl.doe.gov/technologies/oil-gas/publications/eordrawings/BW/bwinsitu_comb.PDF.
- [126] USGS World energy assessment team. Usgs world petroleum assessment 2000 - description and results, <http://pubs.usgs.gov/dds/dds-060/index.html>, (accessed April 2011).